Evolution and Use of CFD for Separated Flow Simulations Relevant to Military Aircraft

Arthur Rizzi
Royal Institute of Technology (KTH)
Stockholm, 100 44
SWE

rizzi@kth.se

James M. Luckring
NASA Langley Research Center
Hampton, VA, 23681
USA

james.m.luckring@nasa.gov

ABSTRACT

Separated flows often set aerodynamic limits for an aircraft flight envelope, and many of these flows remain difficult to predict with Computational Fluid Dynamics. This paper reviews and explores how CFD simulations have been used for predicting separated flows, and the associated aerodynamic performance, throughout the flight envelope, giving special focus to NATO aircraft. The review entails: a summary of the physics of flow separation that is especially difficult to model numerically; a top-level survey of seven decades of CFD developments to meet many of the challenges of separated flow predictions; six case studies for an assessment of the current CFD capabilities; and future prospects. Significant advances are still needed for separated flow simulations to become practical with reliabilities comparable to attached flow simulations. Some recommendations for future work are included.

NOMENCLATURE

$b/2$	wing semispan	Q	vorticity visualization parameter
C_D	drag coefficient, drag / (q_∞ S_{ref})	q_∞	free-stream reference dynamic pressure
C_f	skin friction coefficient	Re_{cref}	Reynolds number, U_∞ c_{ref} / ν
C_L	lift coefficient, lift / (q_∞ S_{ref})	S_{ref}	wing reference area
C_l	Rolling moment coefficient, rolling moment / (q_∞ S_{ref} b)	s	local semispan
C_N	normal force coefficient, normal force / (q_∞ S_{ref})	t/c	airfoil thickness-to-chord ratio
C_p	static pressure coefficient	U_∞	freestream reference velocity
c	wing chord	x,y,z	body axis Cartesian coordinates
c_r	root chord	x_b	longitudinal vortex breakdown location
$cref$	reference chord	α	angle of attack, deg.
g	weight force parameter	β	angle of sideslip, deg.
L	body length	γ	boundary layer intermittency. Also, shear stress angle, deg.
M	Mach number	η	fraction of semispan
mac	wing mean aerodynamic chord	θ	boundary layer momentum thickness. Also, circumferential angle, deg.
Pa	Pascals	Λ	wing sweep, deg.
p,q,r	Roll, pitch, and yaw rotary rates, deg/sec	ν	kinematic viscosity

Subscripts

le	leading edge	*rms*	root mean square
max	maximum	*vb*	vortex breakdown
ref	reference	∞	free-stream reference conditions

Abbreviations

AGARD	Advisory Group for Aerospace Research and Development	NLG	Nose Landing Gear
AMR	Adaptive Mesh Refinement	RANS	Reynolds Averaged Navier Stokes
AVT	Applied Vehicle Technology	RTO	Research and Technology Organization
DES	Detached Eddy Simulation	SA	Spalart-Allmaras turbulence model
FC	Flight Condition	SADES	Hybrid SA / DES model
LBM	Lattice Boltzman Method	SARC	SA with Rotation Correction
LEX	Leading-edge EXtension	SST	Shear Stress Transport turbulence model
MLG	Main Landing Gear	STO	Science and Technology Organization
MLG	Main Landing Gear	UCAV	Uninhabited Combat Air Vehicle
NATO	North Atlantic Treaty Organization	URANS	Unsteady RANS

1.0 INTRODUCTION

Every object submersed in a stream of air undergoes separation. As a packet of air approaches a wing, it attaches along a line near the leading edge, traverses over it and ultimately separates from it to continue the journey downstream. The specific details of its dynamical motion over the wing surface, including the separation location, determines the aerodynamic performance of the wing (lift and drag). The Navier-Stokes equations describe this dynamical motion, hence performance can be studied by numerical approximations to these equations, along with measurements in wind tunnels and flight tests.

Among the aerodynamic characteristics that are central to aircraft performance is the lift-curve slope, the attainable maximum lift, $C_{L,max}$, the angle of attack that this maximum occurs, α_{max}, and interpreted as stall indicating the limit to the flight envelope. As angle of attack increases, but before α_{max} is reached, buffet usually is encountered, stable leading edge vortices may break down indicating the onset of chaotic separated flow over the aircraft. Beyond stall, this chaotic separated flow grows in size and strength, suggesting three overall sectors of the flight envelope: 1) cruise, where the flow is attached and benign, 2) maneuver, which includes the onset of buffet and vortex bursting and 3) post-stall maneuver and heavy buffet.

The last AGARD Conference on Separation[1] was held in 1975, nearly 45 years ago, and CFD was just dawning then. The intervening years have brought much development and application of computational methods, and we present our overview of them with special interest on the status of CFD for simulating flight conditions of NATO aircraft in these three regions of flight.

From unaccelerated flight at 1*g*, the pilot flies the aircraft and commands performance to accelerating flight at multiple *g*s by increasing lift in three ways: increase incidence angle, α, increase speed, *M*, and reconfigure the geometry, e.g., deploy the slats and/or flaps. Depending on the aircraft being flown, the pilot's particular "mix" of these three leads to the specific flow conditions at that instance in time. And such flow conditions may be easy or hard to simulate accurately with CFD.

1.1 Military Aircraft Challenges

To make this discussion more concrete, see Figure 11-1 that displays representative NATO aircraft in a chart with vertical axis of increasing speed (*M*) and horizontal axis of the sweep angle of the aircraft typical of its speed class. Subsonic unswept-wing aircraft as a class, at the bottom left, encounter with increasing alpha

what we can call "classical boundary layer separation" that leads to stall. Airlifters, in the middle of the chart, fly transonically where shock waves over the wing interact with, and separate, the boundary layer at lower alpha than for subsonic flight without shocks – termed shock-induced separation. Slender (or low aspect ratio) fighter aircraft at the right, capable of supersonic flight, exploit stable vortex flow separating from the leading edge of their thin highly swept wings at moderate angles of attack. These vortices can interact with shocks, breakdown and lead to buffet and ultimately stall with "massively separated" flow. Hybrid wings may have Shock/Boundary-Layer Interaction (SBLI) and leading-edge vortex separation. Hirschel et al.[2] explain and elaborate these types of phenomena, their modeling and computation, at book-length.

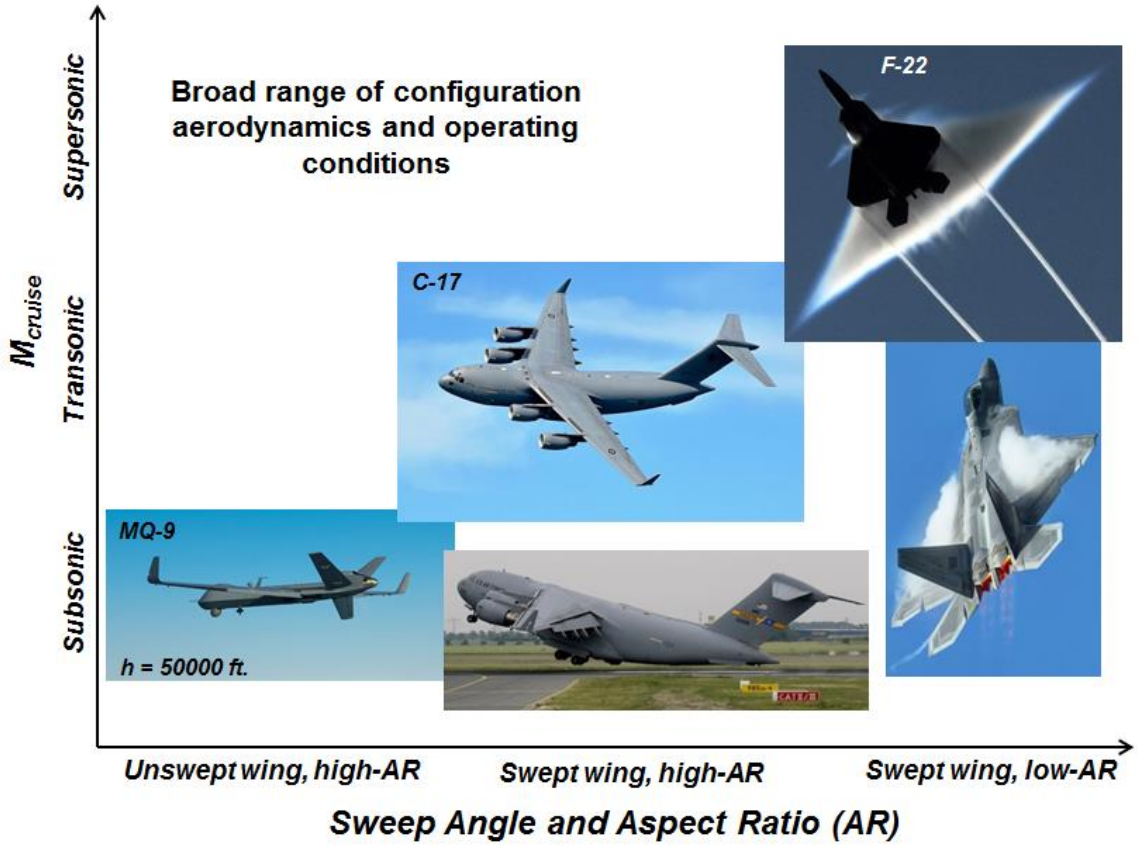

Figure 11-1: Military aircraft and operations.

Missiles and launch vehicles (not shown) have their own separated flow challenges. At liftoff/boost conditions, the vehicle can be at 90° angle of attack due to cross winds and must transition at low speeds through several forebody separation domains to essentially zero degrees angle of attack while accelerating. At high speeds, launch vehicles can have multibody booster separation with separated flows while missiles can encounter complex vortex-shock interactions with flow separation at terminal maneuver.

These are the types of challenges that must be met for the accurate CFD prediction of aircraft performance, and this paper is laid out to track the evolution of the CFD methodology that enables this broad range of separation problems to be studied, and illustrates, with concrete examples, some particular solutions to indicate how the methodology is being used.

1.2 Organization of Paper

In attempting to approach this goal, the paper begins with the next section describing the physics involved in the separation problems under consideration to give credence to the claim that some of these are indeed

difficult problems to solve today. Others are more tractable and our third section traces three decades of CFD development that makes this class of problem tractable today. The fourth section, the heart of the paper, digs deeper into those flight conditions that are still problematical today. Our approach in elucidating these is to overview six different categories of flight conditions that have been, and are still, under study in a number of collaborative CFD assessment campaigns because it is our belief that computational work has benefited significantly by establishing a collective group for the numerical investigations. Our overview of those six categories of flight conditions focuses on various categories of flow separation: i) steady, controlled and ordered vortex separation from smooth surfaces of slender wings; ii) the unsteady breakdown of such vortices caused by higher incidence in subsonic flow, or by shock wave interaction at transonic speeds; iii) unsteady separation from a hybrid wing, such as the F-18, caused by shock-boundary-layer interaction (SBLI) leading to abrupt wing stall; iv) maneuvering flight where the accelerating motion of the aircraft causes unsteady smooth-surface separation of vortices and their accompanying time-dependent motion in the flowfield; v) maximum lift and stall separation on a multielement wing; and finally, (vi) unsteady component loads from an open landing gear cavity.

Although single-code/single-investigator CFD assessments will continue to advance our craft, a teamed and sustained collaborative campaign offers significant benefits for understanding complex aerodynamic phenomena because of the diversity of opinion and numerical formulation along with the opportunity to assess numerical uncertainty. Examples are the AIAA Predictive Workshops and the AVT Task Groups and the NASA CAWAPI series. Each of these campaigns has a unique aerodynamic focus that, in turn, stresses different underlying flow physics.

For CFD to provide predictive capability, simulation of such relevant underlying flow physics with sufficient fidelity is required. However, a priori knowledge of just what the relevant physics are, and just what sufficient fidelity really constitutes can be elusive. As a case in point, many of the collaborative assessments are spawning new wind-tunnel tests to better understand the particular focus topics and to possibly provide validation-class data for code assessment and improvement – we term these physics-based investigations, which, in some cases, can approach the so-called “Unit Problems”. This class of collaborative CFD assessment with focused validation-like experimentation that is directed toward the particular program objectives for enhanced CFD predictive capability appears to be a very fruitful approach for future advancements to computational aerodynamics.

Not all of the challenges are in hand today. The fifth section presents our look ahead and discusses some of the prospects for the future. Lastly, the paper concludes with an overall summary of our findings and a path forward.

2.0 SEPARATION – A HARD PROBLEM

The advent of jet propulsion in the late 1940s brought high-speed flight, shock waves on swept and low aspect ratio configurations where separation, as a phenomenon, branched out in several directions from classical boundary-layer separation on an unswept wing to controlled vortex separation, shock-induced separation, etc. Since the 1950s, these various branches of flow separation in three dimensions have been studied, and researchers have come forth with concepts like closed bubble separation and those involving free vortex layers or vortex sheets. Theoreticians found that the surface-flow topology of skin friction, i.e., wall streamlines, with different types of singular points and rules governing how they can occur, could shed light on how shear layers are shed from smooth surfaces. (See, for example, Chapter 7 of Hirshel et al.[3] for one thorough treatment.) The approach in CFD turns out to be more practical. Here, boundary-layer separation, as observed in the computed results, can be studied and interpretations, coupled to the physics involved, can be argued that are adequately resolved. With this in mind, let us look now at some of the physics involved in those military aircraft challenges.

2.1 Some Physics of Military Aircraft Challenges

Broad range of vehicle classes and operating conditions result in a wide variety of separated flows that are important to military aircraft operations. Figure 11-2 spells out some of the separated flow challenges for military aircraft in the operating conditions of Figure 11-1.

Straight-wing aircraft (e.g., WW2 type, HALE, surveillance, etc.) at the bottom left of figure, fly at strictly subsonic speeds where "classical boundary layer separation", i.e., partial pressure recovery facing an adverse pressure gradient forces the flow to detach from the wing surface before reaching the trailing edge. This is the classical wing-design problem and the optimum solution is to maintain attached flow all the way to the trailing edge (see, Hirshel et al.[2] for further discussion).

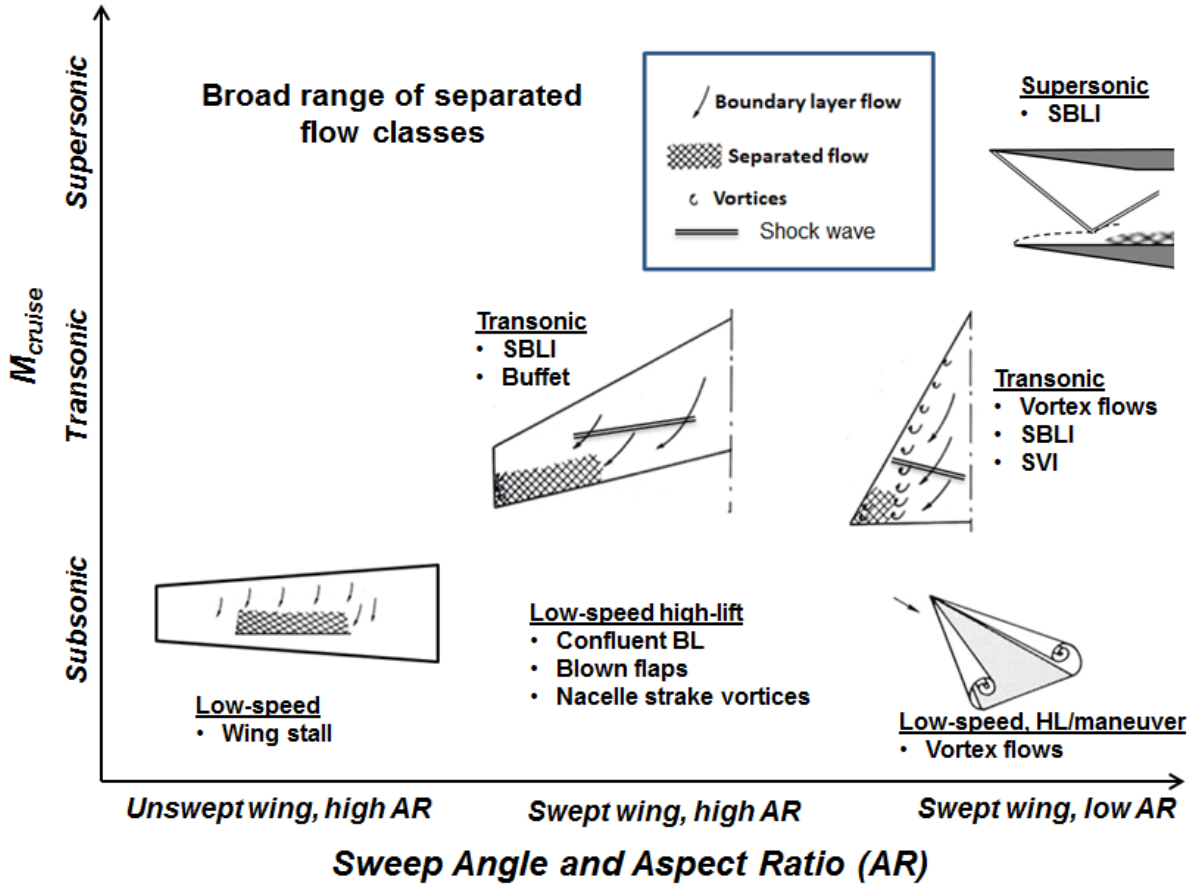

Figure 11-2: Military aircraft separated flows.

Jet propelled fighters as early as the late 1940s (e.g., F-86), as well as airlifters today, middle of figure, fly transonically with thick swept wings. In this condition, a new phenomenon "shock stall", brought on by shock waves interacting with the boundary layer, hinders pressure recovery even more so that separation occurs at an even lower incidence angle than at subsonic operating conditions. Also, swept wings are prone to tip stall, hence loss of aileron efficiency – a big problem for 1940s aircraft like the B-47 (as well as the F-86), which was solved by various "fixes" like vortex generators added to the outer wing panel.

Appearing early in the 1950s, column on right in figure, supersonic fighters required thin wings in slender configurations – high sweep meant lower high-speed drag but also generated less lift. However, it was discovered that separation from a sufficiently swept leading edge created a stable vortex over the wing that enhances the lift, and this effect is widely exploited in all designs. Flows with "coherent vortex separation"

then lead to new interaction phenomena: vortex breakdown stall, shock-vortex interaction, SBLI and shock-vortex-boundary layer interactions (SVBLI) of many variants.

The maneuver, or *V-n*, diagram in Figure 11-3 indicates the intended operating range within the flight envelope of military aircraft (see Figures11-1 and 11-2), and suggests the flow physics that may pertain to its aerodynamic performance as a function of speed and lift generated in terms of multiple *g* weight forces. Consider a vertical line at a given speed: at B, cruise, there is lift of 1*g* for level unaccelerated flight. For rapid pull-up, the pilot commands higher incidence, more lift of say 3*g* at C for combat and maneuver, and in so doing may encounter the onset of buffet. In another scenario, a horizontal line in the diagram, he may command higher speed at a given lift, say 2*g*, at D for supersonic operations, and may well encounter strong shock effects like shock stall. High lift devices are needed for takeoff and landing operations, location A, where confluent flows, possibly with transition effects, come into play.

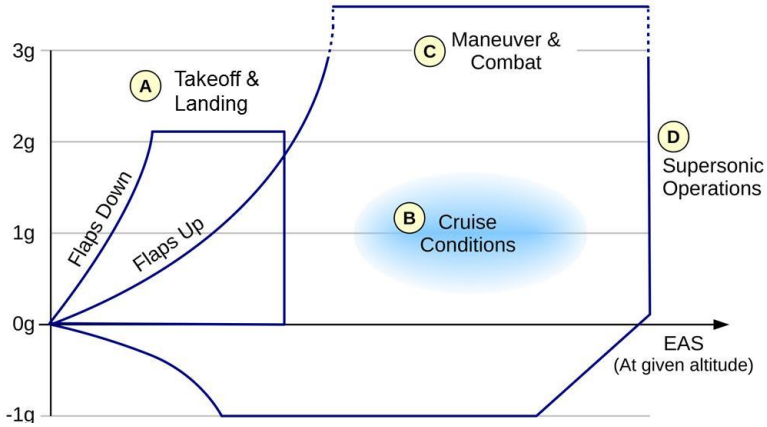

Figure 11-3: Separated flow consequences in maneuver diagram.

The lift-curve for the F-4 aircraft from Hall,[4] Figure 11-4, presents a typical example of what phenomena can occur as angle of attack increases from location B, cruise, to location C, maneuver and combat. Above an angle of attack of 8 degrees brings the onset of buffet if the slats are not deployed. Deploying the slat, the dashed line, delays onset by a few degrees. Wing rock occurs with further increase in incidence, then gets into heavy buffet caused by massively separated flow, stall at maximum lift and eventual departure from controlled flight. Active use of the slats can delay these phenomena, but not eliminate them.

Current limitations to CFD simulation of such separation phenomena are a primary inhibitor to expanding the use of CFD into broader regions of the aircraft performance envelope. RANS has enabled useful CFD applications to many attached-flow situations. It has only had limited successes for separated-flow simulations, and it appears likely that time-accurate hybrid RANS/LES simulations (or better) may be needed for CFD to penetrate the separated flow problems that lead to further types of interactions with shocks and boundary layers, all of which are domains relevant to aircraft operations. The next section discusses the main physics implied in these phenomena.

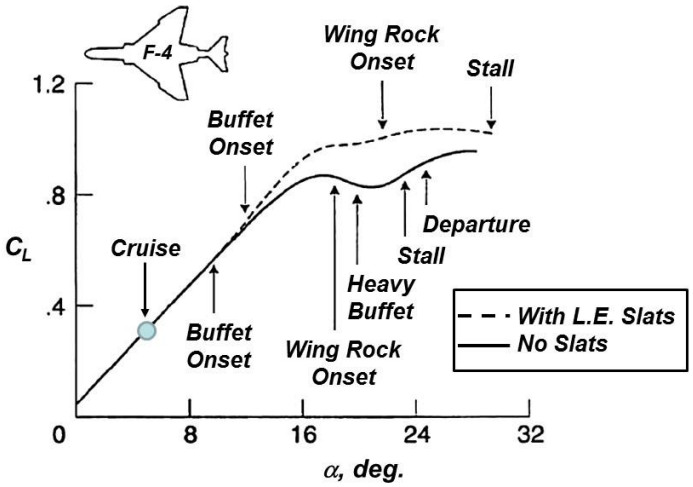

Figure 11-4: Lift curve variation for basic F-4 and F-4 with leading-edge slats. Hall[4]

2.2 Flow Physics Challenges and Consequences

Let us look more closely at the three fundamental separation phenomena occurring in the scenarios described above.

2.2.1 Smooth-Surface Separation

We have mentioned two broadly descriptive notions of separation: bubble-like and vortex-shear (sheet) separation, both of which occur from smooth surfaces. Be aware that separation is an inherently 3D phenomenon, nevertheless it is useful, and easier, to discuss bubble separation in a 2D context.

Figure 11-5 spells out a succession of separation classes, and physics, which occur on airfoils as summarized by Polhamus.[5] These stall patterns encompass flow physics with various combinations of laminar separation, turbulent reattachment, and turbulent separation or reseparation. Domains for these separation classes have been characterized experimentally into a similarity parameter space based upon leading-edge radius and Reynolds number. Through basic wing theory principles, these types of flow separation may occur on swept and tapered wings and can define the wing stall characteristics in the vicinity of $C_{L,max}$. Indicated by the black areas, bubble separation along the lines that Figure 11-5 suggests are relevant for wings of low to moderate sweep and low to reasonably thick airfoil profiles. For more highly swept wings, Polhamus[5] also demonstrated correlation of turbulent reseparation with the onset of nonlinear vortex-lift characteristics.

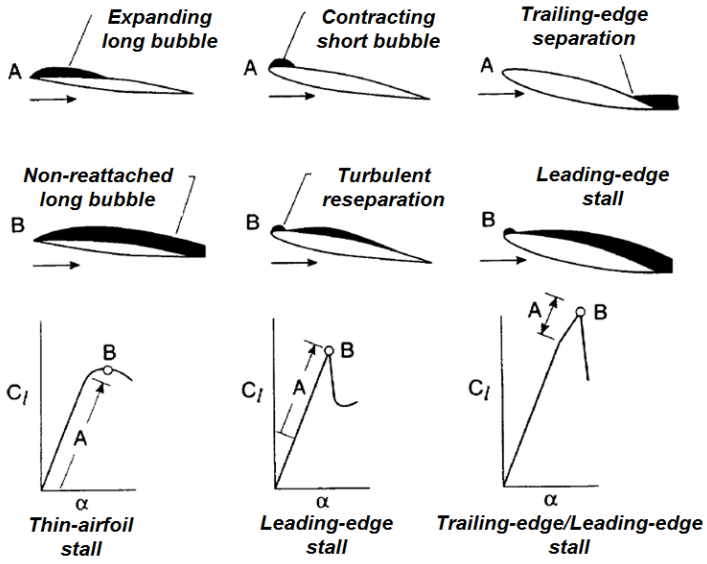

Figure 11-5: Classification of smooth-surface airfoil stall characteristics. Polhamus[5]

For wings of high sweep and thin profiles, separation likely takes place at the leading-edge, and here the notion of bubble type does not hold. Instead, smooth separation in this case implies that wall-streamlines on the body leave the surface and continue into the flowfield as a vortex layer/sheet that, under self-induction, rolls up into a vortex, see Figure 11-6. It also follows from this theory that the separation can start very gradually, somewhere on the surface.

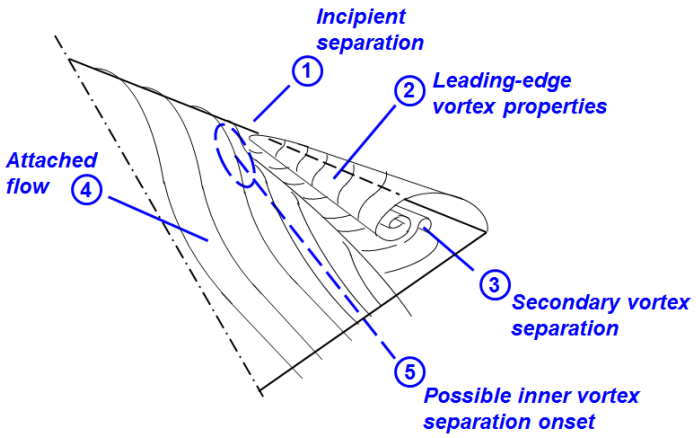

Figure 11-6: Smooth-surface separation, delta wings.

If the leading edge of the wing is sharp, this geometrical feature fixes the location where the vortex sheet leaves the surface and the flow could be handled as an inviscid computation. But when the leading edge radius is increased, (with a cone as a limiting case), the location where the vortex sheet is formed is far from obvious and three-dimensional boundary layer separation must be resolved. The AVT-183 task group analyzed the flow features denoted on Figure 11-6 on the 53°-swept diamond wing in a validation-motivated

approach combining wind tunnel measurements and CFD computations. The resounding conclusion is that details of flow separation along a blunt swept-wing leading edge are extremely sensitive to the numerical and physical modeling approach taken.

2.2.2 Shock wave boundary layer interaction

On transport type wings weak shocks are present at and around the design condition. For fighters, massive separation due to (strong) shock wave boundary layer interaction is a very critical phenomenon that determines wing buffet, and hence the limits of flight. It can also give rise to unsteady phenomena like self-sustained 'limit cycle oscillation' (LCO) of the shock and the boundary layer/wake. The flow image in Figure 11-7(a) taken in a wind tunnel gives an example of massive separation. Figure 11-7(b) spells out in some detail some of the resulting small-scale flow features and the physics involved. Figure 11-7(c) indicates how these small-scale features have substantial large-scale flow effects.

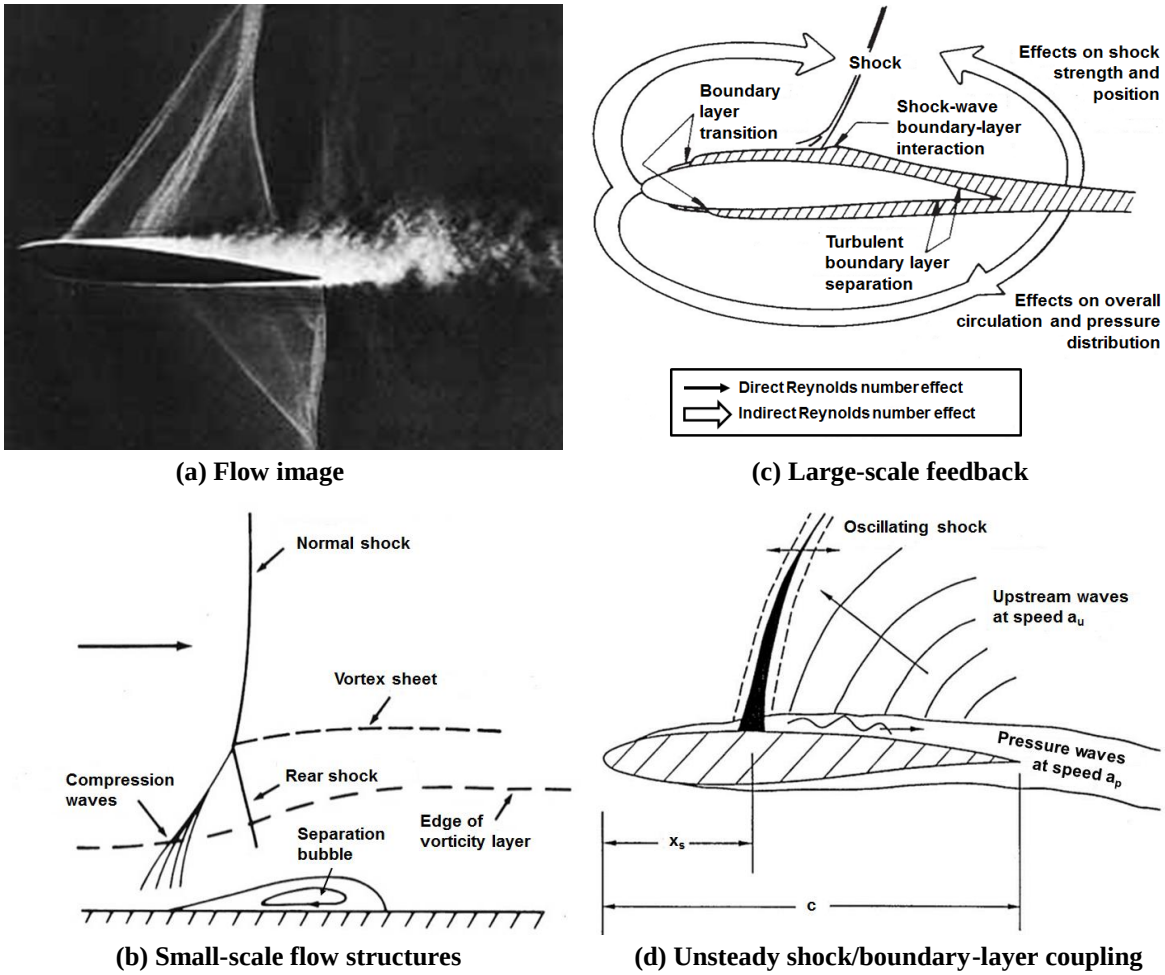

(a) Flow image

(c) Large-scale feedback

(b) Small-scale flow structures

(d) Unsteady shock/boundary-layer coupling

Figure 11-7: Shock wave boundary layer interaction – small scale and large effects.

For example, the combined effect of the shock wave boundary layer interaction and the subsequent downstream boundary layer development determines the condition at the trailing edge. And this in turn affects the overall circulation and hence the shock wave strength as indicated schematically in Figure 11-7(c). Since the shock wave boundary layer interaction and the wave drag, are very sensitive to shock strength, all the ingredients are present for a complicated Reynolds number sensitive viscous-inviscid interaction that can be either steady or unsteady.

Figure 11-7(d) illustrates self-sustained shock oscillation during transonic buffeting with fully separated flow

where the shock wave oscillates on the upper surface of the airfoil about a mean position x_s. The shock movement sends pressure waves propagating at a velocity a_p downstream in the separated flow region. On reaching the trailing edge, the disturbances generate upstream moving waves at velocity a_u, either from the wake fluctuation or from the trailing-edge boundary layer. These waves then interact with the shock and impart energy to it that maintain its oscillation. More thorough treatments of shock/boundary layer flow physics can be found in the books by Babinsky and Harvey[6] and by Vos and Farokhi.[7]

The flow variations resulting from insipient separation are generally gradual and continuous, until the point is reached when 'massive separation' occurs (involving a topological change in the overall flow field), e.g., Figure 11-7(a). If the shock is sufficiently weak, a little bit of separation at the trailing edge, causing some extra drag, is not necessarily bad. This is somewhat similar to the situation at the optimal lift/drag ratio of a transonic wing where a weak shock is normally present and the resulting wave drag is accepted.

2.2.3 Transonic/supersonic shock-vortex-boundary-layer interactions

Figure 11-8 is a shadowgraph taken in the wind tunnel for a slender delta wing at incidence and supersonic speed M = 1.1, where “B” labels the bow shock wave, “V” the shed leading edge vortex, and “S” a shock wave interacting with the vortex, causing what looks like vortex breakdown. With this shock one can also expect SBLI to take place. This is yet another example of the complexity of these interacting flow features.

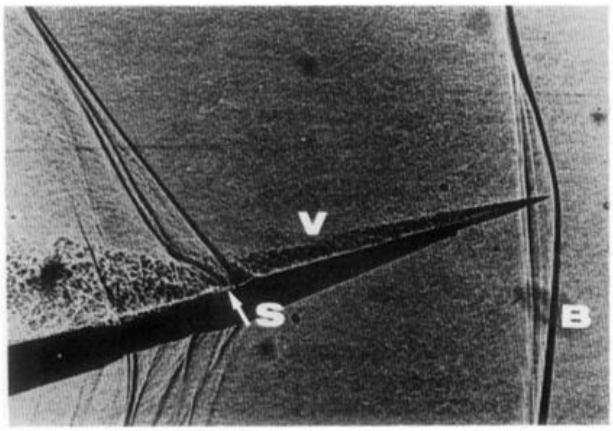

Figure 11-8: Multiple high speed interactions: shock vortex boundary layer.

2.3 Separated Flow Classification

The previous section identified some of the flow physics and complex interaction effects associated with separated flows. Additional flow physics, such as boundary layer transition and confluent boundary layer interactions, can also be present at conditions for which the separated flow effects are consequential to vehicle performance. In practice, these separated flows have become grouped into flow types related to vehicle components, a number of which have been selected as organizing principles for this symposium (e.g., juncture and corner flows, wing stall and wake flows, vortex flows).

In developing this article, the authors have chosen an approach to separated flow classification that distinguishes overarching characteristics of the separation, irrespective of the detailed physics of any particular separation phenomenon, in the context of vehicular scales. Three characteristics to classify flow separation have been chosen:

1. *Class of separation*. This characteristic relates the separation scale to boundary layer length scales, and is characterized as varying from mild to massive separation. For mild separation, relatively steady and thin separated flow regions occur near the surface where wall-bounded turbulence models could be valid. Fluctuations of the separated flow would be comparable to turbulence. For massive separation, unsteady large fluctuating flow regions occur in the flowfield beyond boundary-layer length scales. Fluctuations of the separated flow would be comparable to large eddy effects.
2. *Character of separation*. This characteristic addresses the vortical content of the separation, and is characterized as varying from coherent to incoherent states. For coherent vorticity, relatively steady and organized vorticity occurs in the separated flow regions, an example of which would be the sharp-leading-edge vortex from a slender delta wing. Fluctuations of the separated flow could be comparable to turbulence. For incoherent vorticity, unsteady vortices occur in the flowfield, an

example of which would be vortex breakdown for the slender delta wing vortex. Fluctuations of the separated flow would be comparable to large eddy effects.

3. *Scale of separation*. This characteristic relates the scale of the separated flow to vehicular length scales, and is characterized as varying from local to pervasive. Local separation would occur from components of the vehicle, and could take on any of the class or character attributes described above. Pervasive separation would occur essentially at the full vehicle length scale, an example of which would occur for post-stall maneuver of a fighter aircraft or missile.

The first two characteristics address fluid mechanics of the separation, while the third relates the scale of the separated flow to the scale of the vehicle. These characteristics will be included in distinguishing CFD simulation capabilities later in the paper. Development of modeling in CFD for treating separated flow phenomena must be addressed first and is outlined in the next section.

3.0 SEVEN DECADES OF CFD DEVELOPMENT AND APPLICATION

For this article the authors define Computational Fluid Dynamics (CFD) as the branch of fluid mechanics that uses numerical analysis and data structures to analyse and solve nonlinear fluid flow problems. In this regard, we consider analytical and linear solution methods separately from CFD techniques.

A summary for seven decades of CFD development is shown in Figure 11-9. CFD entails a marriage of theoretically-based numerical solution techniques with scientific computing capacity, and on this figure we

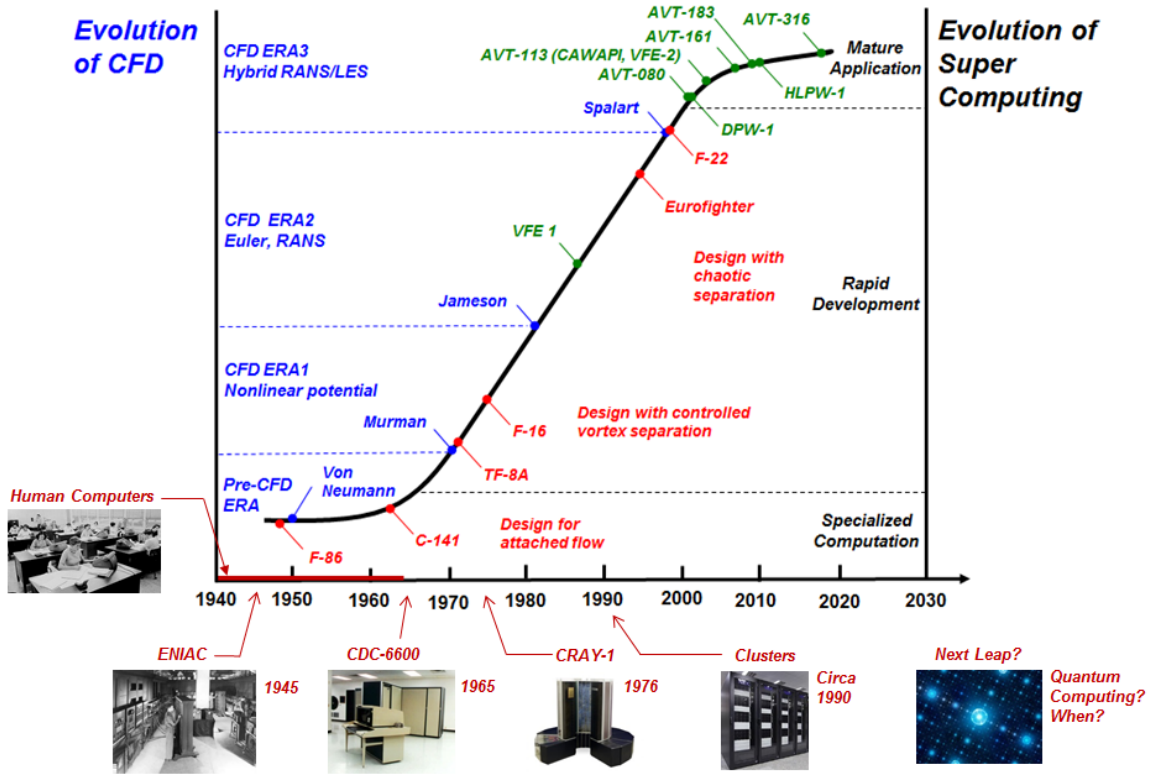

Figure 11-9: Seven decades of CFD.

juxtapose the evolution of CFD (subdivided into eras) with the evolution of supercomputing (also subdivided). The figure also includes select aircraft (first flight date) and collaborative CFD ventures (initiation date).

The pre-CFD ERA includes solutions to linear-potential equations (e.g., transformations and panel methods). During this era, the theoretical underpinnings for CFD were established by von Neumann and Richtmyer[8] in

1950 and scientific computing was limited to human computers and specialized machines, such as the ENIAC. ERA-1 is based on solutions of nonlinear potential equations and was established by the theoretical work of Murman and Cole[9] in 1970. This era saw the rapid development of scientific computing with machines such as the CDC-6600 and the CRAY-1. ERA-2 is based on the solution of the Euler (and shortly thereafter Reynolds Averaged Navier Stokes (RANS)) equations, and was established by the theoretical work of Jameson et al.[10] in 1981. This era saw sustained rapid development of scientific computing with machines such as the CRAY-2 and various cluster-computing architectures.

Covering the first half of this decade (through the end of 1985), Rizzi and Engquist[11] reviewed simulation work of primarily nonlinear vortex phenomena and separation, discussing the numerical modeling involved for computing discontinuous discrete solutions, bringing in the grid generation aspects needed to resolve such phenomena and how the computational methods mapped onto the supercomputing hardware of the day. Their review concludes with a number of computed examples exemplifying the status of CFD, circa 1985, for computing such nonlinear flow phenomena. In addition, Vos et al.[12] extensively reviewed, from a European perspective, the ERA-2 RANS CFD technology for numerous problems in aircraft design.

ERA-3 is based on the solution of unsteady flows with hybrid RANS/Large-Eddy-Simulation (LES) techniques and was established by the theoretical work of Spalart et al.[13] in 1997. This era saw the mature application of scientific cluster computing but it also has seen a decline in the ability of scientific computing capacity to meet contemporary CFD needs. Vos et al.[12] also discussed several early unsteady flow applications using DES physical modelling.

Throughout these seven decades CFD development has taken the form of climbing a ladder of ever increasing physics simulation and, along the way, expanding the ability to represent geometric complexity for aircraft applications. Much of this work was enabled, in part, by rapid advancements in supercomputer capability. Details for the evolution and use of these collective CFD techniques are described in the following subsections, beginning with work that led to the origins of CFD.

3.1 Origins of CFD: Supercritical Aerodynamics

Transonic cruise aerodynamics had been identified as a critical design objective for the swept-wing jet-powered aircraft being developed after World War II. Transonic wind tunnel test techniques had matured substantially due to the introduction of the slotted test section to the NACA 8-Foot High-Speed Tunnel in 1948 (renamed the 8-Foot Transonic Tunnel) as well as due to the subsequent development of other large transonic tunnels. In the early 1960s, Whitcomb experimentally developed supercritical aerodynamics for airfoils[14] and wings[15] (published in 1965 and 1966) with a view toward flight-test demonstration, Figure 11-10.

(a) Wind tunnel model

(b) TF-8A flight-test aircraft

Figure 11-10: Supercritical aerodynamics concept development.

Viscous effects were known to be important to supercritical aerodynamics and this included care for shock/boundary-layer interaction effects embracing both attached and separated flows. One example of separated flow concerns occurred in early flight testing of the C-141 aircraft, Figure 11-11. This aircraft was developed before supercritical knowledge had matured, and ground-to-flight Reynolds number effects resulted in a strong shock at an aft location, which separated the boundary-layer flow (Loving[16]). New physics-based wind tunnel test techniques were developed (e.g., Blackwell[17]) to resolve this

ground-to-flight Reynolds number issue.

During this supercritical development era there were no CFD methods to simulate a supercritical flow, even with inviscid assumptions. Viscous supercritical flows would be more difficult to simulate, and viscous supercritical flows with separation even more so. In addition, Whitcomb's successful experimental methods to develop supercritical shapes were time consuming, and interest developed to seek numerical technology to help accelerate the development process and possibly to add insight to these complex flows.

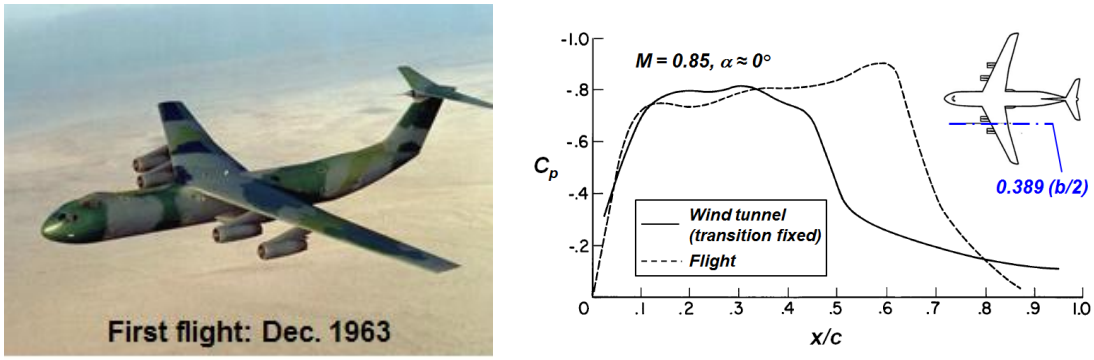

(a) C-141 aircraft **(b) Supercritical pressure distributions**

Figure 11-11: Ground-to-flight discrepancy.

3.2 Development of CFD

Supercritical aerodynamics had been identified as a critical technology for future aircraft, and CFD was originally developed to simulate attached supercritical flows. Supercritical flows are mixed type (elliptic/hyperbolic) and require, as a minimum, the solution of nonlinear potential equations with some ability to capture shockwaves. It so happened that at the time of Whitcomb's first supercritical airfoil paper (1965) coincided with the introduction of the Control Data Corporation CDC-6600, generally considered to be the first successful supercomputer. This became a confluence of (i) a US national need for supercritical aerodynamics, (ii) a scientific challenge for new solution capability of nonlinear fluid flows, and (iii) a new capacity for scientific supercomputing.

The authors have chosen to organize this summary of CFD development into three parts, roughly in chronological order. First is the development of large-scale physics simulations. This will span CFD ERA-1 (nonlinear potential) and a portion of CFD ERA-2 (Euler and laminar applications from RANS). Next is the development of methods to represent complex geometries. Finally is the development of small-scale physics simulations. This will span the remainder of CFD ERA-2 (turbulent applications from RANS) and CFD-ERA 3 (hybrid RANS/LES).

The authors have selected examples to illustrate the CFD evolution and that are representative of points they wish to make. Many of these examples come from their own career experiences as well as those of their peers, and it is noted that many other examples are available in the literature (see, for example, Hirschel and Krause[18]).

3.2.1 Large Scale Physics Simulation

In this section, we will include methods to solve nonlinear potential equations, the Euler equations, and the laminar Reynolds-Averaged Navier Stokes (RANS) equations. With these simulations, the only issue is numerical modeling. As one refines the mesh, the solution of the discrete equations (finite difference, finite volume) approaches the solution to the sponsoring partial differential equations. Techniques that also include flow modeling (e.g., a turbulence model) are addressed in Section 3.2.3, Small-Scale Physics Simulations.

3.2.1.1 Potential Flow

The simplest formulation for transonic aerodynamics simulation is a nonlinear potential flow. By virtue of the potential formulation, the flow has been assumed to be isentropic, irrotational and inviscid. The nonlinear potential equation can be further simplified by assuming small perturbation to arrive at the transonic small disturbance equation.

Despite von Neumann and Richtmyer's fundamental work[8] from 1950 for computing hydrodynamic shocks, it took some time during the latter part of the 1960s to develop a viable solution technique for transonic airfoils. The first such method was developed by Murman and Cole[9] in 1970. They developed a mixed-type finite difference scheme capable of transonic simulations with imbedded shocks, and one of their results is shown in Figure 11-12 for a circular-arc airfoil. Results were presented in terms of transonic similarity variables:

$$k \equiv (1\text{-}M^2)/(t/c)^{2/3}$$

$$\tilde{C}_p \equiv \{[M/(t/c)]^{2/3}\}\, C_p$$

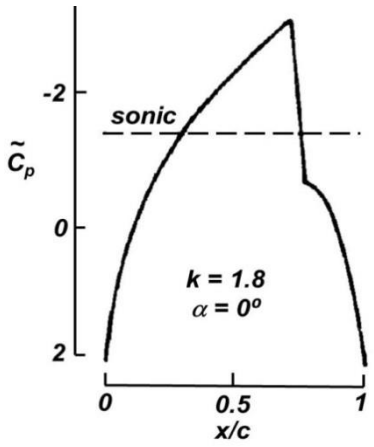

Figure 11-12: First supercritical simulation, circular-arc airfoil. Murman and Cole[9]

Murman and Cole's accomplishment was fundamental and, given the availability of the CDC-6600 class supercomputers, it opened a path for many others to explore similar transonic flow solution methodology. For example, Bailey and Ballhaus[19] developed a method applicable for wing/fuselage solutions in 1975 and Boppe[20] developed a method applicable for realistic configuration solutions in 1978. An example for one of Boppe's solutions[21] from 1980 is shown in Figure 11-13 for a KC-135 tanker configuration. Boppe enabled his transonic small disturbance solutions about complex configurations with an embedded Cartesian grid approach. A notable extension to the transonic small disturbance work was accomplished by Jameson[22], [23] in 1976 with a solution method for the full potential equation that was embodied in a code known as FLO22.

During this era, rotational effects were primarily focused on attached flow interests. The rotational flow physics were confined to narrow regions (boundary layers) and then coupled with the nonlinear potential flow through viscous/inviscid interaction methods. For example, the FLO22 full-potential method and the Mclean[24] 3-D boundary layer method were coupled to provide very useful attached flow cruise aerodynamics simulations for transports.

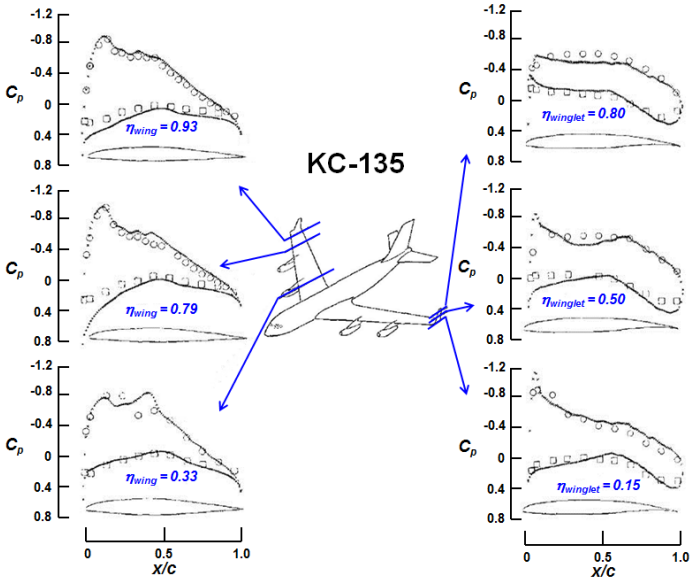

Figure 11-13: KC-135. M = 0.78, α = 2°. Boppe[21]

Separated flows introduce large-scale rotational effects that necessitated explicit modeling during this era of nonlinear potential solvers. These methods generally took the form of discrete vortex modeling (i.e., points, lines, sheets) within a linear potential flow and were not considered as part of the CFD community due to the fundamentally different modeling approaches taken. Two examples follow.

A very successful point-vortex method[25], [26], [27] was developed by Nielsen Engineering and Research (NEAR) company that is still in use at the time of this writing. The method is primarily applicable to slender bodies, and some examples of this method are shown in Figure 11-14.

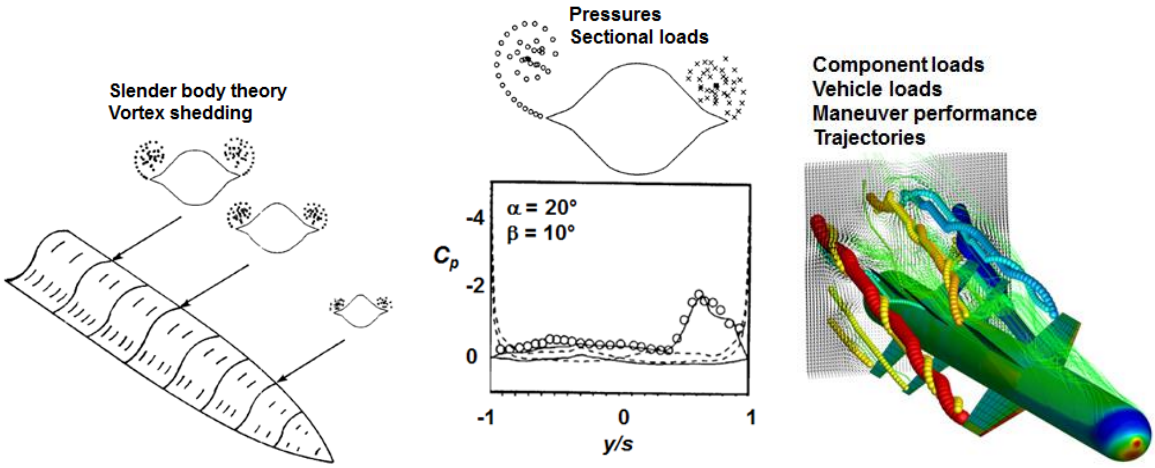

Figure 11-14: Engineering method, vortex points. NEAR Inc.

A successful free-vortex-sheet method[28], [29] was developed by Boeing under contract to NASA Langley Research Center in 1975. This method was based on higher-order panel representations of the leading edge vortex, such as from a delta wing, and provided the first accurate simulations of the 3-D pressure fields for delta wings with leading-edge vortex separation. Some examples are shown in Figure 11-15. The formulation was nonlinear due to the free-vortex-sheet boundary conditions, and application of this method was restricted to simple wing shapes. Other applications of this model are included in an overview by Luckring.[30]

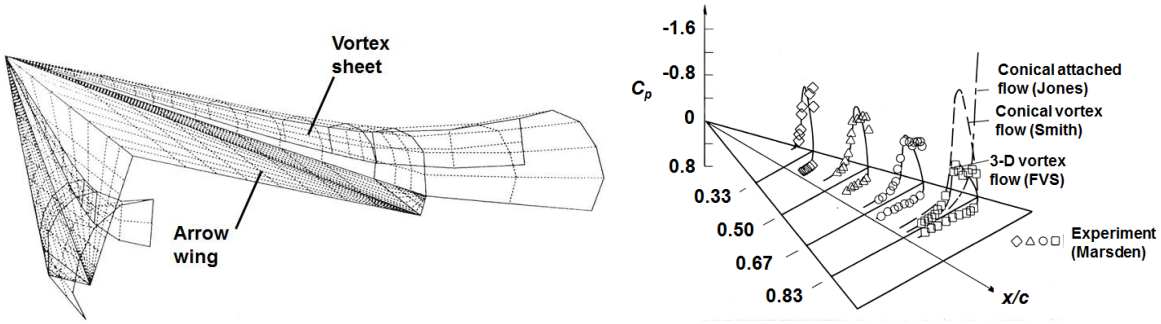

Figure 11-15: Three-dimensional free vortex sheet method.[3.2.9, 3.2.10]

All the nonlinear potential methods of this CFD era were restricted to applications with weak shocks due to the isentropic flow assumption and were limited, for the most part, to attached flow applications. The separated flow methods had their own limitations anchored in the requirement for explicit separation modeling of one form or another. Methods were needed that could capture separation, much in the way potential methods could capture shocks, and this led to the next era of CFD modeling.

3.2.1.2 Rotational Flow

In 1981, Jameson, Schmidt and Turkel[10] developed a new time-stepping method capable of rapidly computing the steady-state solution to the Euler equations to machine-zero levels of the residuals. The numerical technique was based upon a finite volume approach, and this formulation meant that nonisentropic (and nonlinear) flows could be simulated. Rotational flow physics could be contained within the general

computing domain.

Jameson's accomplishment was fundamental, and once again it opened a path for many others to explore similar Euler solution methodology using contemporary supercomputers. One example is shown in Figure 11-16 from Rizzi[31] in 1984 for a sharp-edged delta wing. In this simulation, both the leading-edge vortex and a cross-flow shock between the vortex and the wing upper surface have been captured. Inviscid shock-vortex interactions were now possible to study. Complex configuration analysis capability was developed by Raj[32] in 1987 with the TEAM code, and an example,[33] published in 1991, is shown in Figure 11-17. Many codes were developed and many applications published following Jameson's seminal research.

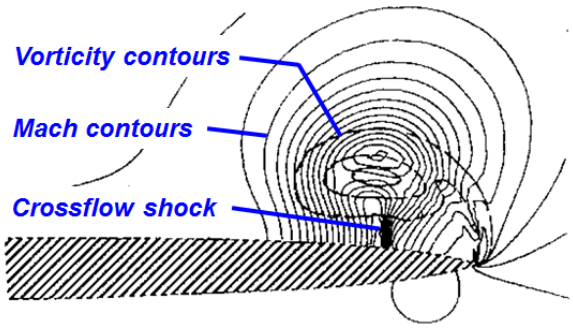

Figure 11-16: Delta wing, $\Lambda = 70°$, $x/c_r = 0.8$. $M = 0.7$, $\alpha = 15°$. Rizzi[31]

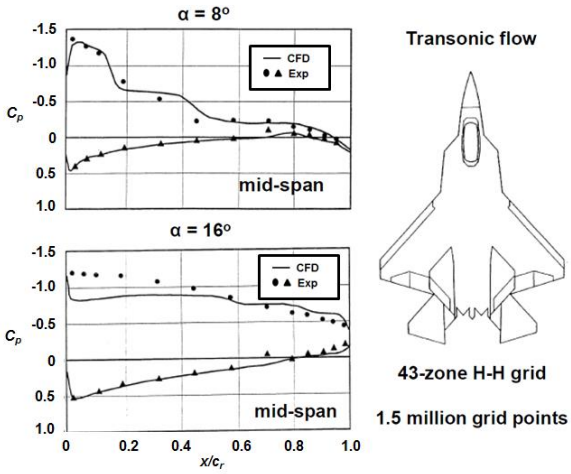

Figure 11-17: Complex configuration. Raj[33]

The Euler capability meant that strong shocks and rotational flow physics could now be captured by this technique. This also opened the door for capturing some separated flows such as from the sharp leading edge of a delta wing. Supercomputer capability was rapidly advancing and this contributed to a capability of solving Navier Stokes equations that included separated flows.

3.2.1.3 Viscous Laminar Flow

Around the time the Euler work was being initiated, other research was underway to provide efficient numerical schemes based upon upwind flux splitting concepts for higher resolution of discontinuities like shocks and vortex sheets. Two notable approaches were developed, first by Roe[34] for flux-difference splitting in 1981, and second by van Leer[35] for flux-vector splitting in 1982. The promise of these upwind approaches, coupled with the rapid supercomputing development of this era meant that tractable three dimensional Navier-Stokes solvers could be anticipated. This meant that nonisentropic viscous flow simulations with separation might be possible within the 1980s.

An efficient algorithm for three-dimensional flow simulations was developed by Thomas et al.[36], [37] in 1985 with applications that included viscous vortex flows and smooth-surface secondary vortex separation at supersonic speeds[38] in 1986 and subsonic speeds[39] in 1987. Solutions were obtained for the Reynolds-Averaged Navier-Stokes equations, with a thin-layer approximation, using a code known as CFL3D, and an example from Thomas' work is shown in Figure 11-18. The solution is for laminar flow about the Hummel[40] delta wing at subsonic speeds. The viscous vortex simulation includes a good estimate of the lift including the maximum lift coefficient, which would include vortex breakdown effects. It also includes good estimates of the spanwise pressure distributions. These pressures are strongly affected by the smooth-surface secondary vortex separation and whether that separation is for laminar or turbulent flow conditions.

Results like Thomas' demonstrated that Navier-Stokes simulations for viscous vortex flows were feasible, at least for simple wing geometries, and many Euler codes evolved quickly to become RANS solvers with variations on the numerical solution details. Because the CFD solution capability was becoming increasingly capable, in terms of flow physics, the interest in applying these methods to more complex and realistic

geometries was growing during this same timeframe. This interest affected method formulations, and a brief discussion of this evolution is presented next.

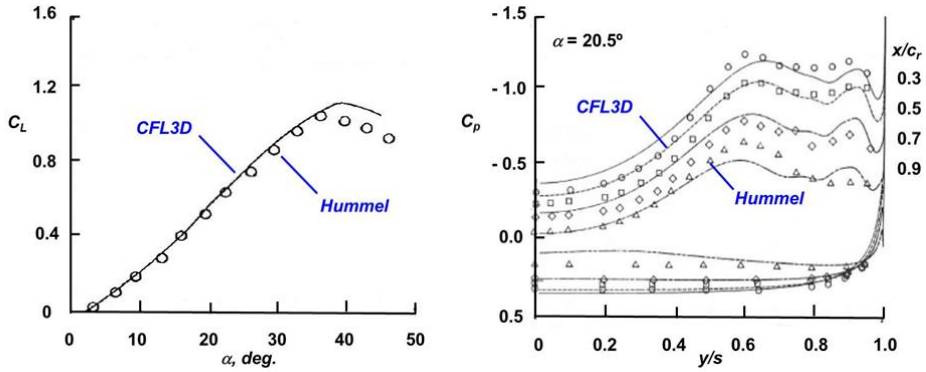

(a) Lift **(b) Pressures**

Figure 11-18: RANS solution, Hummel delta wing, $AR = 1$. $M \approx 0.1$, $Re_{cr} = 0.95 \times 10^6$. Thomas et al.[39]

3.2.2 Advances in Geometric Representation

Aircraft aerodynamics served as the impetus for the development of CFD, and as the ability to simulate more flow physics grew, the interest to more completely represent aircraft configurations also grew. Before discussing this impact on CFD development, it is worth briefly recalling how complex full-scale aircraft and their associated flowfields can be.

An example for a military transport and a fighter are shown in Figure 11-19. The transport is shown in a high-lift takeoff condition, and several challenges for CFD simulation are also noted. These include (i) nacelle strake vortices and their interaction with the wing, (ii) slat and flap gap flowfields along with the associated confluent boundary layer effects, (iii) landing gear and cavity unsteady flows, (iv) propulsion/airframe interactions, and (v) ground effect. A list of challenges is also included for the fighter aircraft, and both these vehicle classes would have additional challenging features for CFD simulation.

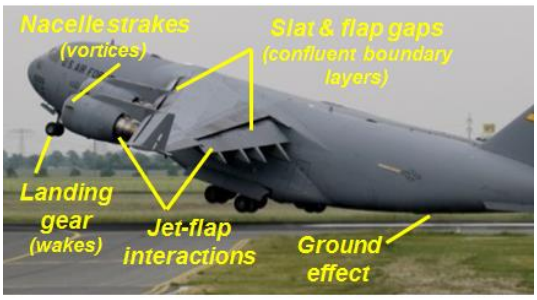

(a) Transport, C-17.

Military aircraft are complex and operate over a broad range of conditions that often include separated flow aerodynamics. From a CFD perspective, the aircraft components and their associated flow fields require sufficient grid resolution for the flow physics contained in the solver to be manifested. This challenge is further exacerbated by the requirement for simulations at full-scale Reynolds numbers, and even more so for the unsteady flows that are important to the expanded envelope flight of many military aircraft. Grid resolution estimates, with contemporary technology, can result in 20 to 40 billion cells to meet these full-scale aircraft simulation needs. Adaptive grid technology may soften these needs, although the adaptation will need to be performed not only in space but also in time for the unsteady flows.

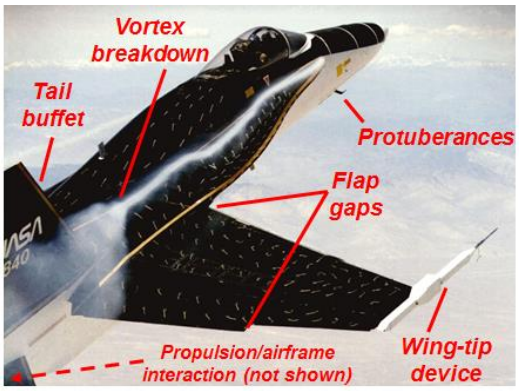

(b) Fighter, F-18 HARV.

Figure 11-19: Some of the challenges.

Several approaches were pursued to enable CFD simulations about complex geometries, and a snapshot of these approaches is shown in Figure 11-20. Boppe[20] used Cartesian imbedded grids in 1978 to enable the transonic small disturbance simulations about full aircraft geometries, and an example of his results was shown in Figure 11-13 This same idea has been exploited by Aftosmis[41] for the contemporary Euler solver Cart3D, and one example of the grid is shown in Figure 11-20(a). Blocked-structured grids offered a second approach, and an example from Ghaffari[42] is shown in Figure 11-20(b). A significant development of overset grid technology was introduced in 1985 by Benek[43], [44] that allowed components (such as a wing and a body) to be gridded independently and then interfaced by inserting one grid into a void from the other grid such that both grids overlapped, Figure 11-20(c). This work led to the flow solver OVERFLOW developed by Buning[45], [46] which evolved to support the emerging RANS CFD capability and resulted in one of the principle computational technologies used to this day. Finally, a significant development for unstructured grid technology was pioneered by Pirzadeh[47], [48], [49] in the early 1990s as supercomputer advancements contributed to the practicality of unstructured-grid flow solvers. The unstructured grid work originally supported Euler simulations and later evolved to support RANS solvers such as USM3D by Frink,[50] Figure 11-20(d).

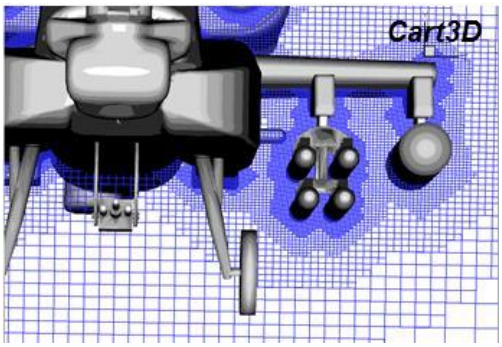

(a) Imbedded Cartesian grids

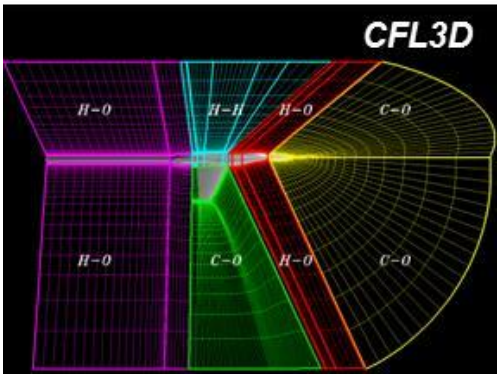

(b) Blocked-structured grids

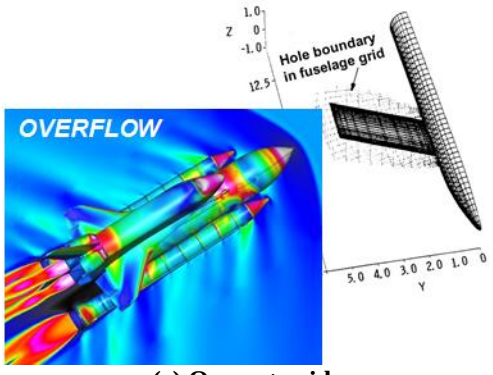

(c) Overset grids

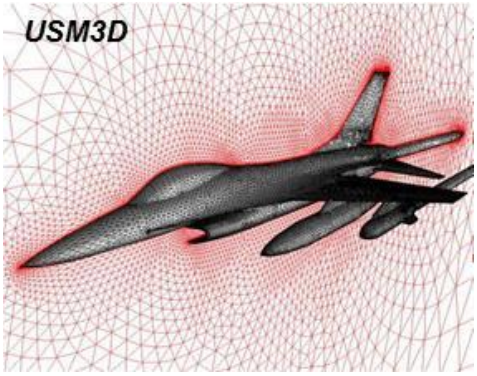

(d) Unstructured grids

Figure 11-20: Some of the solutions.

All of these gridding approaches remain in use at the time of this writing. In many cases, a particular domain discretization approach is closely coupled with a particular CFD flow solver. All of these approaches have enabled the flow solver technology to be applied to fairly realistic representations of full-scale geometries in support of configuration aerodynamics interests. The more recent advancements for adaptive grid techniques will be addressed later in this paper.

3.2.3 Smaller Scale Physics Simulation

The flow physics and associated equation sets from section 3.2.1 could all be resolved with numerical methods using available supercomputing resources. Direct numerical simulations with smaller-scale physics, such as fluctuations within a turbulent boundary layer, greatly exceed available computer resources except for very simple flows. Computation of turbulent flows therefore introduces the requirement to model these flow effects. Flow modeling needs are not limited to turbulence (transition being another example), and flow modeling introduces a new source of uncertainty and possibly error to the simulation. There is of course quite a legacy of turbulence modeling from boundary layer theory and computation, and many of these legacy methods were now available for application within the emergent RANS CFD solvers. Several examples are provided

in the following sections, first for steady flow simulations with RANS methods and then for unsteady flow simulations with hybrid RANS/LES methods.

3.2.3.1 Steady Viscous Turbulent Flow

The Baldwin-Lomax[51] algebraic turbulence model had been developed in 1978 for the thin-layer Navier Stokes equations and had some capability for simulating mildly separated flows. With this model, a length scale of the attached turbulent boundary layer was determined, and a physics-based extension to the model was developed by Degani and Schiff[52] in 1983 to distinguish boundary-layer viscous flows in the presence of separation-induced viscous vortical flows, such as for a forebody at high angle of attack or from the leading edge of a delta wing. Their extension enabled viscous simulations of turbulent flows in conjunction with separated vortical flows. Many emergent RANS solvers incorporated the think-layer approximation, and the Baldwin-Lomax turbulence model with the Degani-Schiff extension became an attractive model for early vortex flow RANS simulations. Two examples using this model follow.

Vatsa et al.[53] computed the three-dimensional subsonic flow about a 6-to-1 prolate spheroid in 1987 at conditions that had smooth-surface separation of both primary and secondary vortex systems. Results were presented for both a flux-difference-split formulation (FDS, from the CFL3D code) and a central-difference formulation (CD, from a code known as TLNS3D) and included comparisons with experiment from Meier.[54] One example is shown in Figure 11-21, and the correlations among numerical and experimental results for the surface skin friction coefficient and the shear-stress angle were generally good. For this case, the experimental flow was tripped from laminar to turbulent at a body station x/L = 0.2, and Vatsa imposed transition in his simulations to mimic this aspect. Vatsa's study included a higher Reynolds number case as well as a lower Reynolds number case for which transition was inferred experimentally to occur in conjunction with the primary vortex separation. Vatsa imposed transition to mimic this lower Reynolds number flow in his simulations and showed that these transitional results matched experiment much better than did fully laminar simulations. These results implied that, if transition could be predicted (as opposed to imposed), the thin-layer RANS technology could provide useful simulations of the transitional flow.

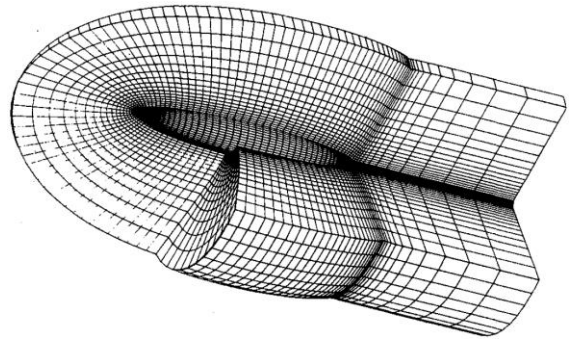

(a) Geometry

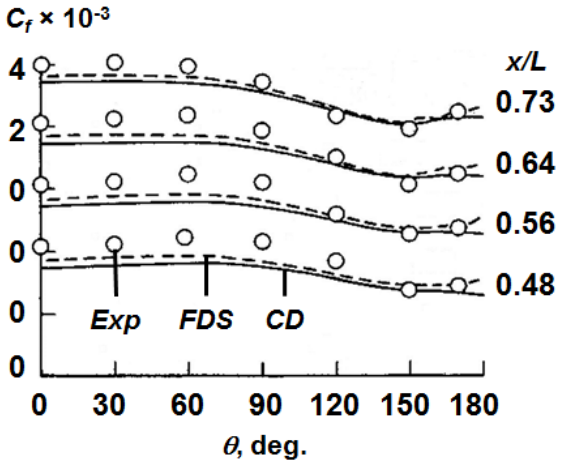

(b) Skin friction coefficient

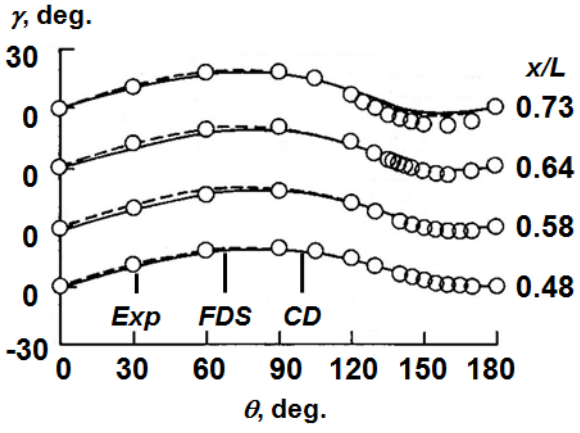

(c) Shear stress angle

Figure 11-21: Prolate spheroid, 6:1. $M \approx 0.1$, $Re_L = 7.7 \times 10^6$, $\alpha = 10°$. Vatsa et al.[53]

In 1989 Ghaffari[42], [55] and his coworkers began presenting turbulent RANS simulations about the F-18 HARV configuration.[56] This was only two years from the fundamental delta wing (Thomas et al.[36], [39]) and prolate spheroid (Vatsa et al.[53]) accomplishments just discussed, and was a fairly rapid leap to complex configuration analysis with RANS technology. At high angles of attack, the F-18 HARV developed forebody vortices (like the prolate spreroid) as well as leading-edge vortices (like the delta wing), and a sampling from Ghaffari's work is shown in Figure 11-22. Turbulence was represented with the Baldwin-Lomax/Degani-Schiff model, and laminar simulations were also performed.

Ghaffari's initial work only modeled the F-18 HARV geometry back to the juncture of the Leading Edge Extension (LEX) and the wing, and these results showed good qualitative agreement with surface flow patterns measured in flight and surprisingly good quantitative agreement for the forebody and forward LEX station surface pressures that had been measured in contemporary wind tunnel tests. Subsequent work modeled the full fuselage and wing, and correlations with flight test pressures were encouraging. The grids for this work were large for supercomputer capacity of that time (1.24 M), but were also identified as being coarse with regard to the flow features being simulated. Two comparisons with flight data are included in Figure 11-22. In this comparison, the flight data are at slightly different conditions from the CFD. Other RANS simulations of the F-18 HARV included more complete geometry, such as the work by Rizk and Gee.[57]

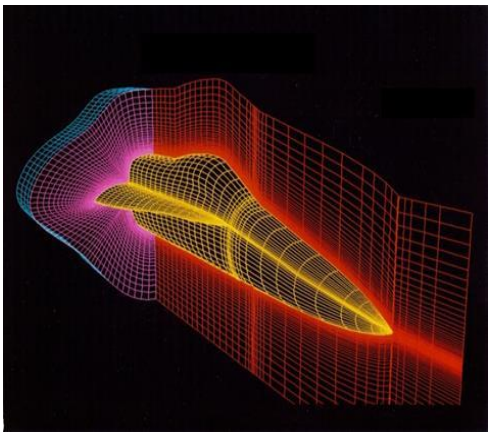

(a) Blocked-structured grid

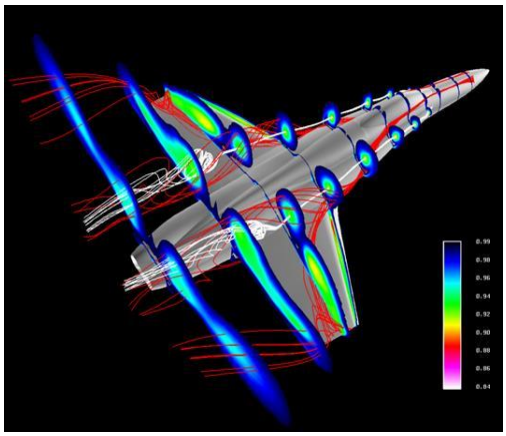

(b) Flowfields

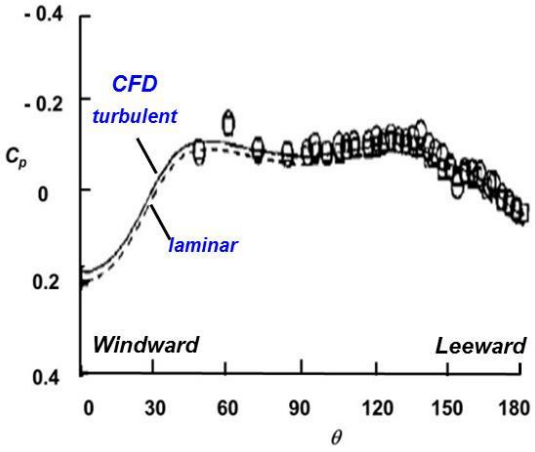

c) Forebody pressures

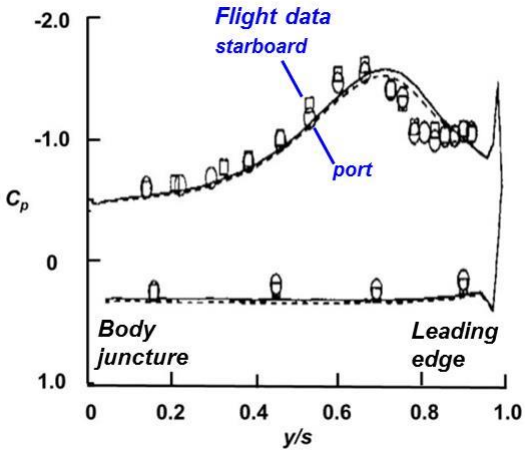

(d) LEX pressures

Figure 11-22: RANS application, F-18 HARV. M = 0.34, Re_c = 13.5 × 10^6, α = 19°. Ghaffari et al.[3.2.22, 3.2.34]

The advancements in RANS solver technology and improved configuration grid capability led to other complex-configuration/complex-flow RANS analyses. For example, transonic viscous flow about a complete F-16A aircraft configuration including power effects was simulated by Flores and Chaderjian[58] in 1988. A more recent example was performed in 2009 by Boelens[59] for the X-31 configuration. Boelens assessed the importance of modeling small details for this configuration, specifically the gaps between the leading-edge flap segments for his turbulent RANS simulations. Recent tests for this configuration had been performed, and Figure 11-23 shows the X-31 wind tunnel model, one of Boelens' grids, and one of his computed flowfields with the gaps represented. In this particular case, the grids representing the flap gaps only produced a small increase in the overall problem size (24.9 vs. 24.7 million cells). However, the flow through these gaps fundamentally altered the wing flowfield by introducing a succession of leading-edge vortices. Without the gaps, the simulations had a single leading-edge vortex. Improved pitching moment correlations with experiment were also achieved with the solutions that included the flap gap effects, and it seemed likely that the flap gap effects observed in this particular study could be important to other swept-wing configurations with segmented leading-edge flaps. It also seems likely that this effect could become more pronounced at the high Reynolds numbers associated with full-scale aircraft. Boelens' work was an outgrowth of another RTO collaboration, AVT-161.[60]

(a) Wind tunnel model

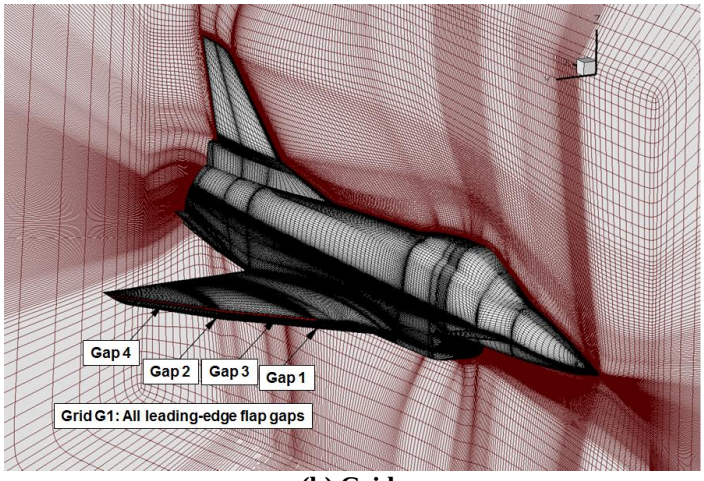

(b) Grids

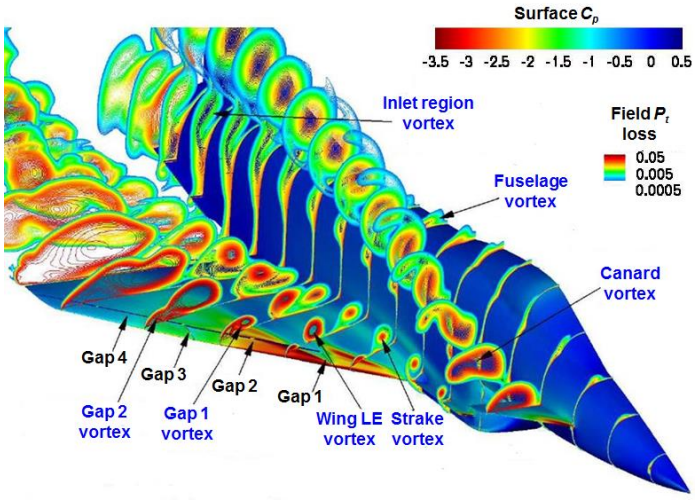

(c) Flowfield

Figure 11-23: RANS application, X-31. $M = 0.18$, $Re_{mac} = 2.07 \times 10^6$, $\alpha = 20.06°$. Boelens[59]

All of the examples discussed to this point have been for steady aerodynamics and steady simulations. The next section addresses a breakthrough for simulating unsteady flows with a hybrid combination of flow solvers.

3.2.3.2 Unsteady Viscous Turbulent Flow

In 1997, Spalart et al.[61] introduced a concept to enable Large Eddy Simulations (LES) to be performed on wings and other more complex configurations. This approach

combined RANS simulation near the configuration, LES simulation in the field, and techniques to interface the two formulations. The LES approach was superior to unsteady RANS for the field simulations, especially as regards separated flows, and the RANS approach provided a means to approximate the near-wall flow physics in a manner that would render the hybrid computations tractable within contemporary supercomputer resources. Unstructured grid technology had already been developed, and the combination of hybrid RANS/LES with unstructured technology was a natural fit. One approach was developed at the United States Air force Academy and embodied in a program known as Cobalt.[62]

Vortex breakdown is one important unsteady phenomenon for leading-edge vortex separated flows. Morton[63] produced promising unsteady results with Cobalt in 2002 for a 70° delta wing being studied under an RTO collaboration known as AVT-080.[64] His simulated vortex breakdown location oscillated between the experimentally determined maximum and minimum locations, Figure 11-24. In 2003, Morton[65] demonstrated improvements to the leading-edge vortex simulation by introducing an adaptive mesh refinement technique. Significantly more vortical content was captured by the adapted mesh solution with only a modest increase in the total number of cells.

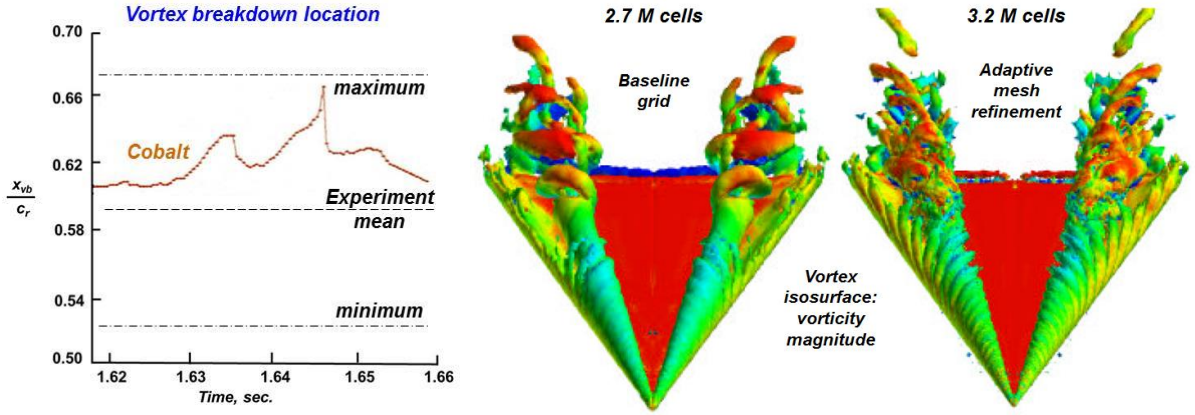

(a) Vortex breakdown **(b) Adaptive grids**

Figure 11-24: Vortex breakdown simulations. $\Lambda = 70°$, $M = 0.07$, $Re_{cr} = 1.56 \times 10^6$, $\alpha = 27°$. Morton[63], [65]

In 2003, Forsythe et al.[66] showed hybrid RANS/LES simulations using Cobalt for a complete F-15E at an extreme angle of attack. Two of his results are reproduced in Figure 11-25. These computations also used the adaptive mesh refinement just mentioned with the delta wing computations. Figure 11-25(a) illustrates the complex and incoherent vortical separations that were captured in this simulation. Figure 11-25(b) contrasts

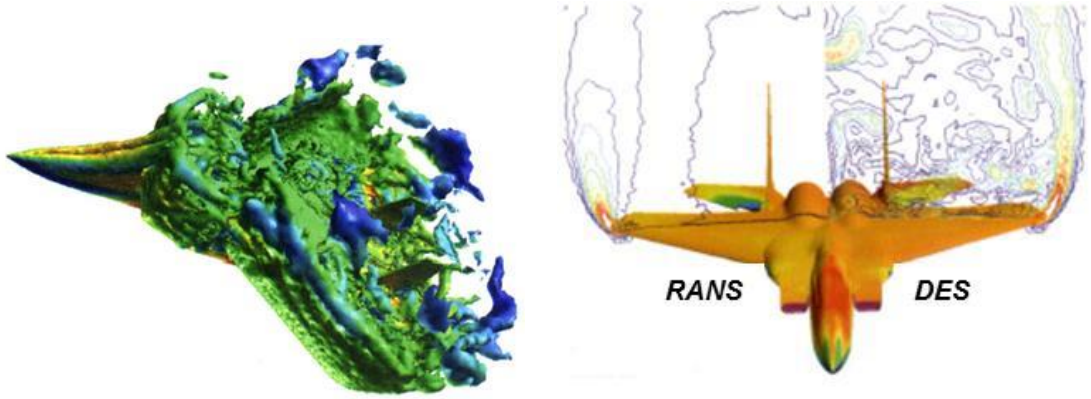

(a) Complex separated flow content **(b) Governing equation effect**

Figure 11-25: F-15E example. $M = 0.3$, $Re_c = 13.6 \times 10^6$, $\alpha = 65°$. Forsythe et al.[66]

unsteady RANS (URANS) and hybrid RANS/LES simulations for this case with massively separated flow. The cut over the wing shows instantaneous vorticity contours and clearly demonstrates the feature resolving capacity of the hybrid RANS/LES approach. Forsythe reported that these URANS simulations did not exhibit any significant unsteadiness, and this solution has virtually no vorticity content over the wing. The hybrid RANS/LES formulation appears to be necessary for simulating flows with significant unsteady separated flow.

Spalart's 1997 hybrid approach for coupling RANS and LES formulations opened a door for many hybrid approaches to be assessed. Especially when coupled with adaptive mesh refinement, this seems to offer a path forward for simulating flows with significant unsteady separated flows. However, guidelines for what exactly qualifies as 'significant' do not appear to have matured. Supercomputer capability has not kept up with the resources needed for these time-accurate hybrid RANS/LES simulations. Despite the fact that the hybrid concept has been around for 20 years, the simulations are still very demanding for current supercomputers, and this has greatly decelerated the learning curve as compared to prior advancements in CFD simulation technology. Additional results from this hybrid technology will be included in the next section.

4.0 AIRCRACFT AND FUNDAMENTAL PROBLEM CASE STUDIES

For this section, the authors have chosen six case studies to highlight some capabilities and challenges for CFD predictions for separated flows. Most topics include both fundamental as well as aircraft assessments, and for all case studies the authors address the underlying flow physics of the separated flow described above. The case studies are presented roughly in an order of increasing flow complexity.

4.1 Controlled Steady Leading-Edge Vortex Separation from Smooth Surfaces

Recent progress has been demonstrated for smooth-surface separation of leading-edge vortices under steady flow conditions. Much of this work led to new physical understanding of blunt-leading-edge vortex separation. Examples are included from two basic studies and one aircraft study.

The first example comes from Vortex Flow Experiment 2 (VFE-2), which was conducted as one facet of an RTO collaboration identified as AVT-113.[67] This work focused on a 65° swept delta wing with a blunt leading edge. Earlier work by Luckring[68] and guidance from Hummel[69] had led to the possible existence of an additional vortex, inboard of the primary leading-edge vortex, that was associated with the blunt leading-edge separation, and new experiments and computations from VFE-2 confirmed the existence of this new vortex. This inner vortex is shown in Figure 11-26 with experiments[70] from DLR and computations[71] from EADS. Additional discussion of these results has been given by Luckring and Hummel.[72]

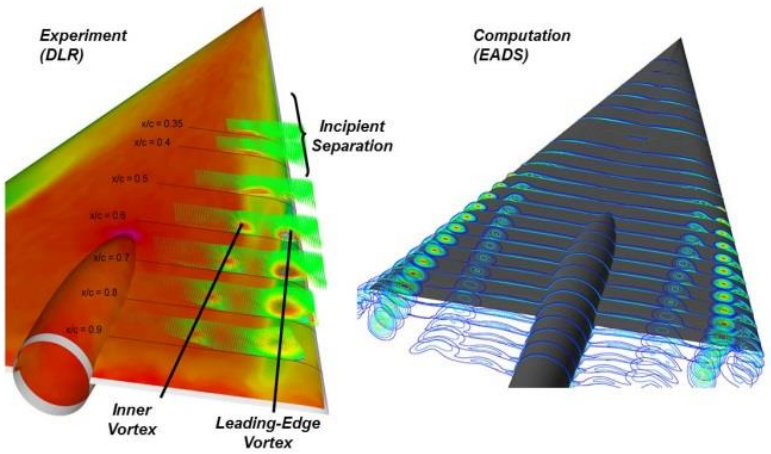

Figure 11-26: Blunt leading-edge separation. Delta wing, Λ_{le} = 65°, M = 0.4, Re_{mac} = 6 × 10^6, α = 13.3°.

The second example comes from an STO collaboration identified as AVT-183.[73] This work focused on a 53° swept diamond wing with a blunt leading edge. This work included new experiments and computations. The work from VFE-2 had identified the existence of an incipient separation region but not many details of this flow. A clearer view of the incipient separation region was established from AVT-183, and one example is shown in figure 11-27(a) with computations from Frink.[74] The inner vortex was found to originate at the downstream limit of the insipient separation region, and the physics of this inner vortex separation was first postulated by Hitzel.[75] The longitudinal location of incipient separation along the leading edge was found to be critical to correlations between CFD and experiment. When this separation location was matched, a good correlation between experiment and computation for the entire wing could be achieved, and an example is shown in Figure 11-27(b) with results from Daniel et al.[76] However, the progression of the separation with angle of attack was not consistently predicted among the CFD results from AVT-183, and this remains a topic for future study.

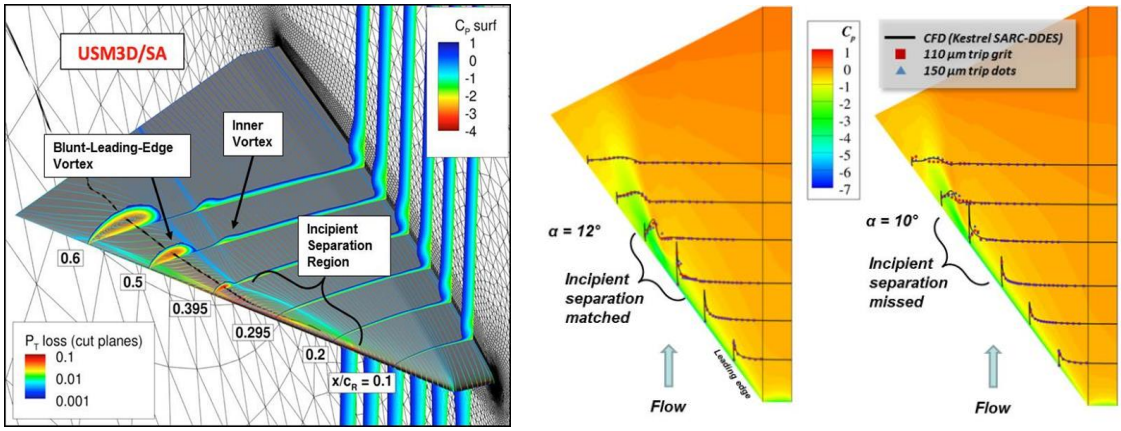

a) Incipient separation, α = 12°. USM3D **b) Correlation with experiment. KESTREL**

Figure 11-27: Effect of insipient separation location on correlation. Diamond wing, Λ_{le} = 53°, M = 0.15, Re_{mac} = 2.7 × 10^6.

The final example comes from another facet of AVT-113[67] that was focused on predicting separated flows from the F-16XL aircraft. This activity was known as the Cranked Arrow Wing Aerodynamics Program, International (CAWAPI), and entailed CFD predictions of flight data that had previously been obtained by Lamar.[77] The conditions included (i) a suite of moderate angle of attack and moderate Mach number conditions along with (ii) a low-speed, high-angle-of-attack condition and (iii) a high-speed (transonic), low-angle-of-attack condition. The work incorporated improved surface modeling and off-body field resolution and detailed CFD assessments. A broad range of flow measurements were obtained with the F-16XL, and a photograph of the research aircraft is shown in Figure 11-28.

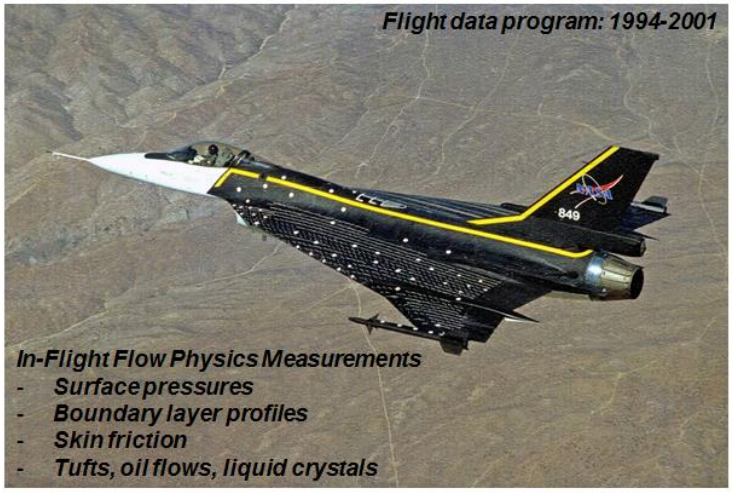

Figure 11-28: F-16XL research aircraft.

Good predictions were achieved at the moderate flight conditions, and one example is shown in Figure 11-29 from Rizzi et al.[78] Here it must be commented that the aircraft wing is comprised of a sharp s-blend near the fuselage, a 70° swept blunt-leading-edge inner wing panel, and a 50° swept sharp-leading-edge outer wing panel. A surface flow pattern is shown in Figure 11-29(a). In this case, the origin of the wing primary vortex is fixed in space by the sharp s-blend (unlike the previously discussed delta and diamond wing flows) but the vortex is fed from the blunt leading-edge of the inner wing panel. Successful correlations among the new CFD predictions and with flight data were achieved, and one example is shown in Figure 11-29(b).

CAWAPI predictions were unacceptable for the two extreme conditions mentioned above. The CAWAPI activity identified a number of possible sources for the discrepancies, and this led to two additional computational campaigns, CAWAPI-2 and CAWAPI-3. One accomplishment from CAWAPI-2 was improved secondary vortex predictions for the low-speed, high-angle-of-attack flight condition, and an example is shown in Figure 11-30 from Elmiligui et al.[79] Secondary vortices form from smooth-surface separation, and through a combination of grid resolution and turbulence model assessments, he achieved the improved secondary vortex resolution with correspondingly improved correlations with the flight test data. In this case, the improved predictions came from the k-ε turbulence model, and it was not clear why this model produced the improved secondary vortex simulation. Discussion of select CAWAPI-3 findings will be presented later in this paper.

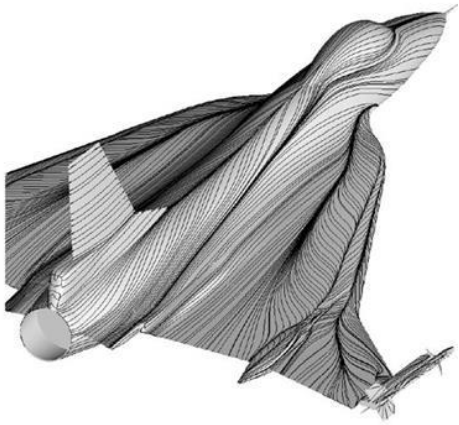

(a) Surface flow pattern

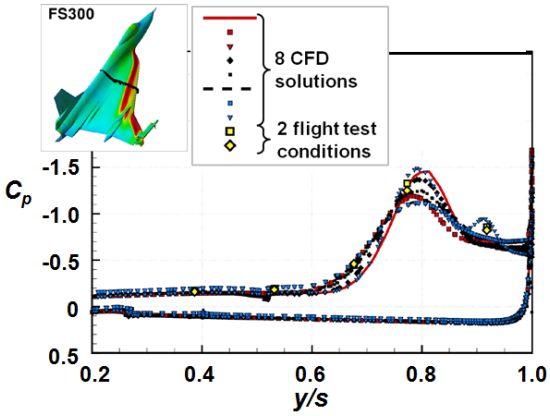

(b) Spanwise pressure predictions

Figure 11-29: Primary vortex predictions, CAWAPI.
***FC-07: M* = 0.304, Re_{cref} = 44.4 x 10^6, α = 11.9°.**
Rizzi et al.[78]

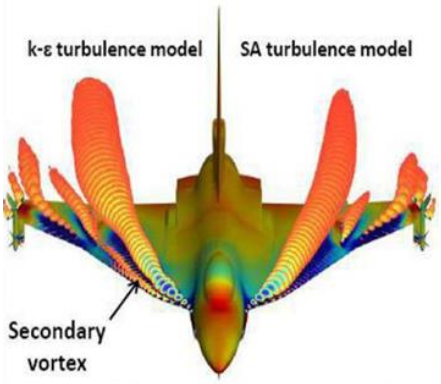

(a) Vortex flowfields

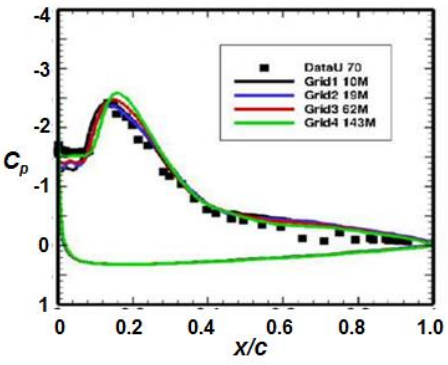

(b) Chordwise pressure predictions

Figure 11-30: Secondary vortex predictions, CAWAPI-2. *FC-25: M* = 0.24, Re_{cref} = 32 x 10^6, α = 19.8°.
Elmiligui et al.[79]

4.2 Unsteady Leading-Edge Vortex Separation

As the previous section explained, at moderate angles of attack, a steady well-ordered vortex develops that enhances the lift of the delta wing. This vortex-enhanced lift increases with increasing angle of attack until the vortex suddenly "bursts" or breaks down into more chaotic rotational motion, at which point $C_{L,max}$ has been reached.

The delta wing vortex breakdown phenomena have been studied extensively since the 1950s. Despite the lack today of a universally accepted unified theoretical interpretation, several forms of vortex breakdown have been identified, namely bubble and helical types, and the global characteristics of the phenomena are understood.

During the breakdown process, the mean axial velocity component rapidly decreases until it reaches a stagnation point and/or becomes negative on the vortex axis. This stagnation point, called the breakdown location, is unsteady and typically oscillates about some mean position along the axis of the vortex core. As angle of attack is increased, the mean vortex breakdown location moves upstream over the delta wing from the trailing edge toward the apex.

The primary vortex over a slender delta wing at angle of attack is principally inviscid, but its location is strongly affected by a secondary vortex formed by the interrelationship between the surface boundary layer and the primary vortex. In addition, the vortex breakdown phenomenon creates turbulent kinetic energy that must be modeled properly or resolved. Many turbulence models create orders of magnitude too much turbulent eddy viscosity in the primary vortex core, which significantly alters the flowfield, and in some cases, eliminates breakdown observed experimentally at high Reynolds numbers.

For these reasons, an accurate prediction of the flowfield over a slender delta wing at high angles of attack and high Reynolds numbers (as well as military aircraft exhibiting vortex breakdown) must model correctly the boundary layer, primary and secondary vortex, and turbulent kinetic energy.

The turbulence models employed in RANS methods necessarily model wall-bounded turbulent motion with no regions of reversed flow, or possibly exhibiting shallow separation, and are unlikely to accurately predict flows characterized by massive separation as in the burst vortex.

Unsteady, massively separated flows are characterized by geometry-dependent and three dimensional turbulent eddies, and these eddies, arguably, are what defeat RANS turbulence models, of any complexity.

For these reasons, researchers currently prefer the so-called hybrid RANS/LES modeling, an early version of which was called Detached Eddy Simulation (DES) because the approach injects eddies, computed by RANS near the wall, and then follows them with LES methodology as they propagate outward into the exterior flowfield. The primary advantage with a hybrid RANS/LES method is that it resolves geometry-dependent, unsteady three dimensional turbulent motions with the LES methodology.

4.2.1 Low Speed Vortex Breakdown over a Sharp-Edged Delta Wing

In his PhD thesis, Görtz [80] computed full-span DES solutions for $M = 0.2$, $Re_{cr} = 1.56 \times 10^6$, $\alpha = 27°$, and extracted the vortex breakdown locations x_{vb} by determining the point along the vortex axis where the chordwise component of velocity equals zero.

Figure 11-31 compares the breakdown locations computed at $\alpha = 27°$ to experimentally measured values by Mitchell[81]. The circles in the plot are the mean measured breakdown locations, the dashed line is a quadratic curve fit to these, and the solid line with crosses gives the minimum and maximum break-down locations measured at $\alpha = 27°$. The star and diamond symbols represent the minimum and maximum computed starboard and port breakdown location, respectively. The triangles denote the breakdown locations computed

on a refined grid. The computed vortex breakdown locations range is $0.789 < x_{vb}/c_r < 0.813$ for the port side and $0.769 < x_{vb}/c_r < 0.797$ for the starboard side.

Figure 11-32 shows a surface contour plot of the time-averaged pressure coefficient C_p for full-span DES (left) and experiment (right). Note that the scale and color map are consistent with the experiment. The upper-surface pressure predicted by DES has an elongated ridge-like pattern, the typical footprint of a vortex. The isobars remain smooth and intact and follow the leading edge until about 80% of the chord, where the contours are constricted, indicating vortex breakdown. Also note the footprint of the secondary vortex close to the leading edges, which the experiment fails to capture. The computed C_p contours are in good qualitative agreement with the experiment, although the suction underneath the primary vortex is underestimated by the numerical simulation.

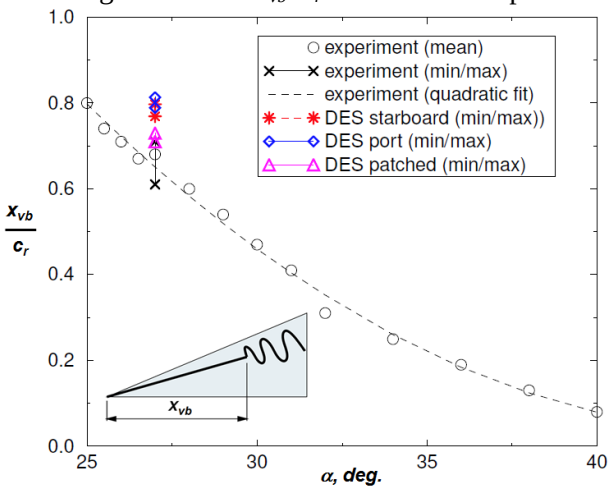

Figure 11-31: Computed vortex breakdown locations compared to Mitchell's experimental data[81].

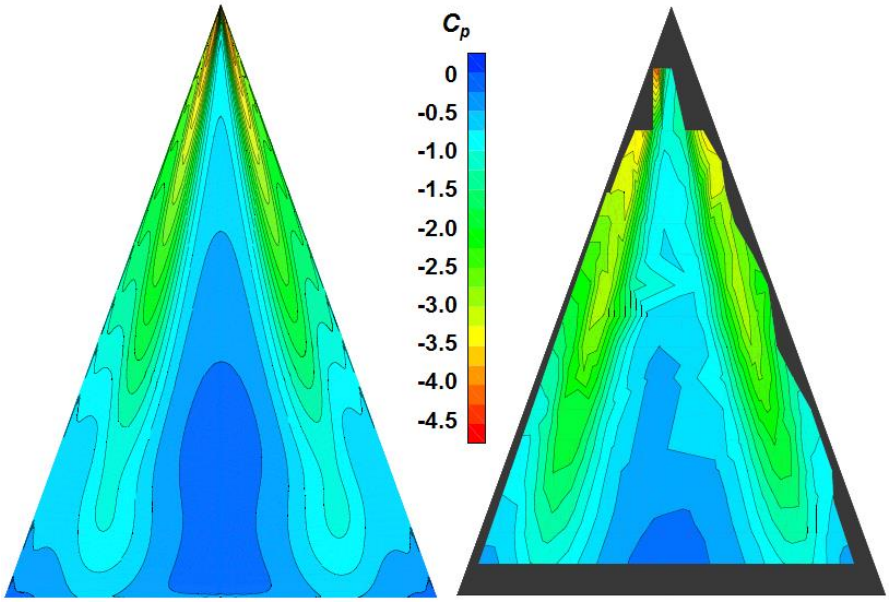

(a) CFD, $M = 0.2$, $Re_{cr} = 1.56 \times 10^6$ **(b) Exp., $M = 0.07$, $Re_{cr} = 1.56 \times 10^6$**

Figure 11-32: Computed and measured upper-surface C_p distribution. $\alpha = 27°$.

4.2.2 Low Speed Vortex Breakdown over F/A-18C

In 2003, Morton et al. [65] were among the first to apply DES to the study of low speed vortex breakdown over the F/A-18C. Applying highly refined grids (including automatic mesh refinement) to the F/A-18C (without the LEX fence) at a condition consistent with vortex breakdown, $M = 0.2755$, $Re_{cref} = 13.9 \times 10^6$, and $\alpha = 30°$, he presents in Figure 11-33 comparisons between steady RANS, unsteady RANS, and Spalart-Allmaras DES (SADES). The resulting predictions are also compared in the AIAA paper[65] with available flight test data for the F/A-18 HARV.

The baseline-grid DES solution shows vortex breakdown occurring at 430 inches aft of the origin and the AMR grid shows vortex breakdown occurring at 475 inches aft of the origin. It should be noted that these are

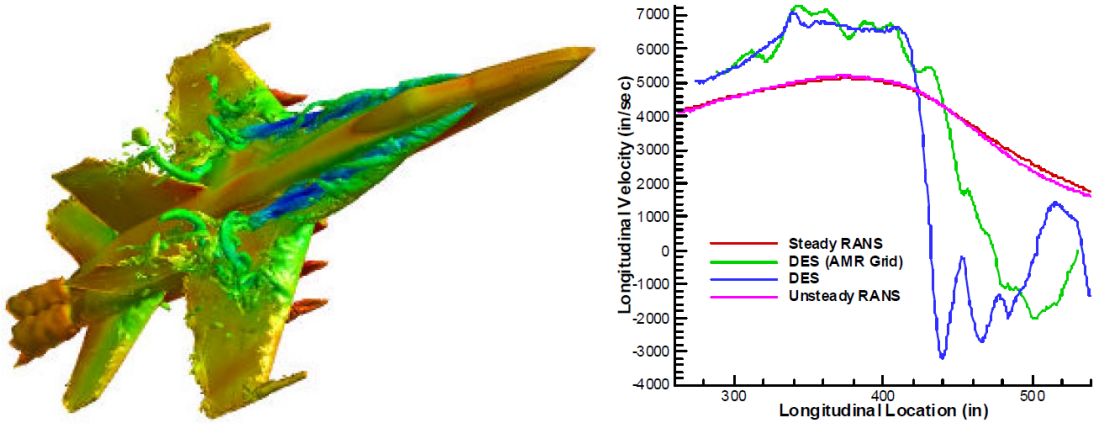

(a) Flowfield, SADES with AMR **(b) Longitudinal velocity in LEX vortex core**

Figure 11-33: F/A-18C solutions. $M = 0.2755$, $Re_{cref} = 13.9 \times 10^6$, $\alpha = 30°$. Morton et al. [65]

instantaneous solutions and the vortex breakdown position can vary up to 10%. These comparisons clearly demonstrate that the DES approach captures the reverse axial velocity in the burst vortex, whereas RANS and URANS do not.

4.2.3 Low Speed Vortex Breakdown over the F-16XL

The collective CAWAPI-2 team, summarized by Luckring et al.,[82] identified two flight conditions for which all the CFD failed to produce acceptable predictions. The first was a low-speed, high angle-of-attack condition that is relevant to takeoff and landing operations. The second was a transonic, low angle-of-attack condition that is relevant to transonic cruise operations.

One of the major findings of this previous CAWAPI-2 work, summarized by Rizzi and Luckring,[83] is that unsteady flow, possibly with the vortex breaking down over the outer wing panel, occurred in the high-alpha case, *FC-25*, namely $M = 0.24$; $\alpha = 19.8°$; $Re = 32.2 \times 10^6$. CAWAPI-3 studied this question further with Hybrid RANS/LES simulations, and results for *FC-25* are summarized here.

This study was focused on unsteady aerodynamic assessments with hybrid RANS/LES methods for the F-16XL aircraft at the low-speed, high angle-of-attack condition. Prior studies, with a focus on steady RANS methods, had failed to produce acceptable CFD predictions of the aircraft outer-panel wing properties as compared to flight test. The new work in CAWAPI-3 included six independent assessments, using five hybrid RANS/LES methods. The overall predicted flow fields were compared, and a combination of steady and unsteady analyses was performed for wing pressures, off-body flow properties, and forces and moments. Correlations among the methods, and with unique flight-test measurements were included.

Comparisons among the methods of the overall vortical flows were quite good. The hybrid RANS/LES simulations showed detailed vortical content and substructure, including stronger secondary vortices than often observed. Exact sources for this were not clear, but could include fine/adapted grids, high Reynolds numbers, the F-16XL geometry, and the inherent modeling capabilities of hybrid RANS/LES methodology. We give an example here.

A standard Q criterion was adopted for visualizing the vortical flowfields about the F-16XL aircraft (where lower values of Q will bring out more vortical content). Figure 11-34 presents an isometric view of vorticity colored by the pressure coefficient over the range $-2.0 < C_p < 0.2$. Four partners provided these results.

Looking at the Kestrel results first, Figure 11-34(c), the dark blue primary vortex from the inner, 70° swept wing is clearly evident. Slightly outboard of this vortex is a lighter blue vortical structure where a secondary vortex would be expected. Further outboard, and close to the leading edge, a tertiary vortex also seems to be indicated.

The secondary and tertiary vortices are small, and they are not commonly seen as distinctly as in the Kestrel-a results. These small, vortical features may be associated with the hybrid RANS/LES modeling, the fine-grid resolution of this solution, the high Reynolds numbers of the target condition, and the F-16XL geometry.

The vortices from the 70° swept wing tear from the leading edge at the break in leading-edge sweep, whereupon the primary vortex appears to burst and the secondary vortex appears to merge with the air dam vortex (both are counter-rotating). On the outer, 50° swept-wing panel, a new leading-edge vortex (dark blue) is seen; and further outboard, this vortex merges with several smaller vertical structures from the tip missile.

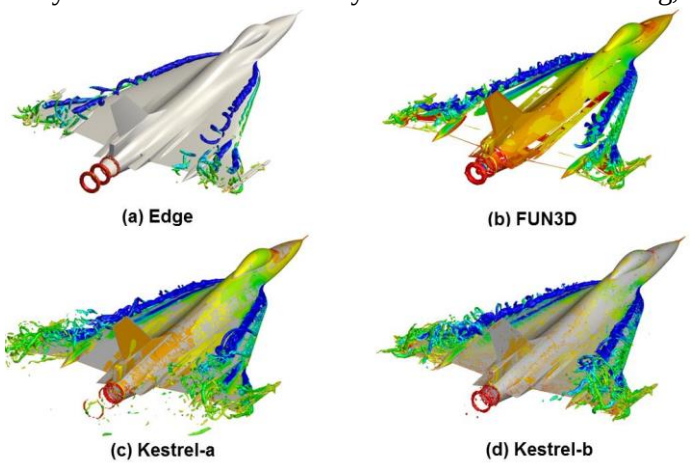

Figure 11-34: Comparison of four off-body flowfields, isometric view. *FC-25*, $M = 0.242$, $Re_{cref} = 32.22 \times 10^6$, $\alpha = 19.84°$.

Turning now to the other solutions, comparisons among the four results with the *Q* criterion are included in Figure 11-34. Results are shown for the EDGE, FUN3D, and Kestrel codes. The results from all four simulations have captured the same overall vortical structures just discussed. All four results look similar at the scale shown over the forward, highly swept portion of the wing. Between the two Kestrel simulations, the Kestrel-b results show more vortical content on the aft portion of the wing. Grid resolution is one factor affecting these images. The FUN3D results show less vortical content on the aft portion of the wing, and this could be due to the relatively small grids used with these simulations. The Kestrel results had fine grids that were also adapted, and the detail in these images may be due in part to vortical grid resolution. The EDGE results had a moderate grid, and the lack of vortical resolution may be associated with the local grid resolution.

Figure 11-35 for *FS-337.5* presents correlation of unsteady pressure coefficients among the methods and with the data that are very good. The methods also show less difference in the secondary vortex region at this station than they did at the previous station (*FS-300*). Unsteady effects now appear to be manifested more in the footprint of the primary vortex. Once again the unsteady effects are similar among the methods.

The unsteady simulations demonstrated that the wing outer-panel flow is very unsteady due to a complex suite of vortex flows and interactions. The collective unsteady predictions for

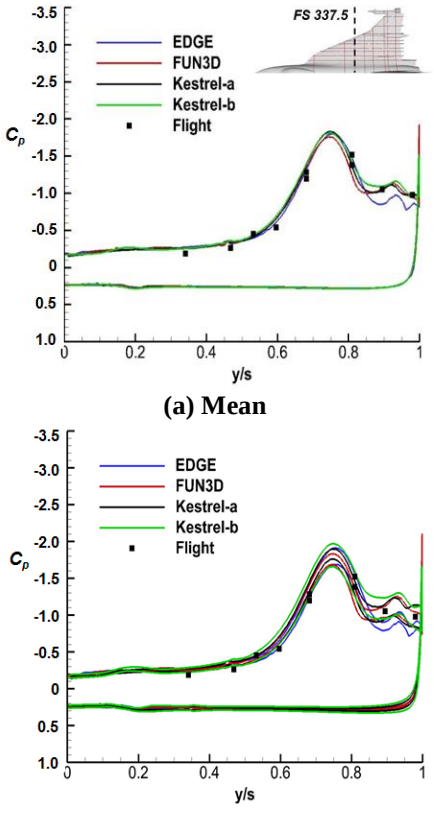

(a) Mean

(b) Mean ± 1 SD

Figure 11-35: Surface pressure coefficients, *FS-337.5*. *FC-25*, $M = 0.242$, $Re_{cref} = 32.22 \times 10^6$, $\alpha = 19.84°$.

the wing outer-panel aerodynamics bound the experimental data, and at least imply that unsteady aerodynamic effects are a significant contributor to the prior discrepancies between flight and (steady RANS) CFD. At other locations, where the flow was predicted to be mostly steady, the correlation among the simulations and with flight test was good. The predicted spatial onset and progression of unsteady effects also agreed fairly well among the methods.

4.2.4 High Speed Vortex Breakdown over a Sharp-Edged Delta Wing

4.2.4.1 Introduction

The occurrence of shocks on delta wings introduces complex shock/vortex interactions, particularly at moderate to high angles of incidence. These interactions can make a significant difference to the vortex breakdown behaviour. For subsonic flows, the motion of the location of onset of breakdown toward the apex is relatively gradual with increasing incidence. At transonic speeds, increasing the incidence angle strengthens the shock and can lead to a shock-vortex interaction triggering breakdown.

The location of breakdown can shift upstream dramatically by as much as 30% of the chord in a single incidence interval of just one degree due to this interaction. This could be called *shock-vortex-breakdown stall,* similar to shock stall - the loss of lift of a moderate-sweep wing as the incidence is increased in transonic flow and SBLI causes the flow to separate. However, a study of the interaction between longitudinal vortices and normal shocks in supersonic flow found that it is possible for a vortex to pass through a normal shock without being weakened sufficiently to cause breakdown, so it depends highly on the specific flight case.

The flow over slender delta wings is potentially more complex as the shock is not necessarily normal to the freestream in the vortex core region. Investigation is needed to consider the behavior and onset of vortex breakdown, particularly with respect to shock/vortex interactions. AVT-113 Facet 2 (VFE-2) studied this behavior as a unit problem in the flow over a sharp-leading-edge slender delta wing under subsonic and transonic conditions. Sample results follow from the work of Schiavetta et al.[84]

4.2.4.2 Transonic Results

Cases with a freestream Mach number of 0.85 were considered, when shock waves are expected to be present. The same angles of incidence were computed, with 18 degrees again giving no breakdown over the wing and 23 degrees resulting in breakdown. The case before breakdown showed similar levels of agreement with the measurements. However, the case after breakdown shows significant discrepancies arising from the premature prediction of vortex breakdown. In fact, the sudden movement of breakdown is predicted about 3 degrees earlier for the CFD when compared with the measurements

Location of Shock Waves. Normal and crossflow shocks were found to occur in this flow. The main focus here is on the normal shocks, which can be identified by plotting the pressure coefficient along the symmetry plane.

Influence of Time Accuracy. The comparison of surface pressure coefficient contours for the time averaged hybrid RANS/LES solutions from the Cobalt and Edge codes shows an overall similar picture, see Figure 11-36. The Cobalt solution shows a more pronounced shock upstream of the apex of the sting fairing, which influences the interaction with the vortex. The Edge solution does not show such a distinct impact of the shock wave on the vortical system and presents a more diluted picture of the breakdown process. In general, there are some differences in breakdown location and shock strength, however, the behavior of the breakdown location motion is very similar in both cases. Analyzing the pressure coefficient fluctuations on the vortex core axis for the Edge solution reveals that the main region of influence of the sting-fairing shock movement is between $x/c_r = 0.54$ and $x/c_r = 0.72$, see Figure 11-35 (b), hereafter the fluctuations are due to the vortex breakdown unsteadiness. Time accurate behavior of the

shock and vortex breakdown movement is considered below. Vortex breakdown first appears on the wing at $\alpha = 20°$, which coincides with a significant increase in shock strength. At this point, it may be assumed that the strength of the shock is high enough to cause a complete reorganization of the flow.

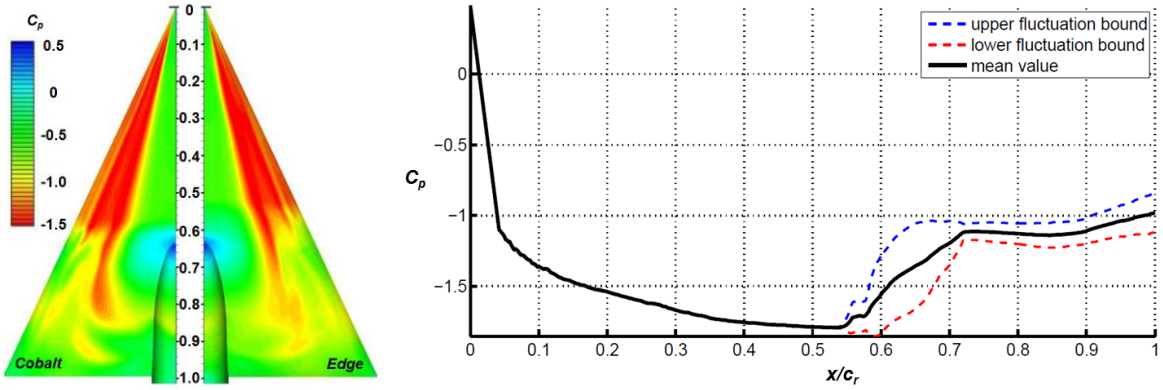

(a) Time-averaged surface C_p **(b) C_p distribution through vortex core, Edge.**

Figure 11-36 Transonic unsteady vortex flow simulations with vortex breakdown. $M = 0.85$, $Re_{cbar} = 6 \times 10^6$, $\alpha = 23°$. Schiavetta et al.[84]

Shock Behavior in Unsteady Solutions. The analysis of all contributed RANS and the time-averaged DES computations reveals the presence of either one or two shocks upstream of the sting-wing intersection. To understand this discrepancy between the otherwise similar solutions, it is necessary to assess the time-dependent flowfield. In this section, the DES computations performed at KTH[85] have been evaluated. This analysis helps to explain the post-breakdown development of the main vortical structures, and also the complex interaction between vortex breakdown and the shock system ahead of the sting.

Figure 11-37 shows the vortex breakdown position history for the last cycle of the Edge solution. The position of breakdown is defined here as the foremost chordwise station where there is fully-reversed axial flow in the primary vortex. It is apparent from Figure 11-37 that the downstream movement occurs relatively suddenly and the upstream recovery is more gradual. The Cobalt predictions show a similar behavior. The reason for the different behavior of the downstream and upstream motion can be found from the flowfield visualization. At the earliest time, a single shock wave is found to propagate upstream ahead of the sting tip at $x_{vb}/c_r = 0.51$ (see Figure 11-36) that with time develops into a twin-shock fore-sting dynamical system that Crippa revealed in his time-accurate solution.[85]

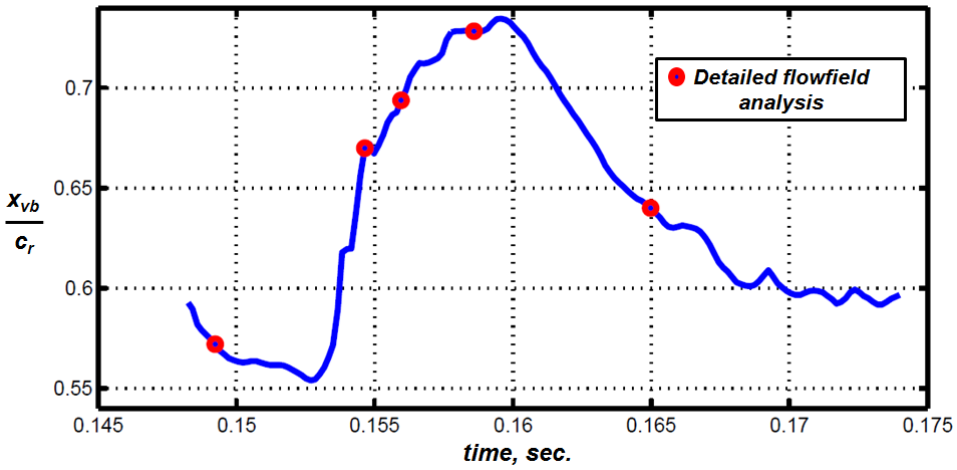

Figure 11-37: Vortex breakdown position for the Edge solution.

Conclusions. The following conclusions are drawn:

- The sudden motion in breakdown location observed in experiments is due to a shock-vortex interaction.
- The CFD predictions of the breakdown movement are insensitive to the simulation details.
- The onset angle of the breakdown movement was predicted about 3 degrees earlier than the measurements. The tunnel interference could contribute to this and should be further investigated.
- The reason for this could be due to the prediction of the shock strength or axial flow in the vortex.
- More detailed measurements of surface pressures and flow field velocities are needed.

4.2.5 Shock-Vortex-Boundary-Layer Interaction - Turbulent and Inviscid F-16XL, *FC-70*

The CAWAPI case of *FC-70* (M = 0.97, Re_{cref} = 89 × 10^6, α = 4°) presents a transonic flow with shock that does not undergo breakdown, and is in fact a steady flow. It presents an interesting, and challenging, case of shock-vortex-boundary-layer interaction. In his PhD thesis, Crippa[85] presents an interesting comparison between an inviscid solution and a RANS solution that brings some insight into the role of the boundary layer.

Figure 11-38 shows the substantial difference in vortex core strength between the Euler solution on the triply adapted "inviscid" grid and the RANS solution on the singly adapted "viscous" grid. Although the geometry of the "S-blend curve" leading edge section that joins the fuselage to the high-sweep section features a sharp leading edge, the high-sweep section features a decreasing radius toward the wing kink, which means that the position of vortex onset in the Euler solution is grid dependent. For the Euler analysis, the discrete grid is responsible for the generation of vorticity and thus, the refinement of the surface grid changes the predicted leading-edge vortex location. By refining the blunt leading edge of the high-sweep section, the separation onset predicted by the inviscid method moves downstream.

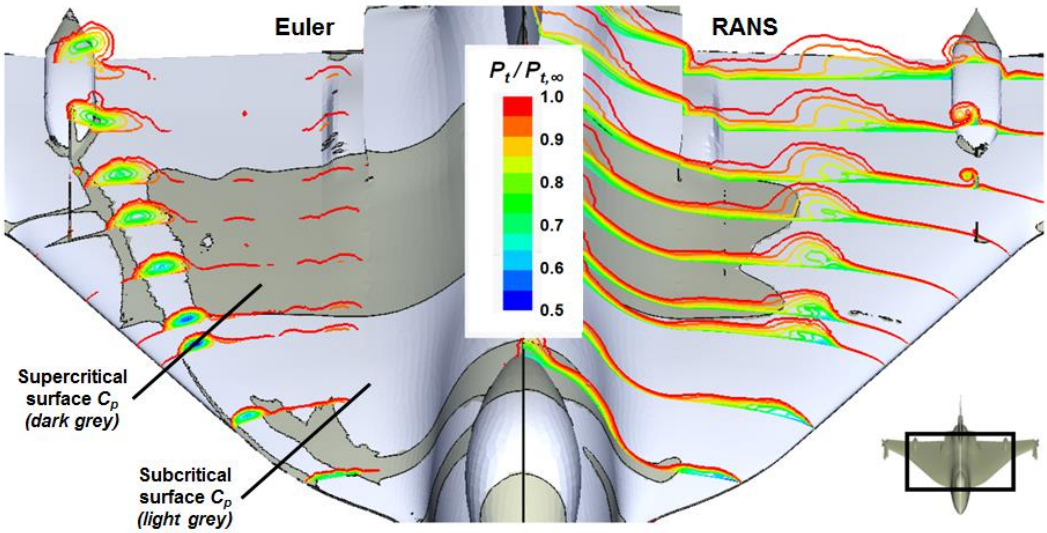

Figure 11-38: Comparison of Euler and RANS solutions on adapted grids for *FC-70*. M = 0.97, Re_{cref} = 89 × 10^6, α = 4°.

Figure 11-38 also presents the topological difference in supercritical regions between the two computations. The supercritical region in the inviscid computation is clearly divided in the chordwise direction by the footprint of the leading-edge vortex. In the viscous result, the supercritical region (dark grey region) extends from the symmetry plane to the midspan, whereby the weaker vortex has less impact on it. Most noteworthy, this comparison indicates a very weak SBLI since there is little difference in the shock location terminating the supercritical regions in the Euler and RANS solutions.

4.3 Unsteady Shock/Boundary-Layer Interaction

An upgrade program for the F/A-18C/D aircraft was initiated in the 1990s and this resulted in the F/A-18E/F Super Hornet with a first flight of the preproduction aircraft in November of 1995. Although this was a derivative program, the F/A-18E/F incorporated significant changes to the wing and the LEX, and early in the flight test, the preproduction aircraft encountered an uncommanded lateral motion, referred to as wing drop, at transonic speeds. This adverse feature led to the 5-year Abrupt Wing Stall Program to identify and resolve this deficiency with experimental, computational, and simulation tools. An overview of this program has been given by Hall et al.[86] in 2005, and a photograph of the F/A-18E in high-speed flight is shown in Figure 11-39.

Figure 11-39: F/A-18E.

New transonic wind tunnel testing included work with a free-to-roll test technique, and this testing was successful in demonstrating the abrupt wing stall behavior that prior rigid-support testing had missed. Further experimental and computational work identified unsteady flow effects on the wing at a span station near the leading-edge snag, and CFD contributed to the understanding of the flow phenomena associated with the abrupt wing stall. Critical unsteady computations were performed by Forsythe and Woodson[87] in 2003 that demonstrated an unsteady flow separation at this span location, Figure 11-40. The solution shows vorticity isosurfaces colored by pressure and separation from contours of zero streamwise velocity (grey). Forsythe performed hybrid RANS/LES computations with an SADES formulation using the flow solver Cobalt.[62] The scale of the separation could be captured with this approach, and the simulation demonstrated a localized but sizeable separated flow region.

Forsythe's results showed a shock-induced boundary-layer separation with a low frequency longitudinal oscillation of the shock and subsequent separation location. Full-span simulations demonstrated that this phenomenon could occur asymmetrically, and the flow image at *time c* in Figure 11-40 illustrates this condition. The separation was further complicated by a small vortex formed from the snag side edge that penetrates the separation zone.

Details of the flow understanding from Forsythe's work were consistent with a growing body of experimental findings, and this unsteady and asymmetric separation became the likely source of the abrupt wing stall. Simulation tools were also used to verify this interpretation, and the separation issue was resolved experimentally through the development and implementation of porous patches on the wing upper-surface fold fairing for the production F/A-18E/F. Unsteady separated flows were central to this issue, and a very effective marriage of advanced experimental and numerical research led to the identification, understanding and resolution of the abrupt wing stall.

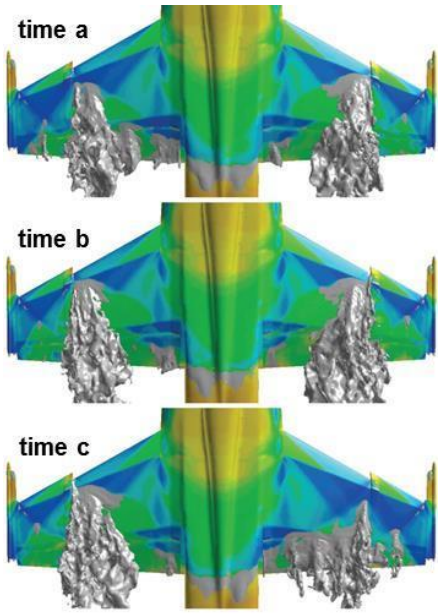

(a) Flowfield

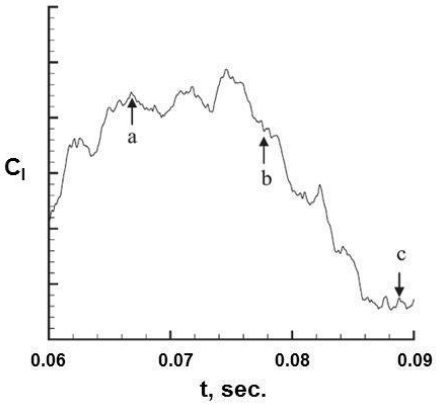

(b) Rolling moment

Figure 11-40: Simulation of abrupt wing stall, F/A-18E/F. $M = 0.9$, $Re_{cref} = 3.98 \times 10^6$, $\alpha = 9°$. Forsythe and Woodson.[87]

4.4 Maneuvering Flight with Flow Separation

Both F-16XL and X-31 programs involved flight tests and wind tunnel campaigns. In CAWAPI, we concentrated exclusively on the flight tests that were available. In X-31 AVT-161, it was the opposite, the flight tests were not offered to us, we concentrated on the wind tunnel measurements.

Historically, most CFD is carried out with comparisons to wind tunnel measurements where the majority of measurements are done with a "clean" model, i.e., no control surfaces and/or high lift devices. This in fact was the case for CAWAPI – except for some simulations by Tomac – all were done with the clean aircraft. In a sense, we are modeling the wrong geometry when we do so. Test pilots of course must use control surfaces to fly even unaccelerated flight.

The F-16XL flight tests we have investigated are straight and level unaccelerated trajectories. Since this aircraft is very nearly neutrally stable, very little trim control is required for these flights, i.e., the control surfaces are little deployed, justifying the use of the 'clean' wing.

4.4.1 "Replaying" a Flight Maneuver by CFD Simulation

In principle, if all the data of a flight test are recorded capturing all the pilot commands, control setting, trajectory etc., then these data can be "replayed" through a time accurate CFD calculation, which features the moving control surfaces, maneuvers, propulsion settings etc., and the computed forces and moments can be compared against the flight test values.

The key functionality for the CFD solver for replay is the ability to move the mesh. Two types of mesh movement are required. First, a rigid rotation and translation is required to follow the motion of the aircraft. Secondly, the control surfaces are deflecting throughout the motion.

The desired motion to be replayed through the unsteady CFD solution is specified in the motion input file. The aircraft reference point location, rotation angles and control surface scaling factors are needed. The rotation angles are obtained straight from the pitch, yaw and bank angles. The aircraft reference point velocity is then calculated to achieve the required angles of attack and sideslip, and the forward speed. The velocity is then used to calculate the location.

Such replay functionality, or "flying the maneuver", is only beginning to be common in CFD codes, where the desired goal would be to achieve virtual flight testing.

4.4.2 Physics: Flow From Accelerating/Oscillating Flight, Vortex-Vortex Interactions, Hysteresis

NASA's X-31 program has shown the feasibility of post-stall flight and the combat superiority of highly maneuverable aircraft. This has called for more research in the domain of maneuvering aerodynamics and in particular, maneuvering delta wings. Both experimental and numerical work has started on simple maneuvers: pitching or rolling wings undergoing forced oscillation.

The major difference between a wing at a fixed attitude and one that is pitching is a hysteretic behavior of the breakdown. By definition, hysteresis is a lagging or retardation of an effect. For delta wings, it means that the effect of the flow conditions (angle of attack, roll angle, etc.) on the vortex is not felt immediately but only after some delay.

Thus, depending on the history of the maneuver, even if the instantaneous flow conditions are the same as a corresponding static case, the flow field can be different. In the case of pitching delta wings, the vortex breakdown position depends not only on the current flow conditions (free stream velocity, angle of attack, etc.) but also on the history of the wing motion, i.e., increasing (upstroke) or decreasing (downstroke) angle of attack. This dynamic position of the vortex breakdown is also dependent on, among other parameters, the

location of the axis of rotation, the amplitude of the motion (initial and final angles of attack) and the pitch rate, etc.

Current and future fighter airplanes are designed to transiently fly at very high angles of attack. This super-maneuverability is now required for dog-fight maneuvers like the "Cobra maneuver" for instance. These new types of maneuvers involve high pitch rates and flight at incidences beyond the static stall angle of attack.

The aerodynamics around a maneuvering fighter is very complex but needs to be understood in order to optimize the airplane design. The good aerodynamic performances of the fighters in high angle of attack maneuvers are often reached thanks to the use of a delta wing.

The aerodynamics of these wings at incidence is characterized by the formation of a pair of strong leading-edge vortices on the leeward side of the wing. The vortices create a zone of high flow velocity with low surface pressures on the wing producing an additional lift compared to classical rectangular shapes. At very high incidence, however, the vortex flow breaks down, a zone of recirculation with a turbulent wake appears and the lift decreases. During maneuvers, the same phenomena occur but the flow has to adapt to the moving planform and thus time-lags are observed in the dynamic response. The prediction and the understanding of the hysteresis loops that form a history of the aerodynamic forces, for example, can be very useful for the designer to extend the limit of the flight envelope during maneuvers.

4.4.3 Basic Studies: Forced Oscillating Delta Wing and UCAV

Figure 11-41 illustrates this phenomenon of "dynamic lift" for a pitching delta wing: in the upstroke motion more lift is created than for the static wing at the same α. This hysteretic lift behavior creates a hysteretic loading of the wing with an overshoot of the static forces in the upstroke motion and an undershoot in the downstroke motion. The advantage of a rapid pitch-up maneuver is obvious with the additional normal force obtained compared to the static case, the so-called "dynamic lift" effect.

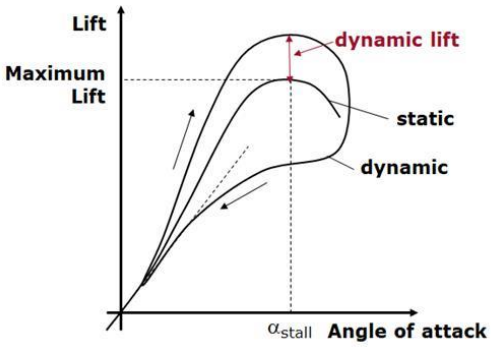

Figure 11-41: Static and dynamic normal force coefficient.

Lemoigne[88] has studied this effect in his PhD thesis with computations of a forced-motion sharp-edge delta wing undergoing pitching dynamics consisting of sinusoidal oscillations defined by the angle of attack law:

$$\alpha(t) = 38° + 6° \sin(\omega t)$$

The axis of rotation is placed at $x/c = 0.4$ and the free-stream Mach number is $M = 0.2$. A static computation at the mean angle of attack is used as the starting point for the pitching computation.

Figure 11-42 plots the computed results for the normal force coefficient compared to the inviscid values. The first important remark is that for the high angles of attack the turbulent results only differ slightly from the inviscid ones: the maximum normal force is a bit lower in the turbulent case and the same applies to the first half of the oscillation in general but the difference is very small.

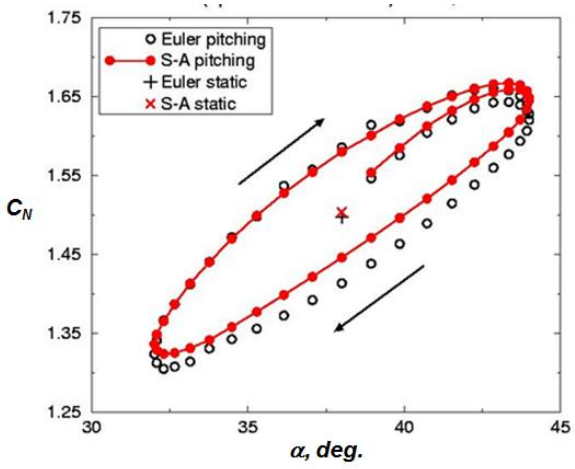

Figure 11-42: Normal force coefficient results for oscillating delta wing. Euler and RANS/SA.

More recently, the collaborative AVT-161 project[60] performed an integrated numerical and experimental assessment of dynamic stability derivatives with hysteresis characteristics for an Uninhabited Combat Air Vehicle (UCAV) with blunt leading edges known as SACCON. Even for static conditions, the separation-induced vortical flows are very complex for this configuration, Figure 11-43. New forced oscillations experiments were performed to establish the dynamic configuration aerodynamics of this vehicle and to guide numerical assessments. The numerical approach requires time accurate formulations, either unsteady RANS (URANS) or hybrid RANS/LES, which incorporate dual-time-stepping schemes. There are two issues involved: (i) the size of the time step necessary to resolve the relevant unsteady physics and (ii) the number of subiterations carried out to complete a given time step. The heart of an efficient numerical procedure lies in understanding the relationship between the number of time steps per oscillation cycle and the subiteration convergence for a representative time step. After exploring various combinations of step size and iteration number, Frink[89] established guidelines for URANS simulations that yielded efficient converged forced-oscillation simulations. Frink et al.[90] summarized some of the numerical findings for three of the codes included in the AVT-161 studies.

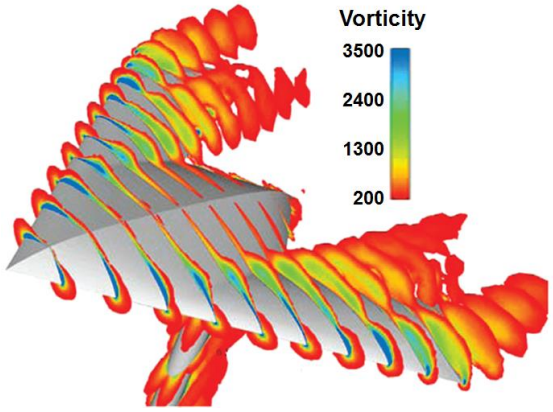

Figure 11-43: SACCON CFD simulation. USM3D, M = 0.144, Re_{cref} = 1.6 × 10^6, α = 16.83°. Frink et al. [90]

4.4.4 Aircraft Study: X-31 Maneuver Aerodynamic Analysis

The X-31 program was a cooperative US/German flight test program with a work and budget share of 50% each. Rockwell built the two aircraft based on a lot of available parts from the F-16. The wing design for example came from Germany (DASA, today Airbus Defence and Space, Manching and Ottobrunn, Germany). The flight control system came as well from DASA, and demonstrated for the first time a full integration of a thrust vectoring device into the entire control system and controller. The real aircraft geometry is still confidential among some partners (quite similar to CAWAPI).

Figure 11-44: X-31.

The X-31 is an experimental high-angle-of-attack delta-wing canard configuration aircraft with lex, strake, and flaps. The aircraft was designed to test thrust vectoring technology and controlled flight at high angles of attack as seen in Figure 11-44. The full scale aircraft has a length of 13.2 meters (including thrust vectoring paddles) and a total wingspan of 7.3 meters. A few details of the X-31 geometry are shown in Figure 11-45.

SHAMAN[27] is NEAR's preliminary design prediction and analysis software tool applicable to configurations operating in pre- and post-stall flow conditions. Its approach is a direct coupling of fluid dynamics and flight mechanics for use in the flight regimes where the flow phenomena are dominated by vorticity and separation associated with high angles of incidence and large values of roll, pitch, and yaw rotational rates.

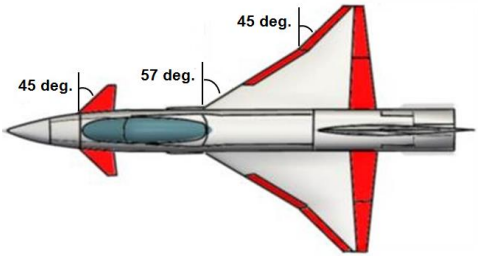

Figure 11-45: CAD model of X-31 aircraft with control surfaces.

SHAMAN has application as a diagnostic tool for the assessment of aerodynamics and flying characteristics of flight test aircraft. In a flight test maneuver of the X-31, the aircraft flies in trim at approximately 25° angle of attack. The maneuver begins with a 180° roll around the velocity vector followed by a rapid pull up. In the flight test, the X-31 departs from the intended trajectory at about 55° angle of attack (t = 15 sec.), Figure 11-46.

As part of AVT-161, Mendenhall et al.[91] applied SHAMAN to this maneuver by forcing the aircraft through the actual measured flight conditions and control deflections. Careful examination of the forces and moments on the vehicle and the associated flow field can provide some insight into the flow phenomena, which may be responsible for the departure.

Figure 11-46 presents the flow angles and angular rates measured during the maneuver. These conditions are imposed on the X-31 configuration in SHAMAN as the vehicle is forced through the actual maneuver and the vortex field is allowed to build and evolve with the changing flight conditions. The measured and predicted aerodynamic forces on the X-31 are compared during the maneuver in Figure 11-47.

The two arrows in Figures 11-46 and 11-47 mark two key flight conditions, one prior to departure (t = 14 sec.) and the other after departure (t = 16 sec.), which are examined in more detail to better understand the features of the aircraft flow field at this critical time during the maneuver. Flight test data from DARPA are compared with SHAMAN results to demonstrate specific features of that method.

In Figure 11-48, the predicted vortex field is shown on the X-31 before and after departure. Because of the high angle of attack, the vortex field is moving away from the airplane at a high angle, but there are still significant interference effects of the vorticity on the vehicle. Note that the rudder is engulfed in part of the forebody vortex field just prior to departure. After departure, there is more asymmetry in the vortex fields because of the high angles of incidence and sideslip (shown in Figure 11-48), and most of the forebody and wing vorticity is above the rudder. As part of the diagnostic analysis of this maneuver, SHAMAN provides the time history of the loads on each component of the aircraft to help understand the changing loads as the flow field changes.

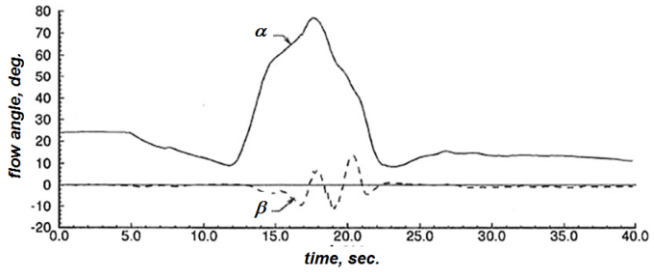

(a) Flow angles

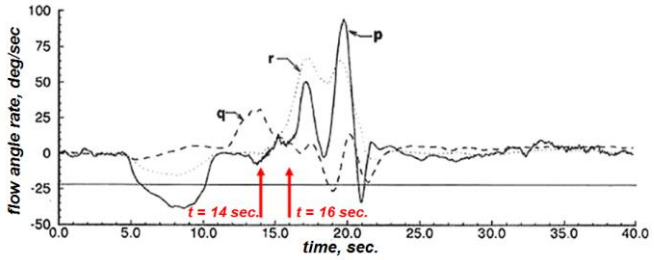

(b) Angular rates

Figure 11-46: Measured conditions, X-31 flight-test maneuver.

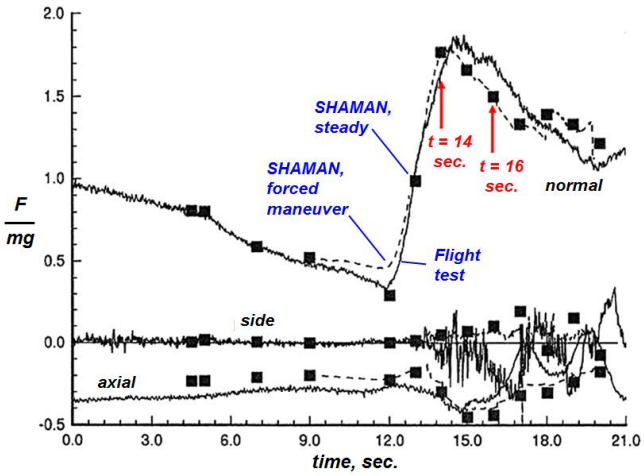

Figure 11-47: Measured and predicted forces, X-31 flight-test maneuver.

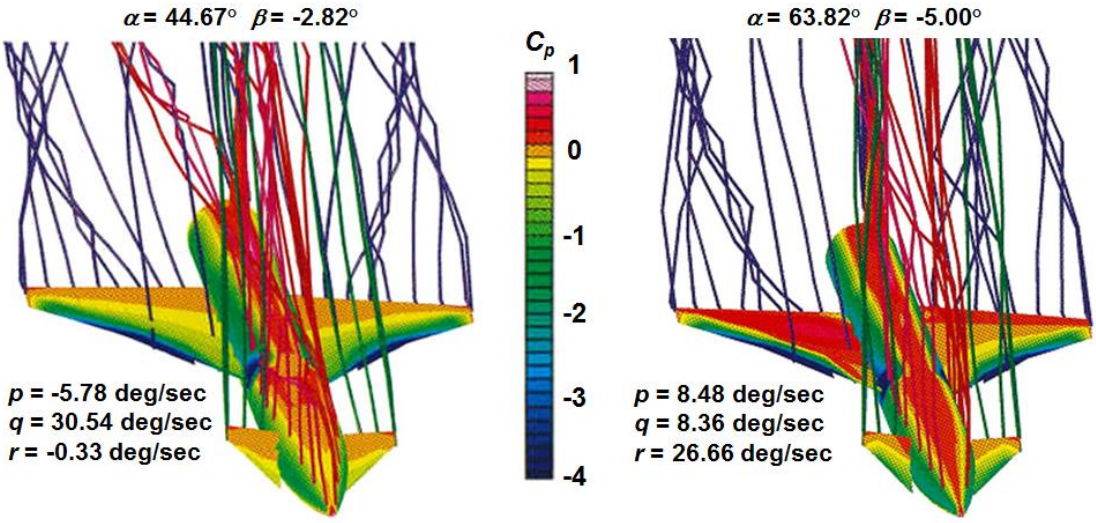

(a) t = 14 sec. **(b) t = 16 sec.**

Figure 11-48: Predicted vortex field for the X-31 in a departure maneuver.

4.5 High Lift, Multielement Wing: HLPW Trap Wing

So far, we have been looking at configurations with clean wings, but high-lift devices must be added for landing and takeoff to be realistic. Accurate computations of flows over high lift devices are a challenging task. At the leading edge of the slat, there are effects of compressibility, unsteady cove flow and presence of a laminar separation bubble. While on the main wing profile confluent boundary layer flow and adverse pressure gradient wakes are present. AIAA has recognized the importance of this aspect and already three cycles of the HLPW have been held. The test case for the first cycle was the NASA Trapezoidal wing.

4.5.1 Three-Element NASA Trapezoidal Wing

The full configuration test case features the 3-element NASA trapezoidal wing, more specifically the configuration 1 from the high-lift prediction workshop (slat at 30°, flap at 25°) with brackets (see Rumsey et al.[92]). At the trailing edge, the flap is partly or completely inside the wake region with elevated levels of turbulence intensity leading to the presence of bypass transition phenomena. Due to the fact that the fluid dynamics for the majority of these flow phenomena are dominated by viscous flow, RANS or higher fidelity CFD is required for realistic predictions.

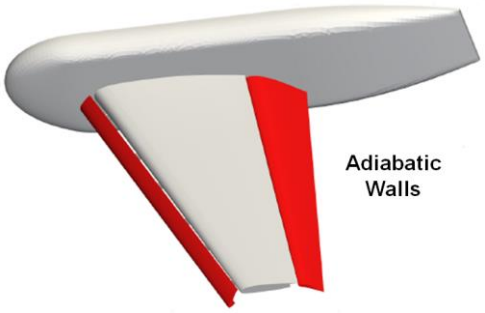

(a) CAD model

(b) Trap wing in 14-by-22-Ft. tunnel

Figure 11-49: The NASA trapezoidal wing.

Figure 11-49 shows the NASA Trapezoidal wing in the NASA Langley 14- by 22-Foot Subsonic Tunnel. It is a semispan model that used the tunnel floor as a symmetry plane. The freestream values correspond to the tunnel farfield upstream conditions at a Mach number of 0.2 and a mean-aerodynamic-chord Reynolds number of 4.2 million.

Transition modeling was known to be important in 2-D multielement airfoil studies, and it was noted at the workshop that transition effects could reduce trailing-edge flap separation and significantly improve pitching moment

predictions. Several contributors subsequently explored this effect, notably Eliasson et al.[93] used a database e^N method with the envelope approach to impose transition regions in conjunction with the SA model. All groups demonstrated improved results when transition regions were included.

Figure 11-50 shows integrated forces and pitch-up moment, comparing experiments with results computed by Tomac[94] (PhD) with the Edge code in transitional mode and in fully turbulent mode. Regarding lift and drag, the results computed by the γ-Re_θ SST transition/turbulence model of Langtry and Menter,[95] improvement is achieved in terms of not only absolute forces but also the angle of attack at which the wing stalls, Fig 11-50 (left and center). The prediction of a pitch-up moment is also improved for 13 to 28 degrees angle of attack.

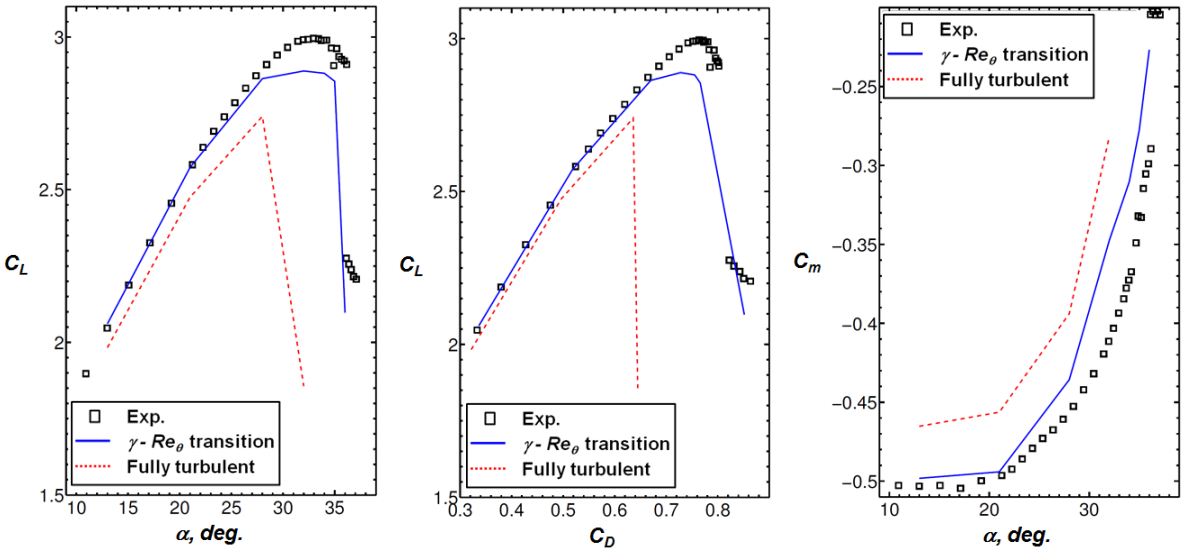

(a) Lift (b) Drag (c) Pitching moment

Figure 11-50: Integrated forces and moments computed with the Edge code (Tomac PhD thesis). $M = 0.2$, $Re_{mac} = 4.2 \times 10^6$.

The γ-Re_θ SST transition/turbulence model includes the solution of two additional transport equations for an intermittency parameter and a local transition onset momentum-thickness Reynolds number. The effective intermittency regulates the production of turbulent kinetic energy (TKE) in the SST model.

Figure 11-51 indicates the laminar and turbulent areas by viewing the projected intermittency levels (blue, red) on the surface and isosurface of elevated turbulent kinetic energy (yellow), for angle of attack of 28°. Note that the levels have been adjusted to clearly indicate the laminar and transitional regions. Blue areas are low levels of intermittency thus indicating laminar areas, red areas, on the other hand, indicate elevated levels of intermittency and transitional regions. The isosurface of turbulent kinetic energy has intentionally been removed from the upper surfaces on the left hand side in Figure 11-51 since the intermittency works as a good indicator for the relatively clean flow on the upper side of the wing. On the lower side, on the other hand, the flow is significantly more complex, and therefore, the yellow transparent isosurface is included as well. On the upper side, the results agree well with the computation by Eliasson et al.[93] that uses the database e^N method with the envelope approach in conjunction with the SA model to impose transition regions, indicated by a black line, this applies for all three elements.

On the lower side, the agreement is still good regarding the trailing edge flap except for the tripped boundary layer flow due to the wakes from the brackets. On the main profile, on the other hand, the results disagree significantly. While the e^N database method has predicted a transition location approximately midchord, the γ-Re_θ SST results show mainly turbulent flow on the main profile. However, this demonstrates the state of

the current transition model implementation in the Edge code. Overall, this case indicates that transition modeling is something that must become standard in the near future.

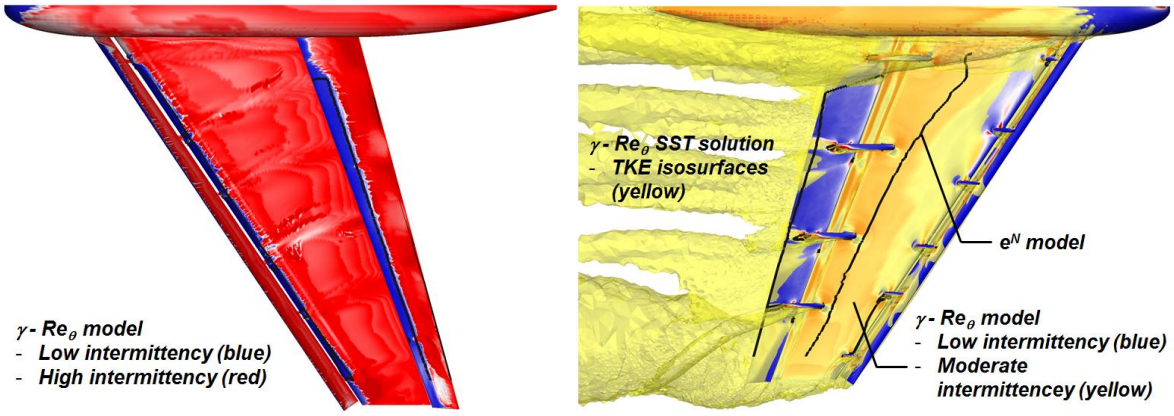

(a) Upper surface **(b) Lower surface**

Figure 11-51: Comparison of approximate prediction of transition locations. Trap wing, $M = 0.2$, $Re_{mac} = 4.2 \times 10^6$, $\alpha = 28°$.

4.6 Unsteady Aerodynamic Loads in Undercarriage Wake on A320

Significant dynamic loading in the vicinity of the landing gear (e.g., undercarriage housing walls, struts or landing gear doors) originate from fluctuating aerodynamic pressures that induce structural vibrations leading to fatigue. Figure 11-52 illustrates the physical problem of opening the doors and deploying the landing gear.

Sources of this dynamic behavior can be: motion of the doors/struts driving the flow, flow separating from the moving components themselves or vortices emanating from the landing gear that impinge on the other components. Furthermore, additional unsteadiness is introduced into the flowfield from the landing gear housing where an unsteady interaction between the main incident flow and the cavity flow occurs, mainly characterized by strong instabilities of the shear layers dividing the outer flow from the cavity flow. The time scales, however, of all these various dynamics can differ widely.

Dynamic loads generated by these unsteady flow phenomena often contribute to the design of structural parts in the undercarriage area, which raises two challenges. First, means are needed to mitigate the induced vibrations in order to increase the fatigue life of the parts and to reduce airframe noise. Second, efficient and accurate methods are needed to aid in determining the dynamic loads in order to perform a proper lightweight design of all structural parts.

(a) Main landing gear retraction

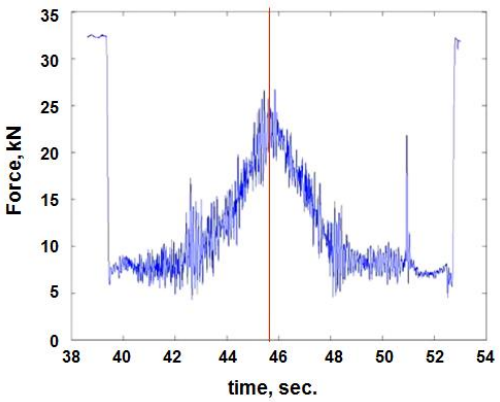

(b) Main landing gear door force

Figure 11-52: Landing gear retraction.

4.6.1 Physics Modeling Challenges: Two CFD Approaches

As part of a larger European Union research project known as AFloNext (AFLO), an extensive CFD team, Tomac et al.[96] performed unsteady CFD simulations in 2016 to better understand this complex physical phenomena occurring in the undercarriage area of an aircraft during takeoff and landing.

Their CFD studies focussed on three main effects considered as major contributors to the unsteady loads on the Main Landing Gear (MLG) door, namely the:

1. Unsteady wake trailing from the Nose Landing Gear (NLG)
2. Unsteady vortices shedding from the MLG door situated in the NLG wake
3. Acoustic resonance of the MLG cavity

Such a computation is a demanding problem in terms of grid generation and local grid refinement to maintain the resolution of the NLG wake over the 13 meters until it hits the door and other components of the MLG. Component motion adds further demands for time resolving the disparate time scales of the complete nonstationary problem.

Those are challenges for numerical representation, but there are also challenges to the physical modeling. The NLG is a very bluff body, and the physical modeling must capture the essential features in a bluff-body wake where the turbulence is no longer wall-bounded. The AFLO Project embraced multiple high-fidelity CFD simulation approaches for modeling these complex flows, adopting to freeze in time the component motion of doors/gear to two “stationary snapshots”: partly deployed and fully deployed. Then, two CFD approaches were adopted by the team[96] for their studies of unsteady flow around the stationary components.

The first was hybrid RANS/LES modeling. In order for this model to succeed, the mesh downstream of the NLG must resolve, and not unduly dissipate, the unsteady wake sufficiently well at least up to and including the MLG, the cavity and the door. A RANS subteam addressed this issue by refining the grid within a spatial box enclosing all of the undercarriage so that specific grid enrichment could provide the resolution that is called for. Note that this grid has to be refined in all three spatial dimensions, in contrast to just the normal direction for wall-bounded turbulence.

In the second approach, a separate subteam chose to solve the discrete Lattice-Boltzmann equations. These are mesoscopic equations for fictive sets of particles that are modeled through their distribution function. Macroscopic properties, such as pressure, are then determined through post processing. The Lattice-Boltzmann Method (LBM) has not been addressed in this article, and just a few additional details follow.

Due to its particulate nature and local dynamics, the LBM has several advantages over other conventional CFD methods, especially in dealing with complex boundaries and treating microscopic interactions since the method originates from a molecular-like description of a fluid and can directly incorporate physical terms stemming from knowledge of the interaction between molecules. Turbulence is handled according to the LES approach, either with high-order explicit filtering or with a dedicated subgrid scale model. In particular, the LBM approach is weakly dispersive and almost nondissipative since its processes are streaming and colliding.

Some hybrid RANS/LES results have been selected for this article, and the reader is referred to Tomac et al.[96] for the additional results including the LBM simulations.

4.6.2 Geometry Models and Grids

Figure 11-53 displays the grid and its adaption in the refinement box for the undercarriage region. The grid-enrichment boxes extended from NLG to two meters downstream of MLG and had a maximun cell size of 0.02 meters applied to both surface and volume grid. The maximum cell size in the density region between nose landing gear and main landing gear doors was 0.02 meters and the surface resolution on various critical appendages had a maximum edge length of 0.01 meters. Despite this very fine lower-surface grid, the overall grid consisted of only 150 M cells.

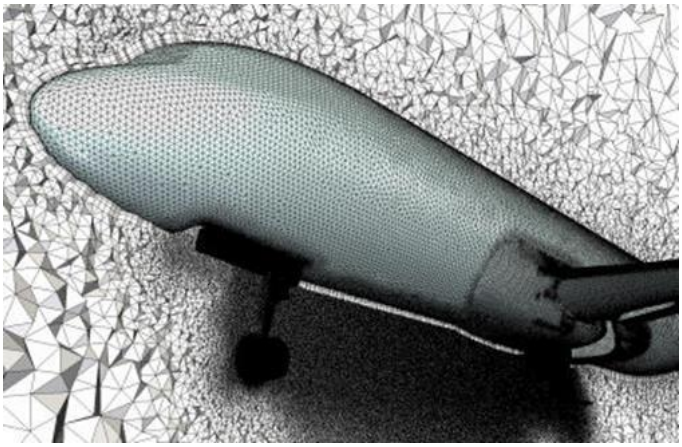

Figure 11-53: Undercarriage grid refinement.

4.6.3 Results: Hybrid RANS/LES Modeling

The general mean flow features have been highlighted with an emphasis on the vortex structures in the wake created by the NLG and its possible effects when striking the MLG and door and cavity.

4.6.3.1 Landing Case: high speed, low α, NLG & MLG fully deployed

Figure 11-54 presents hybrid RANS/LES results computed for the landing case with the NLG and MLG fully deployed. These are from the first 10000 time accurate iterations (1 second) started from a RANS solution.

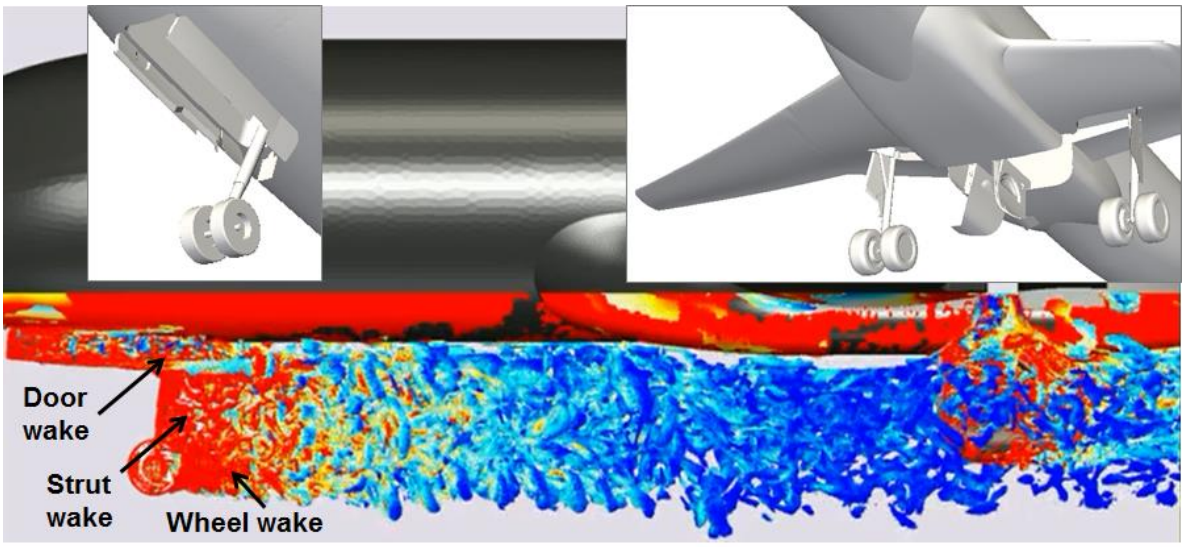

Figure 11-54: Unsteady vortical flow in the undercarriage area computed with hybrid RANS/LES for Landing Case 1b; illustrated by contours of *Q* criterion.

The summary conclusions that can be drawn from Figure 11-54, as well as from videos of time-evolving flow quantities, such as C_p and Q criterion, are the following:

1. Large areas of separated flow are apparent on the MLG door
2. There are three components to NLG wake: a door wake, a strut wake, and a wheel wake

3. Small structures around the NLG are not resolved all the way down to MLG door. However, these structures are judged not to play an important role in the door vibration because they are small
4. Vortex shedding from the NLG and NLG rod is resolved sufficiently all the way downstream to the MLG door
5. Vortex tubes rolling off, and onto, the edges of the cavity are well resolved. Small structures are captured in the close proximity of MLG door
6. C_p and Q criterion time evolution movies indicate the following:
   - Pressure fluctuations on the MLG door are indeed affected by BOTH cavity and wake flows
   - On the inner side of the MLG door, the pressure pulses are slower with frequency similar to cavity flow fluctuations

Comparison of power spectral densities between the hybrid RANS/LES simulation and flight-test data indicated that the energy levels on the inner door surface were quite well predicted, but the cavity resonance seemed too intense compared to the flight-test data. The results also showed that the nose landing gear wake impacting on the main landing gear doors seemed to be the most important source of excitation.

4.6.3.2 Cavity investigation

Figure 11-55 shows the standard deviation of the oscillating pressure field, p_{rms} in two different longitudinal planes, cutting through the MLG cavity. Inside of the cavity, the fluctuations increase when approaching the rear wall of the cavity. Literature studies tell us that the impingement of the separated boundary layer on the rear wall of the cavity is the cause of a feedback loop between the boundary layer separation on the cavity leading edge and the pressure waves traveling upstream from the impingement on the rear wall.

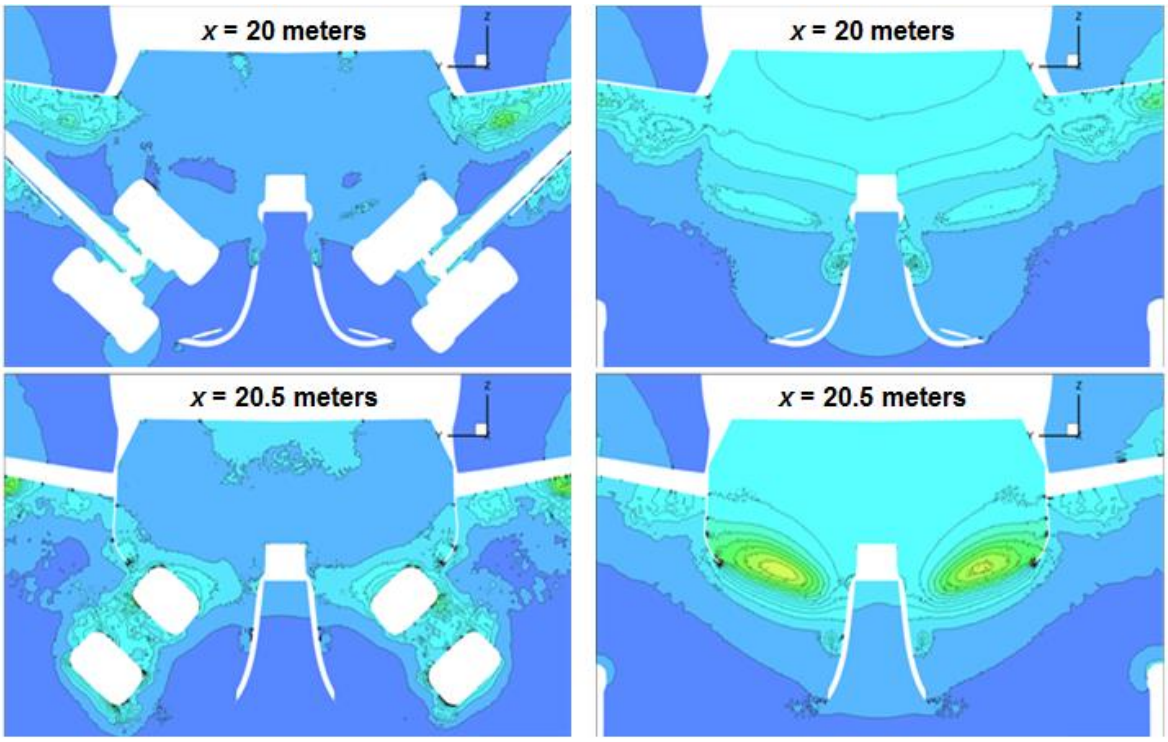

(a) Main landing gear partly deployed **(b) Main landing gear fully deployed**

Figure 11-55: Standard deviation of the oscillating pressure field in two different longitudinal planes. Takeoff conditions, $M = 0.272$, $q_\infty = 5247$ *Pa*, $\alpha = 10.5°$.

Figure 11-56 illustrates this mechanism, and it is known to be the cause for the above mentioned cavity tones. In this figure, M_1 represents the onset Mach number to the cavity, and the cavity flow physics are characterized in terms of the cavity length-to-depth ratio, *l/h*. Some examples of steady flow characteristics have been given by Plentovich et al.[97] and for unsteady flow characteristics by Tracy et al.[98] These cavity flows present another challenge for CFD to accurately resolve the unsteady cavity flow physics in the context of a complete aircraft simulation (e.g., Figure 11-54), and to do so with sufficient fidelity to extract unsteady loads for neighboring components. Although presented in this instance for a landing gear application, the cavity flow fields are also highly important for internal store release from combat aircraft. Some examples at supersonic speeds have been given by Stallings and Forrest[99] and Stallings and Wilcox[100] and at subsonic and transonic speeds by Stallings et al.[101]

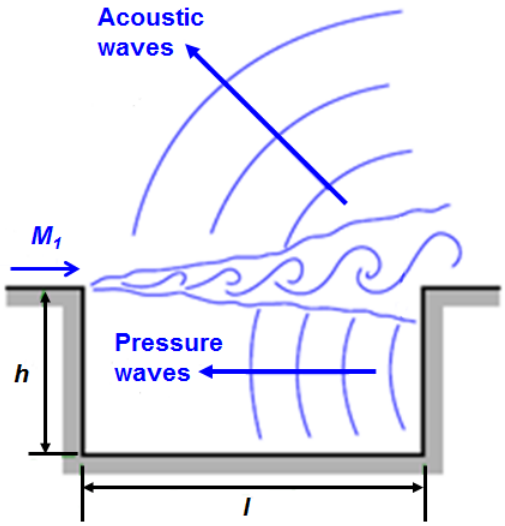

Figure 11-56: Schematic illustration of the feedback process for resonant wave effects in a cavity from a separated shear layer.

5.0 FUTURE PROSPECTS

While RANS technology has become fairly well established for select separated flow simulations (such as from a sharp-edged slender delta wing), many contemporary separated flow simulation interests seem to require at least a hybrid RANS/LES class of technology. However, the pace of hybrid RANS/LES technology maturation has been inhibited by insufficient supercomputer evolution to support this class of computation.

The discussion of future prospects is organized to first address trends of supercomputer growth (i.e., the context of these simulations). Next, the future growth of simulation needs is addressed, and finally some recommendations for future developments will be offered.

5.1 Future Growth of Computer Processing

For much of the history of CFD, the growth of supercomputer capacity, both as regards speed and memory, has kept pace with the advancements of flow simulation technology. This was characterized by the linear portion of the s-curve shown in Figure 3.0.1, spanning the evolution of nonlinear potential, Euler, and Reynolds-Averaged Navier-Stokes solvers. Moore's law has been useful to estimate how much improvement in processing time can be anticipated from supercomputer evolution, and Figure 11-57 from Luckring[102] shows the established trend of 1.9/year. (At this rate, computing becomes approximately 1000 times faster per decade.) Despite this sustained growth of the fastest supercomputers, the supercomputer speed has not been sufficient to support the evolution of CFD into hybrid RANS/LES technology, and these methods have remained very expensive to use for the last two decades.

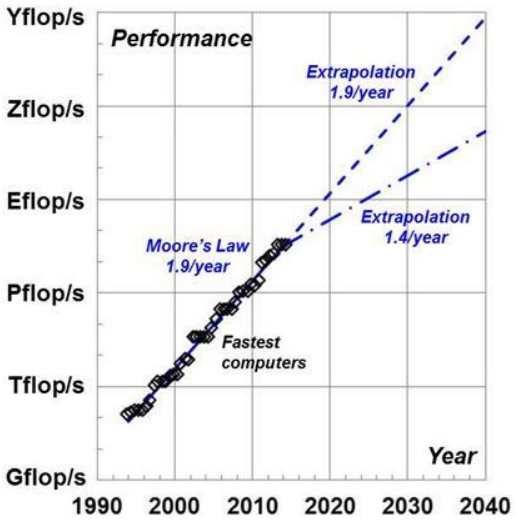

Figure 11-57: Projected computer performance, Moore's law.

Cluster supercomputing has matured over three decades,

and Spalart and Venkatakrishnan[103] have pointed out that Moore's law extrapolations may now overestimate future supercomputer performance due to fundamental chip limitations. They estimate that anticipated growth may only be at roughly half the Moore's law rate, with possibly even less speedup realized for typical CFD applications. Both of these extrapolations are shown in Figure 11-57. By either scenario, CFD simulations of moderately to massively separated flows will remain expensive to accomplish for some time with current computer technology and solution algorithms.

5.2 Future Growth for Simulation Needs

Although not a topic of this paper, it is the authors' observation that many useful applications of RANS-based solvers are underway to address attached flow interests. One recent summary of RANS method capabilities has been given by Bush et al.[104] With regard to separated flow interests, it appears that at least hybrid RANS/LES technology is necessary for the massively separated flows, and may be needed for moderately separated flows. It should be recalled that massively separated flows occur not only at aircraft but also at component scales (e.g., the wake behind a nose gear). There will be a sustained need for increased efficiency of these simulations as well as for improved concepts for resolving small-scale turbulence in the context of larger-scale separation. As a compounding factor, flows need to be simulated about complex full-scale configurations, at full-scale conditions, and an example of this challenge follows.

Current CFD simulations of complex configurations can use 500 million points without fully modeling the full-scale vehicle of interest. This problem size occurs from the need to resolve geometric features as well as the flows they create. Larger cases are not unprecedented, and in one recent example[105] at NASA, approximately 4 billion cells were needed to model a complex Space Launch System configuration with complex vortical flows, Figure 11-58. The full-scale configuration geometry had already been significantly simplified, roughly to that of a wind-tunnel model, and adaptive grids were used to help resolve the vortex flows with some efficiency. The flow simulation in Figure 11-58 shows vortical separation from the tower that interacts with the vehicle at takeoff conditions.

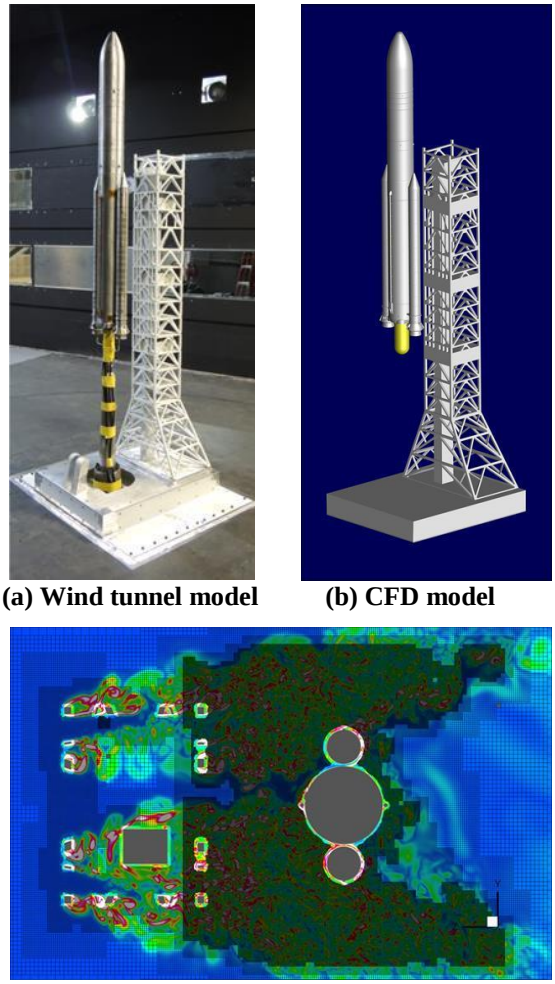

(a) Wind tunnel model **(b) CFD model**

(c) Flow simulation

Figure 11-58: NASA SLS example, 4 billion cells. Krist et al.[105]

For this problem size, solutions took 2-3 weeks to accumulate 8-9 days of processing time in a shared-resource supercomputing environment. With regard to full-scale configuration aerodynamics, it is estimated[106] that roughly an order of magnitude increase in grids could be anticipated for representing full-scale geometry along with a doubling in the cycles required for convergence with this grid at full-scale Reynolds numbers. A factor of 20 speed up would be required to solve this full-scale simulation using the same 9 days of processing time (all other factors being held constant). Following Moore's law (full or half rate), this would take 5 to 10 years to realize.

It is not uncommon in a program development environment for urgent needs to arise that demand short turnaround. Another speedup factor of 400

would be needed to change the 9 days to 30 minutes of processing time to enable same-day analysis capability in support of such critical program needs. Following Moore's law again, this would take 9 to 18 years to realize for the wind-tunnel problem size. For 30-minute processing time of the full-scale problem, the combined factor of 8000 would take approximately 14 to 28 years to realize through supercomputer evolution alone.

All of these projections are for a frozen level of physics simulation (in this example, hybrid RANS/LES) and for a frozen set of physics representation (e.g., no exhaust plumes are included). It has been the authors' experience that similar grid requirements occur for other vehicle classes at full-scale conditions; one set of geometric and flow complexities get traded off for another across vehicle classes, still resulting in these very large problem sizes. Conventional computer advancements alone will not be sufficient for CFD to penetrate flight envelope regions with separated flows and contribute timely results of grid-resolved flows for full-scale vehicle simulations. There is a sustained need for advanced algorithm development, both as regards speed as well as flow physics resolution (e.g., adaptive grids) and representation (e.g., transitional flows). Guidance from new experimentation could contribute to the new flow physics representations.

5.3 Legacy and Path Forward

In this section we will summarize the CFD legacy with a perspective toward CFD simulation categories that have become successful as well as those that have been less than successful. For both categories, discussion of some underlying reasons is included along with recommendations for future activity to advance CFD capability to simulate separated flows that are relevant to military aircraft needs.

The question of which applications, and which associated flow physics, CFD technology has become well accepted (as well as and which applications/physics the CFD technology has not matured) is best addressed in the context of military aircraft operations (Figure 11-1) and associated separated flow physics (Figure 11-2). Although this paper focuses on separated flows, some discussion of attached flows is included.

5.3.1 Legacy

5.3.1.1 What Works and Why

Large AR wings. For the straight-wing and swept-wing categories, the optimum operating conditions are attached flow over the wing, and here RANS technology has become useful for predicting lift and approximating drag, even at higher lift levels than cruise flight. For incipient separation, one could compare and contrast the two different technologies, RANS vs. Euler + boundary layer. The former is well-posed mathematically for separated flow, whereas the latter breaks down at separation unless special efforts are taken. RANS of course needs a sufficiently refined "boundary-layer type" grid, i.e., highly refined in the direction normal to the wall, and not in the other two directions. Overall, we could say that RANS works as well as boundary-layer theory up to separation, but with the advantage of improved representation of viscous flows about complex configurations. Predictions for the onset of separation could be very useful, and assessments of RANS capabilities for such predictions are recommended. New experiments would be desired to obtain detailed data, including the onset of unsteady flow characteristics, to guide these assessments for conditions relevant to military aerodynamics.

Moderate and small AR wings. RANS also produces reasonably reliable solutions when flow separates from an aerodynamically sharp leading edge of a slender-wing displayed in Figure 11-2, and forms a coherent vortex over the wing. Such separation is indeed massive but not necessarily pervasive, even though the shear layer (which is turbulent) rolls up to form the vortex. The structure of the vortex however remains coherent, spatial scales are large and time fluctuations small enough to enable effective RANS simulations.

Many impressive results using a variety of hybrid RANS/LES formulations have been accumulated over roughly 20 years. Highlights in this paper have included unsteady vortex flows, unsteady post-stall maneuver flows, and unsteady transonic shock/boundary-layer flows; others are available in the literature. Applications

have ranged from delta wings to aircraft configurations. The accomplishments are also noteworthy in that supercomputer resources have not kept up with the simulation needs of these methods in contrast to the prior history of CFD development. (See, Figure 11-9).

5.3.1.2 What doesn't work and Why

Large AR wings. Considering first attached flow cruise conditions, accurate CFD predictions of cruise drag continues to be challenging. Seven cycles of the Drag Prediction Workshops have reduced computational variations, but the residual variations remain large compared to experimental accuracy. An additional source of the computational variations was found to be a separation pocket at the upper surface wing-body juncture near the trailing edge. RANS simulations varied greatly in predictions of this mild and localized separation, and a new experimental campaign has been initiated to study this class of separation in detail following CFD validation testing principles.

There are other sources of mild and localized separation, and as this separation grows, for example with increasing angle of attack or flight speed, the separation becomes massive and can also shift from localized to pervasive scales. It may be possible to obtain a RANS solution in these circumstances, but its trustworthiness must be questioned. The physics of this separation is better represented with hybrid RANS/LES methods, but validation data to guide development of best practices for these methods is lacking for many practical applications. The High-Lift Prediction workshops represent one effort to address these needs for high-lift configurations that are relevant to transport aerodynamics.

Moderate and low AR wings. As the operating conditions become more extreme for both moderate and low aspect ratio wings, the mild separation becomes both massive, i.e., unsteady flow with large fluctuations, as well as pervasive. This type of unsteady flow is fundamentally different from the assumptions upon which the boundary-layer equations are derived. The Navier-Stokes equations of course are still valid, but an accurate solution now requires a time accurate integration with a time step suitable to capture the relevant fluctuating phenomena and a grid size refined not in just the wall-normal direction but in all directions throughout the entire pervasive separated flow region. In addition, the turbulence modeling must now treat isotropic turbulence and not wall-bounded turbulence. Such highly resolved temporal and spatial simulations are very uncommon in current CFD applications, although promising approximations from hybrid RANS/LES methods have been maturing for several decades. This particular maturation has been inhibited by a lack of computer speed advancements to keep up with the simulation requirements of hybrid RANS/LES techniques (as depicted in Figure 11-9).

Vortices present a number of contemporary challenges for CFD simulation. Practical wings have blunt leading edges, and one challenge is the formation or onset of the blunt-leading-edge vortex. A sharp-edged wing geometrically fixes the separation location to the leading edge, and all of the above requirements for RANS to work are fulfilled. However, when the wing surface is smooth, the location where the turbulent shear layer leaves the surface becomes a balance of the inertial and viscous forces in the Navier-Stokes equations that can be sensitive to the turbulence modeling used. Recent progress from the STO AVT-113 and AVT-183 projects have shown that good predictions of the blunt-leading-edge vortex flows can be achieved if the leading-edge vortex incipient separation (i.e., the origin of the vortex) is matched between experiment and CFD, but that the onset and progression of this incipient separation was not consistently predicted. The origin of the leading-edge vortex affects the vortex strength and location over the wing, and new studies will be needed to improve predictions of incipient vortex separation.

Vortex breakdown presents another contemporary challenge. Simulation requirements change if the vortex bursts over the wing because then the time and space scales grow, the flow fluctuates, and the separation becomes massive. Contributions to vortex breakdown understanding were achieved experimentally and numerically through the STO project AVT-080. Although hybrid RANS/LES technology has improved these predictions, accurate predictions have yet to be demonstrated. Vortex breakdown can be one source of

adverse buffet and pitchup characteristics, and new experiments to quantify the unsteady flow details within burst vortices for a systematic variation of leading-edge vortex properties could be useful for improving the CFD simulation capability.

Practical wing geometries also incorporate moderate leading-edge sweep angles and wing aspect ratios (e.g., F-22), and this causes the leading-edge vortices to be much more unsteady than those from slender wings. Bursting occurs at lower angles of attack, and the applicability of RANS to capture these unsteady and massively separated vortical flows is questionable. Here again hybrid RANS/LES methods may be required, but best practices to guide the shift from RANS to hybrid RANS/LES simulations have not generally been established. Here again, new and systematic validation campaigns, for example as wing aspect ratio is increased from slender to moderate conditions, that emphasize unsteady vortical content could contribute to this need.

There have been to date only limited exploration studies of these issues, for example in the AVT-161 and CAWAPI-3 programs. The latter treated one of the so-called outlier cases, *FC-25*, with massive and pervasive burst vortex flow over the moderately-swept outer wing panel of the F-16XL using time-accurate hybrid RANS/LES technology that showed some improvement in comparison with flight-test data, but more controlled computations are needed to further our understanding. The focus of study in AVT-161, the X-31 aircraft, has in its flight envelope, all of the categories of separation in our categorization, however, aside from coherent vortex separation, most of these were not explored in any concerted effort. But the motivating goal of course would be to achieve virtual flight testing via CFD.

5.3.2 Path Forward

It appears likely to these authors that the three decades of experience with RANS simulations of separated flows may have established a condition of diminishing returns as regards new capability, and that many of the present CFD simulation challenges for separated flows will require at least hybrid RANS/LES technology. A variety of flight-test programs (F-18 HARV, X-31, F-16XL) in conjunction with a suite of ground-based projects, coordinated through the STO, has established a number of separated flow challenges for contemporary CFD technology. Collectively, this has indicated a need for new campaigns, with integrated CFD and experiment that follow validation testing principles, to obtain new data capable of validating hybrid RANS/LES methods for unsteady separated flow simulations relevant to military aircraft interests. It must also be recognized that additional simulation needs may be important that are not represented in the above mentioned activities.

The authors recommend that a panel be established to help prioritize projects to improve CFD simulation capability of separated flows relevant to military aircraft. Several needs related to commercial transport aircraft are being addressed through current workshop activities (e.g., High Lift Prediction Workshop), and new work could either seek to influence these established workshops or create new projects likely to be coordinated through the STO.

More collaborative campaigns and concerted efforts will be needed, broken down into reduced complexity and even unit problems, to study the broader operating regimes of incoherent, massive and pervasive separation. Guidance for the interrelatedness of systems-level needs (e.g., configuration aerodynamics) and the more fundamental research (e.g., unit or combined-unit poroblems) could be drawn from the current STO project AVT-297 which is establishing frameworks for validation assessment. The modeling focus would be hybrid RANS/LES and further understanding is needed on how to adequately resolve the relevant fluctuating turbulent phenomena in time and space. The turbulent separated flow is massive so appropriate gridding for the LES methodology becomes a critical issue. Such understanding can only come from systematic studies of all the factors involved for the accurate simulation of massive separated turbulent flow.

6.0 CONCLUDING REMARKS

This paper has provided a snapshot of CFD capabilities for predicting separated flows that are relevant to military aircraft operations. The scope of this paper is by no means comprehensive, and the content has been informed by, but not limited to, the organizing principles of the sponsoring symposium.

Separated flows often establish the useable portion of an aircraft flight envelope. In many cases, this takes the form of restrictions associated with separated flow effects on vehicle performance characteristics such as maximum lift coefficient, pitchup, and buffet onset. In other cases, this takes the form of performance enhancements such as maneuver lift and stability from separation-induced leading-edge vortex flows. Separated flows have also inhibited the penetration of CFD to the broader portions of an aircraft flight envelope, both due to flow physics complications associated with the separated flows and due to numerical resource requirements to accurately simulate these flow physics.

The approach taken for this paper was to first summarize the scope of separated flow challenges for military aircraft along with some of the fundamental flow physics associated with these separated flows. Next, a seven-decade summary was presented for the evolution of CFD methods with a focus on separated flow simulation capability. Select examples for advances to the separated flow simulation capability that range from simple delta wings to full aircraft configurations were included in this summary. Six case studies, in an order of increasing flow complexity, were also discussed to document in more detail separated flow simulation capabilities. They provide a broad overview of those operating conditions where CFD makes reasonably reliable predictions and those where they are less reliable, and even untrustworthy. The case studies addressed:

1. steady, controlled and ordered vortex separation from smooth surfaces of slender wings in steady flight;
2. unsteady breakdown of such vortices caused by higher incidence in subsonic flow, or by shock wave interaction at transonic speeds;
3. unsteady separation from a hybrid wing, such as the F-18, caused by shock-boundary-layer interaction (SBLI) leading to abrupt wing stall;
4. maneuvering flight where the accelerating motion of the aircraft causes unsteady smooth-surface separation of vortices and their accompanying time-dependent motion in the flowfield; and finally,
5. maximum lift and stall separation on a multielement wing;
6. unsteady component loads from an open landing gear cavity.

Finally, future prospects for advances to separated flow simulation capability was reviewed. Many successes have been accomplished with RANS technologies over the last 30 years, and most of the remaining separated flow simulation challenges appear to need at least hybrid RANS/LES approaches to capture unsteady content of these flows. Applications of hybrid RANS/LES methods have also demonstrated many promising results for configurations ranging from simple delta wings to complex aircraft geometries. Unfortunately, these methods have remained resource intensive now for several decades, and computer evolution alone does not presently indicate much improvement for these circumstances. Faster algorithms, with efficient adaptive grid technology, will continue to be needed. Collaborative campaigns that focus on obtaining CFD validation data for unsteady separated flows are also highly desirable.

7.0 ACKNOWLEDGMENTS

The first author has drawn on the research carried out by a number of his doctoral students at KTH over the years. They have participated in most of the AVT Task Groups discussed in the paper, and their work has benefited greatly from this experience. We highly appreciate this opportunity that STO made available to us.

The second author greatly appreciates the support at the NASA Langley Research Center from the Research Directorate Office for the research that led to this article. Both authors also wish to thank Ms. Dorothy Notarnicola at the NASA Langley Technical Library for sustained literature research support.

8.0 REFERENCES

[1] AGARD, "Flow Separation", AGARD-CP-168, 1975.

[2] Hirschel, E. H., Rizzi, A., Breitsamter, C., and Staudacher, W. : *Separated and Vortical Flow in Aircraft Wing Aerodynamics*, in publication by Springer, Berlin, 2020.

[3] Hirschel, E. H., Cousteix, J., Kordulla, W., "Three-Dimensional Attached Viscous Flow," *Springer, Berlin Heidelberg*, 2014.

[4] Hall, R. M., Woodson, S. H., and Chambers, J.R., "Accomplishments of the Abrupt-Wing-Stall Program," *AIAA Journal of Aircraft*, Vol. 42, No. 3, 2005, pp 653-660.

[5] Polhamus, E. C., "A Survey of Reynolds Number and Wing Geometry Effects on Lift Characteristics in the Low Speed Stall Region," NASA CR-4745, 1996.

[6] Babinsky, H., and Harvey, J. K., (Eds), "*Shock Wave-Boundary-Layer Interactions*," Cambridge University Press, 2011.

[7] Vos, R., and Farokhi, F., "*Introduction to Transonic Aerodynamics*," Springer Dordrecht, 2015.

[8] von Neumann, J.; Richtmyer, R. D.: A Method for the Numerical Calculation of Hydrodynamic Shocks, *Journal of Applied Physics*, Vol. 21, Issue 3, p.232-237, 1950.

[9] Murman, E. N., and Cole, J. D., "Calculation of Plane Steady Transonic Flows," *AIAA Journal*, Vol. 9, No. 1, 1971. Also AIAA Paper 70-188, 1970.

[10] Jameson, A., Schmidt, W. and Turkel, E., "Numerical Solutions to the Euler Equations by Finite Volume Methods Using Runge-Kutta Time-Stepping Schemes," AIAA Paper 81-1259, 1981.

[11] Rizzi, A. and Engquist, B., "Selected Topics in the Theory and Practice of Computational Fluid Dynamics," *J. Comp. Phys.*, Vol 72, 1987, pp. 1-69.

[12] Vos, J., B., Rizzi, A., Darracq, D., and Hirschel, E. H., "Navier–Stokes solvers in European aircraft design," *Progress in Aerospace Sciences*, Vol 38, No. 8, 2002, pp. 601-697.

[13] Spalart, P. R., Jou, W-H., Strelets, M., and Allmaras, S. R., "Comments on the Feasibility of LES for Wings, and on a Hybrid RANS/LES Approach," *Advances in DNS/LES, 1st AFOSR Int. Conf. on DNS/LES*, Aug 1997, Grey den Press, Columbus OH.

[14] Whitcomb, R. T., and Clark, L. R., "An Airfoil Shape for Efficient Flight at Supercritical Mach Numbers," NASA TM X-1109, 1965.

[15] Whitcomb, R.T., and Blackwell, J. A., Jr., "Status of Research on a Supercritical Wing," NASA SP-124, 1966.

[16] Loving, D. L., "Wind-Tunnel-Flight Correlation of Shock-Induced Separated Flow," NASA TN D-3580, 1966.

[17] Blackwell, J. A., Jr., "Preliminary Study of Effects of Reynolds Number and Boundary-Layer

Transition Location on Shock-Induced Separation," NASA TN D-5003, 1969.

[18] Hirschel, E. H., and Krause, E., *eds*., "40 Years of Numerical Fluid Mechanics and Aerodynamics in Retrospect," *Notes on Numerical Fluid Mechanics and Multidisciplinary Design (NNFM)*, Vol. 100, Springer Berlin Heidelberg, 2009.

[19] Bailey, F. R.; and Ballhaus, W. F., "Comparisons of Computed and Experimental Pressures for Transonic Flows About Isolated Wings and Wing- Fuselage Configurations," NASA SP-347, 1975, pp. 1213-1231.

[20] Boppe, C. W., "Computational Transonic Flow about Realistic Aircraft Configurations," AIAA Paper 78-104, 1978.

[21] Boppe, C. W., "Computational Transonic Flow about Realistic Aircraft Configurations," AIAA Paper 80-130, 1980.

[22] Jameson, A., Caughey, D. A., Newman, P., A., Davis, R. M., "A Brief Description of the Jameson-Caughey NYU Transonic Swept-Wing Computer Program – FLO 22," NASA TM X-73996, 1976.

[23] Jameson A. and Caughey D., "A Finite Volume Method for Transonic Potential Flow Calculations," AIAA Paper 77-635, 1977.

[24] McLean, J. D., and Randall, J. L., "Computer Program to Calculate Three-Dimensional Boundary Layer Flows over Wings with Wall Mass Transfer," NASA CR-3123, 1978.

[25] Mendenhall, M. R. and Lesieutre, D. J., "Prediction of Vortex Shedding From Circular and Noncircular Bodies in Subsonic Flow," NASA CR-4037, January 1987.

[26] Mendenhall, M. R. and Lesieutre, D. J., "Prediction of Subsonic Vortex Shedding From Forebodies With Chines," NASA CR-4323, September 1990.

[27] Nielsen Engineering and Research, Inc., http://www.nearinc.com/, 2019.

[28] Brune, G. W.; Weber, J. A.; Johnson, F. T.; Lu, P.: and Rubbert, P. E., "A Three-Dimensional Solution of Flows Over Wings with Leading-Edge Vortex Separation," NASA CR-132709, 1975.

[29] Gloss, B. B., and Johnson, F. T., "Development of an Aerodynamic Theory Capable of Predicting Surface Loads on Slender Wings with Vortex Flow," Proceedings of the SCAR Conference, NASA CP-001, 1976.

[30] Luckring, J. M., "Recent Progress in Computational Vortex Flow Aerodynamics," AGARD CP-494, Paper No. 6, July 1991.

[31] Rizzi, A., "Euler Solutions of Transonic Vortex Flows Around the Dillner Wing," *AIAA Journal of Aircraft*, Vol.22, No. 4, 1985. Also AIAA Paper 84-2142, 1984.

[32] Raj, P., and Brennan, J. E., "Improvements to an Euler Aerodynamic Method for Transonic Flow Analysis," *AIAA Journal of Aircraft*, Vol. 26, No.1, 1989. Also AIAA Paper 87-0040, 1987.

[33] Raj, P., and Singer, S.W., "Computational Aerodynamics in Aircraft Design: Challenges and Opportunities for Euler/Navier-Stokes Methods," *SAE Transactions*, Vol. 100, Section 1: JOURNAL OF AEROSPACE, Part 2, 1991, pp 2069-2081. Also iPAC911990, International Pacific Air & Space Technology Conference, Gifu, Japan, 1991.

[34] Roe, P. L., "The use of the Riemann problem in finite difference schemes," Seventh International Conference on Numerical Methods in Fluid Dynamics. Lecture Notes in Physics, Vol. 141, Springer, Berlin, Heidelberg, 1981, pp. 354-359.

[35] Van Leer, B., "Flux-Vector Splitting for the Euler Equations," ICASE Report No. 82-30, 1982. Also Lecture Notes in physics, Vol. 170, 1982, pp. 507-512.

[36] Thomas, J. L., and Walters, R. W., "Upwind Relaxation Algorithms for the Navier-Stokes Equations," AIAA Paper 85-1501 CP, 1985.

[37] Thomas, J. L., van Leer, B., and Walters, R. W., "Implicit Flux-Split Schemes for the Euler Equations," AIAA Paper 85-1680, 1985.

[38] Thomas, J. L., and Newsome, R. W., "Navier-Stokes Computations of Lee-Side Flows over Delta Wings," AIAA Paper 86-1049, 1986.

[39] Thomas, J. L., Taylor, S. L., and Anderson, W. K., "Navier-Stokes Computations of Vortical Flows Over Low Aspect Ratio Wings," AIAA Paper 87-0207, 1987.

[40] Hummel, D., "On the Vortex Formation Over a Slender Wing at Large Incidence," AGARD CP-247, Paper 15, 1979.

[41] Cart3D, https://www.nas.nasa.gov/publications/software/docs/cart3d/, last updated 2018.

[42] Ghaffari, F. G., Luckring, J. M., Thomas, J. L., Bates, B. L., and Biedron, R. T., "Multiblock Navier-Stokes Solutions About the F/A-18 Wing-LEX-Fuselage Configuration," *AIAA Journal of Aircraft*, Vol. 30 No. 3, 1993. Also AIAA Paper 91-3291-CP, 1991.

[43] Benek, J. A., Steger, J. L., and Dougherty, F. C., "A Flexible Grid Embedding Technique with Application to the Euler Equations," AIAA Paper 83-1944, July 1983.

[44] Benek, J. A., Buning, P. G., and Steger, J. L., "A 3-D Chimera Grid Embedding Technique," AIAA Paper 85-1523-CP, 7th Computational Physics Conference, Cincinnati, Ohio, 15-17 July 1985.

[45] Buning, P. G, Chiu, I. T., Obayashi, S., Rizk Y. M., and Steger, J. L., "Numerical Simulation of the Integrated Space Shuttle Vehicle in Ascent," AIAA Paper 88-4359-CP, 1988.

[46] OVERFLOW, https://overflow.larc.nasa.gov/, last updated 2019.

[47] Pirzadeh, S. Z., "Structured Background Grids for Generation of Unstructured Grids by Advancing-Front Method," *AIAA Journal of Aircraft*, Vol. 31, No. 2, 1993, pp. 257-265. Also AIAA Paper 91-3233, 1991.

[48] Pirzadeh, S. Z., "Unstructured Viscous Grid Generation by the Advancing-Layers Method," *AIAA Journal of Aircraft*, Vol. 32, No. 8, 1993, pp. 1735-1737. Also AIAA Paper 93-3453, 1993.

[49] Pirzadeh, S. Z., "Three-Dimensional Unstructured Viscous Grids by the Advancing-Layers Method," *AIAA Journal of Aircraft*, Vol. 34, No. 1, 1996, pp. 43-49.

[50] Frink, N. T., Pirzadeh, S. Z., Parikh, P. C., Pandya, M. M. J., and Bhat, M. K., "The NASA Tetrahedral Unstructured Software System (TetrUSS)," ICAS 2000 Congress, Paper 0241, 2000.

[51] Baldwin, B. S., and Lomax, H., "Thin Layer Approximation and Algebraic Model for Separated

Turbulent Flows," AIAA Paper 78-257, 1978.

[52] Degani, D., and Schiff, L. B., "Computation of Supersonic Viscous Flows Around Pointed Bodies at Large Incidence," AIAA Paper 83-0034, 1983.

[53] Vatsa, V. N., Thomas, J. L., and Wedan, B. W., "Navier-Stokes Computations of a Prolate Spheroid at Angle of Attack," *AIAA Journal of Aircraft*, Vol. 26, No. 11, 1989, pp. 986-993. Also AIAA Paper 87-2627, 1987.

[54] Meier, H. U., and Cebeci, T., "Flow Characteristics of a Body of Revolution at Incidence," *Third Symposium on Numerical and Physical Aspects of Aerodynamic Flows*, Long Beach, CA, 1985.

[55] Ghaffari, F. G., Luckring, J. M., Thomas, J. L., and Bates, B. L., "Navier-Stokes Solutions About the F/A-18 Forebody-Leading-Edge Extension Configuration," *AIAA Journal of Aircraft*, Vol. 27 No. 9, 1990. Also AIAA Paper 89-0338, 1989.

[56] Hall, R. M., Murri, D. G., Erickson, G. E., Fisher, D. F., Banks, D. W., and Lanser, W. R., "Overview of HATP Experimental Aerodynamics Data for the Baseline F/A-18 Configuration. NASA TM-112360, 1996.

[57] Rizk, Y. M., and Gee, K., "Unsteady Simulation of Viscous Flowfield Around F-18 Aircraft at Large Incidence," *AIAA Journal of Aircraft*, Vol. 29, No. 6, 1992, pp. 986-992. Also AIAA Paper 91-0020, 1991.

[58] Flores, J., and Chaderjian, N., "The numerical simulation of transonic separated flow about the complete F-16A," AIAA Paper 88-2506, 1988.

[59] Boelens, O. J., "CFD Analysis of the Flow Around the X-31 Aircraft at High Angle of Attack," AIAA Paper No. 2009-3628, 2009.

[60] RTO, "Assessment of Stability and Control Prediction Methods for NATO Air and Sea Vehicles," RTO-TR-AVT-161, 2012.

[61] Spalart, P. R., Jou, W-H., Strelets, M., and Allmaras, S. R., "Comments on the Feasibility of LES for Wings, and on a Hybrid RANS/LES Approach," Advances in DNS/LES, 1st AFOSR Int. Conf. on DNS/LES, 1997, Grey den Press, Columbus OH.

[62] Strang, W. Z., Tomaro, R. F., Grismer, M. J., "The Defining Methods of Cobalt: A Parallel, Implicit, Unstructured Euler/Navier-Stokes Flow Solver," AIAA Paper 1999-0786, 1999.

[63] Morton, S. A., Forsythe, J. R., Mitchell, J. M., and Hajek, D., "DES and RANS Simulations of Delta Wing Vortical Flows," AIAA Paper 2002-0287, 2002.

[64] RTO, "Vortex Breakdown over Slender Delta Wings," RTO-TR-AVT-080, 2009.

[65] Morton, S. A., Steenman, M., Cummings, R., and Forsythe, J. R., "DES Grid Resolution Issues for Vortical Flows on a Delta Wing and an F-18C," AIAA Paper 2003-1103, 2003.

[66] Forsythe, J. R., Squires, K. D., Wurtzler, K. E., and Spalart, P. R., "Detached-Eddy Simulation of the F-15E at High Alpha," *AIAA Journal of Aircraft*, Vol 41 No 2, 2004. Also AIAA 2002-0591, 2002.

[67] RTO, "Understanding and Modeling Vortical Flows to Improve the Technology Readiness Level for

Military Aircraft," RTO-TR-AVT-113, 2009.

[68] Luckring J. M., "Reynolds Number and Leading-Edge Bluntness Effects on a 65° Delta-Wing," AIAA Paper 2002-0419, 2002.

[69] Hummel, D., *Private discussion*, 2002

[70] Konrath, R., Klein, C., and Schröder, A., "PSP and PIV investigations on the VFE-2 configuration in sub- and transonic flow," *Aerospace Science and Technology*, Vol. 24, No. 1, 2013. Also AIAA Paper 2008-0379, 2008.

[71] Fritz, W., "Numerical simulation of the peculiar subsonic flow-field about the VFE-2 delta wing with rounded leading edge," *Aerospace Science and Technology*, Vol. 24, No. 1, 2013. Also AIAA Paper 2008-0393, 2008.

[72] Luckring, J. M., and Hummel, D., "What was learned from the new VFE-2 experiments," *Aerospace Science and Technology*, Vol. 24, No. 1, 2013. Also AIAA Paper 2008-0383, 2008.

[73] STO, "Reliable Prediction of Separated Flow Onset and Progression for Air and Sea Vehicles," STO-TR-AVT-183, 2017.

[74] Frink, N. T., Tomac, M., and Rizzi, A., "Collaborative study of incipient separation on 53º-swept diamond wing," *Aerospace Science and Technology*, Vol. 57, 2016. Also AIAA Paper 2015-0288, 2015.

[75] Hitzel, S. M., Boelens, O. J., Rooij, M., and Hövelmann, A., "Vortex development on the AVT-183 diamond wing configuration – numerical and experimental findings," *Aerospace Science and Technology*, Vol. 57, 2016. Also AIAA Paper 2015-0289, 2015.

[76] Daniel, D., Malloy, D. J., Reasor, D. A., Jr., and Morris, C. C., "Numerical Investigations of Flow Separation on the AVT-183 53 Degree Swept Diamond Wing Configuration," STO-TR-AVT-183, Chapter 15, 2017. Also AIAA Paper 2015-0066, 2015.

[77] Lamar, J. E., Obara, C. J., Fisher, B. D., and Fisher, D. F., "Flight, Wind-Tunnel, and Computational Fluid Dynamics Comparison for Cranked Arrow Wing (F-16XL-1) at Subsonic and Transonic Speeds," NASA TP 2001-210629, Feb 2001.

[78] Rizzi, A., Badcock, K. J., Jirásek, A., and Boelens, O. J., "What was Learned from Numerical Simulations of F-16XL (CAWAPI) at Flight Conditions," AIAA Paper 2007-0683, 2007.

[79] Elmiligui, A., Abdol-Hamid, K., Cavallo, P. A., and Parlette, E. B., "Vortex Numerical Simulations for the F-16XL Aircraft Configuration," AIAA Paper 2014-0756, Jan. 2014.

[80] Görtz, S. (2005), Realistic simulations of delta wing aerodynamics using novel CFD methods. KTH PhD Dissertation, Rep Trita-AVE 2005:01, Stockholm.

[81] Mitchell, A. M., "Caractérisation et contrôle de l'éclatement tourbillonnaire sur une aile delta aux hautes incidences," Ph.D. thesis, Université Paris VI, Paris, France, 2000.

[82] Luckring, J.M., Rizzi, A. and Davis, M.B.,: Toward Improved CFD Predictions of Slender Airframe Aerodynamics Using the F-16XL Aircraft (CAWAPI-2), AIAA Paper 2014-0419, 2014.

[83] Rizzi, A. and Luckring, J.M.: What was Learned in Predicting Slender Airframe Aerodynamics with the F16-XL Aircraft, AIAA Paper 2014-0759, 2014.

[84] Schiavetta, L. A., Boelens, O. J., Crippa, S., Cummings, R. M., Fritz, W., and Badcock, K. J., "Shock Effects on Delta Wing Vortex Breakdown," *AIAA Journal of Aircraft*, Vol. 46, No. 3, 2009, pp. 903-914. Also AIAA Paper 2008-0395, 2008.

[85] Crippa, S., "Advances in vortical flow prediction methods for design of delta-winged aircraft," KTH PhD Dissertation, Rep Trita-AVE 2008:30, Stockholm, 2008.

[86] Hall, R. M., Woodson, S. H., and Chambers, J. R., "Overview of the Abrupt-Wing-Stall Program," *Progress in Aerospace Sciences*, Vol. 40, 2004, pp. 417-452.

[87] Forsythe, J. R., and Woodson, S. H., "Unsteady Computations of Abrupt Wing Stall Using Detached-Eddy Simulation, *AIAA Journal of Aircraft*, Vol. 42, No. 3, 2005, pp. 606-616. Also AIAA Paper 2003-594, 2003.

[88] Le Moigne, Y., "Adaptive Mesh Refinement and Simulations of Unsteady Delta-Wing Aerodynamics," KTH PhD Dissertation, Rep Trita-AVE 2004:17, Stockholm, 2004.

[89] Frink, N. T., "Guidelines for Dynamic CFD Simulations on SACCON UCAV Configuration," STO-TR-AVT-161, Chapter 9, 2012.

[90] Frink, N. T., Tormalm, M., and Schmidt, S. et al., "Three Unstructured Computational Fluid Dynamics Studies on Generic Uninhabited Combat Air Vehicle," *AIAA Journal of Aircraft*, Vol. 49, No. 6, 2012, pp. 1619-1637.

[91] Mendenhall, M. R., Perkins Jr., S. C., Tomac, M., Rizzi, A. and Nangia, R. K., "Comparing and benchmarking engineering methods for the prediction of X-31 aerodynamics," *Aerospace Science and Technology*, Vol. 20, 2012, pp.12-20.

[92] Rumsey, C. L., Slotnick, J. P., Long, M., Stuever, R. A., and Wayman, T. R., "Summary of the First AIAA CFD High-Lift Prediction Workshop," *AIAA Journal of Aircraft*, Vol. 48, No. 6, 2011, pp. 2068–2079

[93] Eliasson, P., Hanifi, A., and Peng, S-H., "Influence of Transition on High-Lift Prediction for the NASA Trap Wing Model," AIAA Paper 2011-3009, 2011.

[94] Tomac, M. (2014). Towards automated CFD for engineering methods in aircraft design (TRITA-AVE, 2014:11). Stockholm: Engineering Sciences, KTH Royal Institute of Technology.

[95] Langtry, R. B., and Menter, F. R., "Correlation-Based Transition Modeling for Unstructured Parallelized Computational Fluid Dynamics Codes," *AIAA Journal*, Vol. 47, No. 12, 2009, pp. 2894-2906.

[96] Tomac, M., Rizzi, A., Charbonnier, D, Vos, J. B., Jirásek, A., Peng, S-H., Winkler, A., Allen, A., Wissocq, G., Puigt, G., Dandois, J., and Abarca-Lopez, R., "Unsteady Aero-Loads from Vortices Shed on A320 Landing Gear Door: CFD Compared to Flight Tests," AIAA Paper 2016-0803, 2016.

[97] Plentovich, E. B., Stallings, R. L., Jr., and Tracy, M. B., "Experimental Cavity Pressure Measurements at Subsonic and Transonic Speeds. Static Pressure Results," NASA TP 3358, 1993.

[98] Tracy, M. B., and Plentovich, E. B., "Cavity Unsteady-Pressure Measurements at Subsonic and

Transonic Speeds," NASA TP 3669, 1997.

[99] Stallings, R. L., Jr., and Forrest, D. K., "Separation Characteristics of Internally Carried Stores at Supersonic Speeds," NASA TP-2993, 1990.

[100] Stallings, R. L., Jr., and Wilcox, F. J., Jr., "Measurements of Forces, Moments, and Pressures on a Generic Store Separating From a Box Cavity at Supersonic Speeds," NASA TP-3110, 1991.

[101] Stallings, R. L., Jr., Plentovich, E. B., Tracy, M. B., and Hemsch, M. J., "Measurements of Store Forces and Moments and Cavity Pressures for a Generic Store in and Near a Box Cavity at Subsonic and Transonic Speeds," NASA TM-4611, 1995.

[102] Luckring, J.M., "The Discovery and Prediction of Vortex Flow Aerodynamics," *The Aeronautical Journal*, Vol. 123, No. 1264, 2019, pp. 729-804.

[103] Spalart, P. R, and Venkatakrishnan, V., "On the Role and Challenges of CFD in the Aerospace Industry," *The Aeronautical Journal*, Vol. 120, No. 1223, 2016, pp. 209-232.

[104] Bush, R. H., Chyczewski, T. S., Duraisamy, H., Eisfeld, B., Rumsey, C. L., and Smith, B. R., "Recommendations for Future Efforts in RANS Modeling and Simulation," AIAA Paper 2019-0317, 2019.

[105] Krist, S. E., Ratnayake, N. A., and Ghaffari, F., "Kestrel Results at Liftoff Conditions for a Space Launch Configuration in Proximity to the Launch Tower," AIAA Paper 2019-3400, 2019.

[106] Krist, S. E., *Private communication*, 2018.